UDK 66:54(05) CODEN HMIDA 8 ISSN 0367–598X

1

Vol. 79

# Hemijska industrija

Časopis Saveza hemijskih inženjera Srbije

# Chemical Industry

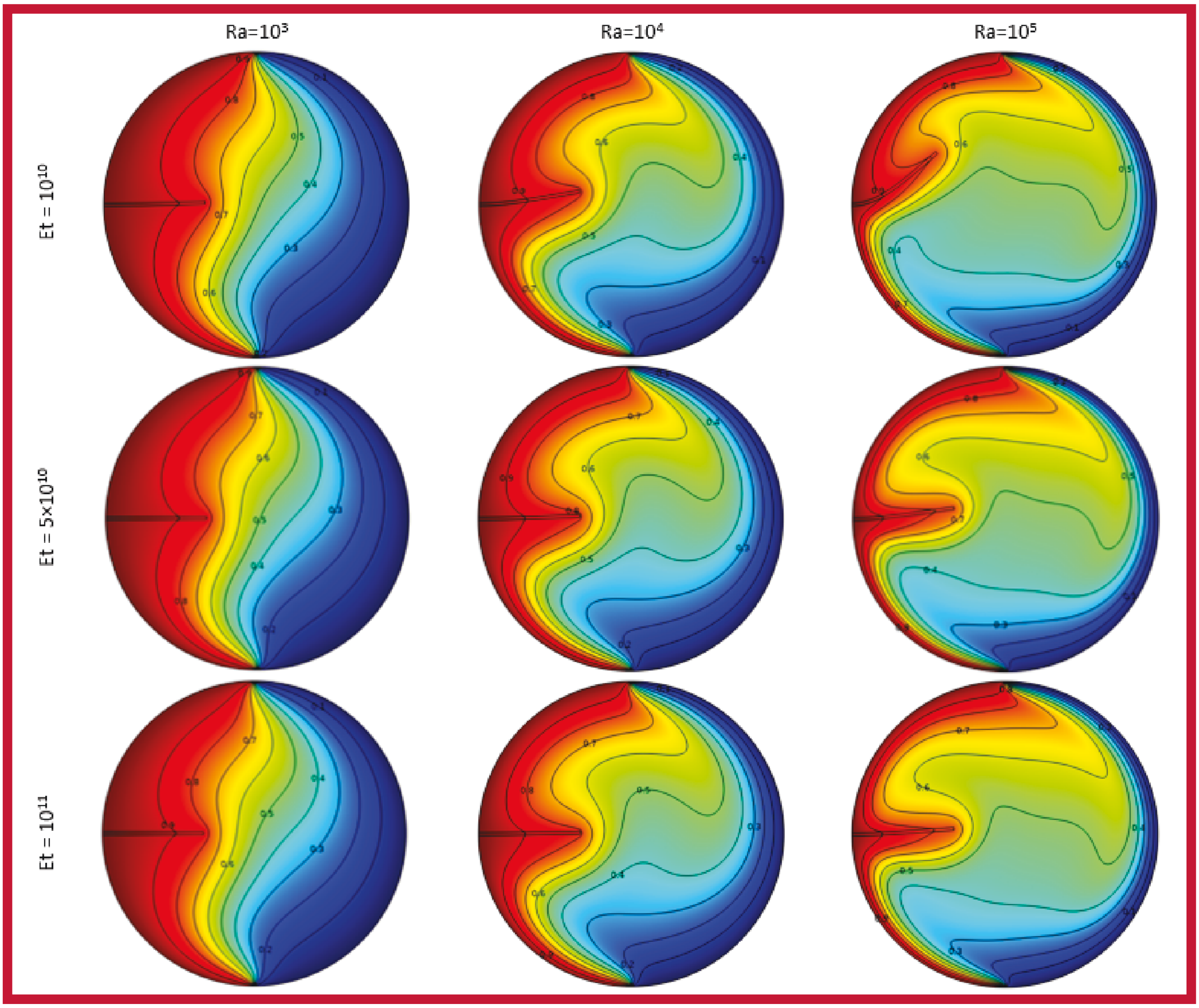

BEOGRAD, JANUAR - MART 2025. HMIDA 8, 79(1) 1-77 (2025)

## Aktivnosti Saveza hemijskih inženjera Srbije pomažu:

**MINISTARSTVO NAUKE,
TEHNOLOŠKOG RAZVOJA
I INOVACIJA
REPUBLIKE SRBIJE**

Tehnološko-metalurški fakultet
Univerziteta u Beogradu

Prirodno-matematički fakultet
Univerziteta u Novom Sadu

ITNMS
Institut za tehnologiju nuklearnih i
drugih mineralnih sirovina, Beograd

Tehnološki fakultet
Univerziteta u Novom Sadu

Institut za hemiju, tehnologiju i metalurgiju
Univerziteta u Beogradu

Fakultet tehničkih nauka
Univerziteta u Novom Sadu

Tehnološki fakultet
Univerziteta u Nišu, Leskovac

Fakultet tehničkih nauka
Univerziteta u Prištini
Kosovska Mitrovica

Institut IMS, Beograd

DCP HEMIGAL
Leskovac

Barič

Elixir Prahovo

Srbija
Beograd
SHI

Chemical Industry
Химическая промышленность

# Hemijska industrija

Časopis Saveza hemijskih inženjera Srbije
Journal of the Association of Chemical Engineers of Serbia
Журнал Союза химических инженеров Сербии

**VOL. 79** **Beograd, januar – mart 2025.** **Broj 1**

*Izdavač*
Savez hemijskih inženjera Srbije
Beograd, Kneza Miloša 9/I

*Redakcija*
11000 Beograd, Kneza Miloša 9/I
Tel/fax: 011/3240-018
E-pošta: shi@ache.org.rs
www.ache.org.rs

Izlazi kvartalno, rukopisi se ne vraćaju

*Za izdavača:* Ivana T. Drvenica

*Sekretar redakcije:* Slavica Desnica

*Izdavanje časopisa pomaže*
Republika Srbija, Ministarstvo nauke, tehnološkog razvoja i inovacija

Uplata pretplate i oglasnog prostora vrši se na tekući račun Saveza hemijskih inženjera Srbije, Beograd, broj 205-2172-71, Komercijalna banka a.d., Beograd

*Menadžer časopisa i kompjuterska priprema*
Aleksandar Dekanski

*Štampa*
Razvojno-istraživački centar grafičkog inženjerstva, Tehnološko-metalurški fakultet, Univerzitet u Beogradu, Karnegijeva 4, 11000 Beograd

*Indeksiranje*
Radovi koji se publikuju u časopisu *Hemijska Industrija* ideksiraju se preko *Thompson Reuters Scietific®* servisa *Science Citation Index - Expanded™* i *Journal Citation Report (JCR)*

## SADRŽAJ/CONTENTS

### Waste Water Treatment/Tretman tečnog otpada

Jovana Gradinac, Aleksandar Jovović, **Electrocoagulation as a new and advanced technology for future challenges in the steel industry's water treatment plants/ Tehnologija elektrokoagulacije kao nova i napredna tehnologija za buduće izazove u postrojenjima za prečišćavanje vode u industriji čelika** ..................... 1

Zorana Z. Radibratović, Biljana B. Cakić, Marija N. Vilotijević, Ivona R. Radović, Mirjana Lj. Kijevčanin, **Implementation of emergency measures to improve the efficiency of nickel removal from water at the existing water treatment plant / Sprovođenje hitnih mera za poboljšanje efikasnosti uklanjanja nikla iz vode na postojećem postrojenju za prečišćavanje vode** ........... 9

### Metal Materials/Metalni materijali

Jelena N. Stefanović, Zoran Mišković, Stevan Dimitrijević, Zlatko Marković, Milan Spremić, **Experimental analysis of atmospheric corrosion of steel S235JR in industrial environment / Eksperimentalna analiza atmosferske korozije čelika S235JR u industrijskoj sredini** ..................... 19

### Simulations and Optimozation/Simulacija i optimizacija

Atika Bencherif, Mohamed Bouzit, Abderrahim Mokhefi, Hanaa Derraz, Fatima Zohra Khelif, **Numerical investigation of free convection within a circular cavity with a flexible fin / Analiza termičkog ponašanja reaktora sa nepokretnim slojem u procesu pirolize** ..................... 31

### Let's refresh our knowledge/Osvežimo naše znanje

Anita M. Lazić, Luka R. Matović, Nemanja P. Trišović, Nataša V. Valentić, **Harnessing the potential of selected plant pigments in dye-sensitized solar cells: the current status / Potencijal odabranih biljnih pigmenata za korišćenje u solarnim ćelijama aktiviranim bojom: trenutni status** ..................... 47

**Erratum** ..................... 67

# Electrocoagulation as a new and advanced technology for future challenges in the steel industry's water treatment plants

**Jovana Gradinac and Aleksandar Jovović**

*University of Belgrade, Faculty of Mechanical Engineering, Belgrade, Serbia*

TECHNICAL PAPER

**UDC: 66.087.5: 669.18.013+632.153**

*Hem. Ind.* **79(1)** 1-8 (2025)

*Abstract*

Water is a basic necessity of life, and it may seem inconceivable to imagine living without it. The environmental impact, together with social and economic impacts of traditional water treatment technologies in the steel industry plants and inevitable fact of water scarcity are leading forces driving a shift to a new paradigm in water treatments.

This research aimed to examine the effectiveness of an electrocoagulation (EC) process and a dissolved air flotation unit for removing various impurities in water from a steel manufacturing plant. Over the past decades EC has been accepted as an efficient and promising alternative technology in the field of water treatment. The EC technique is closely related to chemical coagulation, that involves the supply of coagulant ions by the application of electric current to a sacrificial anode (made of aluminum or iron) placed into a process tank. The main focus of the research is placed on total dissolved solids and conductivity of the treated water. In traditional systems, these are among the parameters that cannot be influenced by chemical dosing units. The specific goal was to understand parameters affecting efficiency of the EC process so to influence the total dissolved solids content and reduction of the residual inorganic and organic impurities, maintaining the necessary water balance.

*Keywords:* water savings, innovative solutions, green industry, recycling, electrochemical process

*Available on-line at the Journal web address:* http://www.ache.org.rs/HI/

## 1. INTRODUCTION

Industrial growth and the changes in manufacturing processes have resulted in the enhancement of the volume and complexity of water discharging to the environment. Many traditional and/or advanced and novel treatment processes have been modified and developed to eliminate or improve the quality of discharged water. Industrial effluents may also contain toxic pollutants, which have to be reduced or eliminated to protect the treatment plant in which they are treated, as well as the environment and public health at the end [1].

Steel industry is one of the main production technologies, which generates large amounts of wastewater. The key problems encountered for industrial wastewater discharges may be hydraulic overloads, temperature extremes and excessive amounts of oil, fats and grease as well as acidic or alkaline constituents, suspended solids, and various inorganic or organic contents [2-6]. Discharge of the steel industry wastewater into sewer systems without any treatment causes serious problems due to high potentials of toxicity causing a necessity for biological treatment [7].

The generated wastewater can be treated by different techniques which should allow either its reuse or its direct disposal into the sewage system. Some of these techniques are reverse osmosis carried out in plants with high energy consumption, or physical-chemical treatments that sometimes cannot achieve the satisfactory level of purification. [8]

Nowadays, the social concern about environmental impacts caused by industry is growing and new regulations demanding more strict environmental protection are being introduced. For this reason, the search for ''greener'' and more efficient methods for wastewater treatment is increasing [9].

Over the past decades, electrocoagulation (EC), sometimes also referred to as electroflocculation, has been accepted as an efficient and promising alternative technology in the field of water treatment. Interestingly, EC offers outstanding

---

Corresponding authors: Jovana Gradinac, University of Belgrade, Faculty of Mechanical Engineering, Belgrade, Serbia
Paper received: 22 April 2024; Paper accepted: 13 January 2025; Paper published: 15 April 2025.
E-mail: jgradinac23@gmail.com
https://doi.org/10.2298/HEMIND240422026G

advantages including simple operation, lower sludge production, and simple automation. When EC operates at low current density, the operating cost of this process is often lower than that of the chemical coagulation process. In particular, EC offers more attractive properties for use in decentralized water treatments [10].

The EC methods use electrons as the main reagent in a heterogeneous reaction. When ionic constituents in wastewater are not sufficient, the use of supporting electrolyte is required to increase the ionic conductivity. The advantages of electrocoagulation include high particulate removal efficiency, a compact treatment facility, relatively low cost, does not require supplementary addition of chemicals, *etc.* [11].

The main advantage of this process is that the temperature control is not needed since EC is performed at ambient temperature. Electrochemical methods are simple, fast, inexpensive, easily operable and eco-friendly in nature. The main advantage is that water is purified, clear, colourless and odourless with low sludge production [12].

The EC technique is closely related to chemical coagulation, that involves the supply of coagulant ions ($Al^{3+}$, $Fe^{3+}$) by the application of an electric current to a sacrificial anode (made of aluminum or iron) placed into a process tank. The electric field allows greater suspension of solids compared to water purification processes that rely solely on chemicals. Thus, the electrocoagulation equipment, thanks to the created electric field and greater suspension of solids, is improving the coagulation process.

It proceeds through three stages: (i) coagulant formation by dissolution of metal ions of the anode, (ii) destabilization of pollutants, suspended particles and de-emulsification, and (iii) aggregation of unstable phases and floc-formation [12-15]. Destabilization of pollutants suspended particles, and de-emulsification mechanisms can be established through dispersed double-layer compression, ion neutralization species existing in water and wastewaters, leading to formation of flocs and sludge [15-16]. In this study, iron electrodes have been used in an EC process.

The mechanism of EC is extremely dependent on chemistry of the aqueous medium, especially its conductivity and total dissolved solids. Here the mechanism of generating ions by EC is explained with examples of iron, used as both the anode and cathode in this study. In an electrolytic system, iron is oxidized to produce iron hydroxide $Fe(OH)_n$ where $n = 2$ or 3. According to literature [17], two mechanisms have been proposed for the production of these species and we describe here one of the two (Equations (1) to (4)), while more details can be found in [17].

Reactions at the anode:

$$4Fe_{(s)} \rightarrow Fe_{aq}^{2+} + 8e^- \tag{1}$$

$$4Fe^{2+}_{(aq)} + 10H_2O + O_{2(g)} \rightarrow 4Fe(OH)_{3(s)} + 8H^+_{(aq)} \tag{2}$$

Reactions at the cathode:

$$8H^+_{(aq)} + 8e^- \rightarrow 4H_{2(g)} \tag{3}$$

Overall reaction is then:

$$4Fe_{(s)} + 10H_2O + O_{2(g)} \rightarrow Fe(OH)_{3(s)} + 4H_{2(g)} \tag{4}$$

From iron electrodes, iron ions are released into the solution through electrolytic oxidation of anode electrode and produce metal hydroxides after reacting with hydroxide monomer [11,18].

Hydrogen gas produced at the cathode during electrolysis cause flotation and better removal of pollutants [11,19].

In the steel industry, water is cooled in cooling towers and due to evaporation, salts and solids are created. The water composition determines the number of water cycles within the system (*NC*), before it is discharged, as per the Equation (5):

$$NC = \frac{TDS_{\mathrm{BD}}}{TDS_{\mathrm{MW}}} \tag{5}$$

where $TDS_{\mathrm{BD}}$ and $TDS_{\mathrm{MW}}$ represent total dissolved solids present in blow down (discharged) water and make up (raw, treated) water

In traditional systems, total dissolved solids and conductivity of the water, are one of the parameters that cannot be influenced by chemical dosing units.

The aim of this study was to investigate a pilot half-industrial system comprising an electrocoagulation process using rod-iron electrodes and a dissolved air flotation (DAF) unit. The specific goal was to understand parameters affecting efficiency of the EC process so to influence the total dissolved solids content and reduction of the residual inorganic and organic impurities. Such water quality improvement, any blow down from the system would be prevented leading to significant water savings.

## 2. RESEARCH METHODOLOGY

### 2. 1. Experimental setup

The studies were performed on a pilot plant that was in trial use in a steel manufacturing plant placed in North Italy and was composed of two main equipment pieces: an electrocoagulation unit and a dissolved air flotation (DAF) unit.

Inlet water was pumped from a scale pit at a flow rate of 10 $m^3 h^{-1}$ to a buffer tank, 1 $m^3$ in volume. From the buffer tank, a dedicated pump, placed inside the pilot system, pumped water at a flow rate of 1 $m^3 h^{-1}$ to the EC equipment, where minerals were removed. From this point, water was collected in a dedicated another buffer tank, from where water was pumped to the DAF unit. The finally treated water was returned into scale pit (Figure 1).

The EC equipment consists of oxidation cells, constructed of polypropylene, agitated by compressed air and supplied with an electric current rectifier with variable voltage/amperage for power supply. The configuration allows adjusting the number of electrodes and the distance between them, providing a tuning in the energy/electric ratio. There were 114 iron electrodes, each a rectangle 16×13 cm, spaced 0.5 cm apart.

The DAF unit is designed to treat the water coming from the EC equipment so to separate water from the sludge.

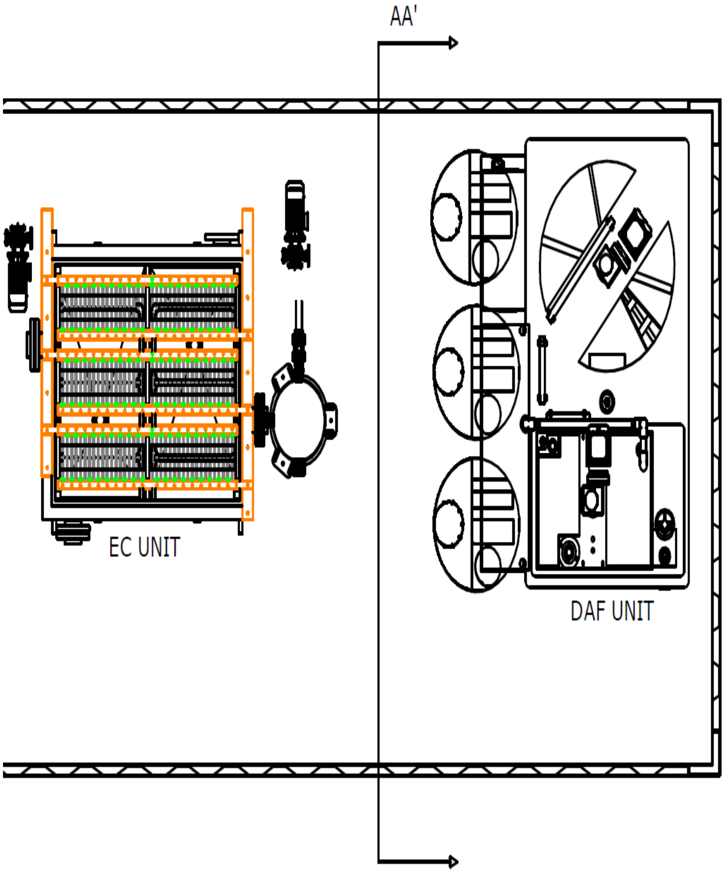

Figure 1. Schematic configuration of the pilot plant

### 2. 2. Analytical methods

Water was analyzed by standard methods as presented in Table 1.

Efficiency of the EC treatment was evaluated by analysing the removal of all parameters measured in Table 1, but the most important for the study was total dissolved solids (TDS).

*Table 1. Analysed parameters in water and applied methods*

| Parameter | Method |
|---|---|
| Content of total dissolved solids, mg dm$^{-3}$ | APAT CNR IRSA 2090 A Man 29 2003 |
| Hardness, mg dm$^{-3}$ | APAT CNR IRSA 2010 Man 29 2003 |
| Total alkalinity, mg dm$^{-3}$ | APAT CNR IRSA 2010 Man 29 2003 |
| Content of chlorides, mg dm$^{-3}$ | APAT CNR IRSA 4020 Man 29 2003 |
| Content of fluorides, mg dm$^{-3}$ | APAT CNR IRSA 4020 Man 29 2003 |
| Content of sulfates, mg dm$^{-3}$ | APAT CNR IRSA 4020 Man 29 2003 |
| Total iron content, mg dm$^{-3}$ | EPA 6020B 2014 |
| Dissolved iron content, mg dm$^{-3}$ | EPA 6020B 2014 |
| Copper content, mg dm$^{-3}$ | EPA 6020B 2014 |
| Ammonia nitrogen content (as $NH_4$), mg dm$^{-3}$ | UNI 11669:2017 |
| Content of total suspended solids, mg dm$^{-3}$ | APAT CNR IRSA 2090 B Man 29 2003 |
| Oil and grease content, mg dm$^{-3}$ | MI 30 REV.3 2018 (APAT 5160 A) |
| Silicium content, mg dm$^{-3}$ | UNI EN ISO 11885:2009 |
| Chemical oxygen demand, mg dm$^{-3}$ | ISO 15705:2002 |

In research [20], the filtered cooling tower water was analyzed to determine the scale ions concentration. The analysis was performed using the APHA (2012) standard methods. Concentrations of the cations and anions were determined by using a UNICO SQ2800 UV/VIS spectrophotometer (Unico, NJ, USA) and a Dionex ICS-1000 ion chromatography system (Thermo Fisher Scientific, USA). Water pH was measured using a Fisherbrand™ FE150 pH meter (Fisher Scientific, Leicestershire, UK) and the conductivity was measured by a Laqua DS70 conductivity meter (Horiba Advanced Techno, Japan).

Via dosing pumps, anionic polymer flocculant solution VAFLOC 974 (Hangrui, China), was added continuously at a flowrate of 1 m$^3$ h$^{-1}$ to the DAF unit for better segregation and separation of the particles.

## 3. RESULTS

Water quality analysis was conducted in a commercial pilot system in a steel manufacturing plant at three selected points:

- inlet point presenting raw water quality,
- intermediate point presenting water quality after the EC process,
- outlet point presenting water quality after the DAF unit.

Results of the measurements at the selected points are shown in Tables 2 to Table 4.

*Table 2. Raw water quality at the inlet point over time*

| | Measurement date | | | | | |
|---|---|---|---|---|---|---|
| Parameters | 21/03/23 | 22/03/23 | 23/03/23 | 27/03/23 | 28/03/23 | 29/03/23 |
| Content of total dissolved solids, mg dm$^{-3}$ | 304 | 300 | 305 | 308 | 304 | 303 |
| Hardness, mg dm$^{-3}$ | 150 | 162 | 170 | 154 | 160 | 150 |
| Total alkalinity, mg dm$^{-3}$ | 80 | 90 | 87 | 100 | 90 | 70 |
| Content of chlorides, mg dm$^{-3}$ | 42 | 43 | 45 | 46 | 48 | 46 |
| Content of fluorides, mg dm$^{-3}$ | 0.17 | 0.16 | 0.16 | 0.16 | 0.17 | 0.15 |
| Content of sulfates, mg dm$^{-3}$ | 88 | 89 | 90 | 94 | 92 | 89 |
| Total iron content, mg dm$^{-3}$ | 7.2 | 14 | 9 | 5.1 | 13 | 9 |
| Dissolved iron content, mg dm$^{-3}$ | 0.0084 | 0.0062 | 0.007 | 0.0052 | 0.007 | 0.0064 |
| Copper content, mg dm$^{-3}$ | 0.2 | 0.29 | 0.3 | 0.14 | 0.3 | 0.24 |
| Ammonia nitrogen content (as $NH_4$), mg dm$^{-3}$ | 0.034 | 0.02 | 0.02 | 0.02 | 0.02 | 0.02 |
| Content of total suspended solids, mg dm$^{-3}$ | 72 | 112 | 105 | 70 | 115 | 102 |
| Oil and grease content, mg dm$^{-3}$ | 2 | 2 | 2 | 12 | 2 | 6 |
| Silicium content, mg dm$^{-3}$ | 2.255 | 2.108 | 2.3 | 1.76 | 2.1 | 1.9 |
| Chemical oxygen demand, mg dm$^{-3}$ | 9 | 10 | 10 | 10 | 7 | 5 |

Performance of the studied pilot half-industrial system was monitored for 9 days, where the major focus was on understanding the influence on the total dissolved solids (TDS) removal, as that parameter can not be influenced with chemical dosing units.

When the system was put in the working mode, in the first week, parameters were changed day by day to understand the influence of each parameter on the TDS removal. On day 1 the EC system was set at 45 A and 5.1 m$^2$ kg s$^{-3}$ A$^{-1}$, followed by 126 A and 8 m$^2$ kg s$^{-3}$ A$^{-1}$ on day 2, 85 A and 5.9 m$^2$ kg s$^{-3}$ A$^{-1}$ on day 3, while from day 4 to day 6 the system was set at 93 A and 6.3 m$^2$ kg s$^{-3}$ A$^{-1}$.

*Table 3. Water quality after the EC process at the intermediate point*

| | Measurement date | | | |
|---|---|---|---|---|
| Parameter | 21/03/23 | 23/03/23 | 28/03/23 | 29/03/23 |
| Content of total dissolved solids, mg dm$^{-3}$ | 246 | 212 | 296 | 268 |
| Hardness, mg dm$^{-3}$ | 277.4 | 152 | 147 | 147 |
| Total alkalinity, mg dm$^{-3}$ | 50 | 80 | 75 | 75 |
| Content of chlorides, mg dm$^{-3}$ | 45 | 45 | 49 | 46 |
| Content of fluorides, mg dm$^{-3}$ | 0.16 | 0.16 | 0.17 | 0.16 |
| Content of sulfates, mg dm$^{-3}$ | 92 | 91 | 96 | 93 |
| Total iron content, mg dm$^{-3}$ | 110 | 40 | 49 | 36 |
| Dissolved iron content, mg dm$^{-3}$ | 1.5 | 0.036 | 5.1 | 0.012 |
| Copper content, mg dm$^{-3}$ | 0.36 | 0.14 | 0.23 | 0.098 |
| Ammonia nitrogen content (as $NH_4$), mg dm$^{-3}$ | 0.02 | 0.015 | 0.02 | 0.02 |
| Content of total suspended solids, mg dm$^{-3}$ | 240 | 111 | 177 | 94 |
| Oil and grease content, mg dm$^{-3}$ | 6 | 4 | 13 | 1,6 |
| Silicium content, mg dm$^{-3}$ | 2.66 | 1.86 | 1.06 | 0.85 |

Water was analysed after the EC process to evaluate performance of this process as well.

Over the time, the effect of current density on various parameters is described above in text. With the increase in the current from 45 to 126 A the removal efficiency of total iron, hardness and total suspended solids (TSS) also increases. This is due to the higher number of ions produced on the electrodes promoting destabilization of the pollutant molecules. The removal percentage of major parameters (beside iron and hardness) maintains a plateau from current 85 to 126 A.

However, compared to the raw water, the total iron content after the EC process was increased due to the use of sacrificial electrodes made of iron.

Still, the most important parameter followed in this study, TDS, has shown a satisfactory removal trend, even after using the EC process, only (an average removal of about 16 % with a standard deviation of ~12 %).

*Table 4. Water quality parameters after the DAF unit at the outlet point;*

| | Measurement date | | | | | |
|---|---|---|---|---|---|---|
| Parameters | 21/03/23 | 22/03/23 | 23/03/23 | 27/03/23 | 28/03/23 | 29/03/23 |
| Content of total dissolved solids, mg dm$^{-3}$ | 240 | 192 | 228 | 284 | 296 | 282 |
| Hardness, mg dm$^{-3}$ | 160 | 146 | 16 | 151 | 156 | 153 |
| Total alkalinity, mg dm$^{-3}$ | 80 | 80 | 1.8 | 75 | 100 | 75 |
| Content of chlorides, mg dm$^{-3}$ | 42 | 43 | 43 | 46 | 46 | 45 |
| Content of fluorides, mg dm$^{-3}$ | 0.15 | 0.16 | 0.16 | 0.17 | 0.17 | 0.17 |
| Content of sulfates, mg dm$^{-3}$ | 88 | 89 | 90 | 93 | 95 | 95 |
| Total iron content, mg dm$^{-3}$ | 4.4 | 16 | 26 | 6.7 | 1.5 | 5.8 |
| Dissolved iron content, mg dm$^{-3}$ | 0.00019 | 0.033 | 0.0046 | 0.00576 | 0.0015 | 0.0016 |
| Copper content, mg dm$^{-3}$ | 0.034 | 0.061 | 0.082 | 0.07 | 0.061 | 0.047 |
| Ammonia nitrogen content (as $NH_4$), mg dm$^{-3}$ | 0.018 | 0.018 | 0.17 | 0.37 | 0.42 | 0.64 |
| Content of total suspended solids, mg dm$^{-3}$ | 10 | 42 | 6 | 19 | 4 | 13 |
| Oil and grease content, mg dm$^{-3}$ | 1.8 | 6 | 2 | 1.8 | 1.8 | 6 |
| Silicium content, mg dm$^{-3}$ | 1.683 | 2.627 | 2.66 | 0.86 | 1.5 | 1.4 |
| Content of total dissolved solids, mg dm$^{-3}$ | 6 | 5 | 6 | 7 | 4 | 4 |

At the outlet point, there was some increase in the $NH_4$, and this could be related to the usage of polymer flocculants that could have some quantity of the polyamide (which contains nitrogen).

Other parameters like chlorides, fluorides and sulfates were not influenced by the DAF unit operating conditions.

The TDS observed removal of around 20 to 30 % in the first several days after the DAF unit, and something less in the later period, but still almost at 10 %. The removal efficiencies were higher for copper, oil and greases, and TSS ranging between 81 to 50 %. Silicium was also significantly removed, achieving in some cases 50 % removal efficiency.

## 4. DISCUSSION

When designing a water treatment plant including the operational parameters it is crucial to know the raw water quality. Also, in order to evaluate the plant performance, it is necessary to monitor the inlet water quality and thus the water parameters were monitored at the moment of starting the trial of the pilot system.

Some of the key parameters affecting the outlet water quality and desirable performance on an EC process include current density, electrode material and electrode arrangement, inter-electrode distance, initial water composition and retention time. A key parameter, though, is the current density, which is the current applied per the effective electrode surface area. The current density determines the release rate of electrons as a consequence of the dissociation of metal ions from the electrode [21,22]. However, the range of current density applied varies widely for different types of the process water and its quality. Differences arise mostly due to variations in ionic interaction. The current if not applied correctly, can influence the removal of contamination. An excess of the current density, for example, can negatively affect the removal as it can enable secondary reactions. Thus, it is very important to make a pre-evaluation of the inlet water, to set the correct operation parameters.

In the present case, it is evident how various values of the current, have affected removal of the impurities.

Removal of total dissolved solids was shown to be the best at 126 A amounting to around 30 %, while on average during the complete study, removal was 17±13 %.

Ammonia nitrogen removal efficiency depends on the electrolysis time and the current density value. At both low current and electrolysis time, the ammonia nitrogen removal efficiency was lower.

The electrochemical method was used to investigate nitrite and ammonia removal from an aqueous solution in literature [23]. The results showed that removal was improved when electrolysis time in the cell was extended. The pH effect on nitrite removal was less significant than conductivity and current input. The iron electrode was unsuitable for removing nitrite due to its low removal efficiency. However insoluble electrodes such as a graphite anode and titanium dioxide cathode were appropriate for removing nitrite and ammonia in electrochemical cells. It was thought that there are two possible mechanisms involved in the process, electro-flotation and electro-oxidation, while it was concluded that more investigations need to be done [26].

Hardness removal was not successful probably due to non-optimized conditions applied during the investigation. A study in literature [24] has shown that the maximal removal efficiency at pH 7.0 and application of aluminum electrodes was achieved at the voltage of 6 $m^2$ kg $s^{-3}$ $A^{-1}$ and a reaction time of 60 min, amounting to 95.4 and 95.7 % for calcium and total hardness, respectively.

## 5. CONCLUSION

The electrocoagulation process presents an environmentally friendly process that can be applied for removal of various impurities. This study was conducted with the goal to examine the EC pilot system focusing particularly on TDS removal along with other water quality parameters. The system gave a positive answer for the purpose of the water treatment plants in the steel industry. The goal of this research was to decrease the TDS value so to show that by maintaining water impurities under necessary limits within water treatment plants, discharge of the water can be avoided. Still, along with some positive results, some parameters like hardness, chlorides, ammonia nitrogen and sulfates were not significantly removed. Further examination should be conducted to include a combination with some other applications (for example electro Fenton process) or by changing the electrode material and configuration of the EC process.

***Acknowledgements:*** The authors thank the SMS Group SpA and Andrea Nadalutti for giving maximum support in this investigation and allowing its publication.

## REFERENCES

[1] Araújo CVM, Nascimento RB., Oliveira CA., Strotmann UJ, Da Silva EM. The use of Microtox® to assess toxicity removal of industrial effluents from the industrial district of Camaçari (BA, Brazil). *Chemosphere.* 2005; 58(9):1277-1281 https://doi.org/10.1016/j.chemosphere.2004.10.036

[2] Heidmann I., Calmano W. Removal of Zn(II), Cu(II), Ni(II), Ag(I) and Cr(VI)present in aqueous solutions by aluminium electrocoagulation. *J Hazard Mater.* 2008; 152: 934-941. https://doi.org/10.1016/j.jhazmat.2007.07.068

[3] Akbal F., Camci S. Copper, chromium and nickel removal from metal plating wastewater by electrocoagulation. *Desalination.* 2011; 269: 214-222. https://doi.org/10.1016/j.desal.2010.11.001

[4] Akbal F., Camci S. Treatment of metal plating wastewater by electrocoagulation. *Environ Prog Sustain Energy.* 2012; 31: 340-350 https://doi.org/10.1002/ep.10546

[5] Kabuk HA., Avsar Y., Ilhan F., Ulucan K. Comparison of pH adjustment and electrocoagulation processes on treatability of metal plating wastewater. *Sep Sci Technol.* 2014; 49: 613-618. https://doi.org/10.1080/01496395.2013.839705

[6] Al-Shannag M, Al-Qodah Z, Bani-Melhem K., Qtaishat MR, Alkasrawi M. Heavy metal ions removal from metal plating wastewater using electrocoagulation: kinetic study and process performance. *Chem Eng J.* 2015; 260: 749-756. https://doi.org/10.1016/j.cej.2014.09.035

[7] Hunsom M, Pruksathorn K, Damronglerd S, Vergnes H, Duverneuil P. Electrochemical treatment of heavy metals (Cu$^{2+}$, Cr$^{6+}$, Ni$^{2+}$) from industrialeffluent and modeling of copper reduction. *Water Res.* 2005; 39: 610-616. https://doi.org/10.1016/j.watres.2004.10.011

[8] David V, Ortiz JM, Vicente G, Eduardo E, Vicente M, Antonio A. Electrocoagulation of wastewater from almond industry. *Chemosphier.* 2011; 84: 1290-1295. https://doi.org/10.1016/j.chemosphere.2011.05.032

[9] Lancaster M. Green Chemistry, An Introductory Text. Royal Society of Chemistry, *Org Proc Res Dev.* 2004: 8, 2: 299-300. https://doi.org/10.1021/op049976c

[10] Jianbo L., Peng Z., Jie L. Electrocoagulation technology for water purification: An update review on reactor design and some newly concerned pollutants removal. *J Environ Manag.* 2021; 84. https://doi.org/10.1016/j.jenvman.2021.113259

[11] Bazrafshan E, Mohammadi L, Ansari-Moghaddam A, Mahvi AH. Heavy metals removal from aqueous environments by electro-coagulation process- a systematic review. *J Environ Health Sci.* 2015; 13: 74. https://doi.org/10.1186/s40201-015-0233-8

[12] Van der Bruggen B, Everaert K, Wilms D, Vandecasteele C. Application of nanofiltration for removal of pesticides, nitrate and hardness from ground water: rejection properties and economic evaluation. *J Membr Sci.* 2001; 193: 239-248. https://doi.org/10.1016/S0376-7388(01)00517-8

[13] Chou WL, Wang CT, Huang KY. Effect of operating parameters on indium (III) ion removal by iron electrocoagulation and evaluation of specific energy consumption. *J Hazard Mater.* 2009; 167(1-3):467-474. https://doi.org/10.1016/j.jhazmat.2009.01.008

[14] DrouicheN, Ghaffour N, Lounici H, Mameri M. Electrocoagulation of chemical mechanical polishing wastewater. *Desalination.* 2007; 214: 31-37. https://doi.org/10.1016/j.desal.2006.11.009

[15] Hyun Kim T, Park C, Shin E-B, Kim S. Decolorization of disperse and reactive dyes by continuous electrocoagulation process. *Desalination.* 2002; 150: 165-175, https://doi.org/10.1016/S0011-9164(02)00941-4

[16] Holt PK, Barton G, Wark M, Mitche C. A quantitative comparison between chemical dosing and electrocoagulation. *Colloid Surf A.* 2002; 211: 233-248. https://doi.org/10.1016/S0927-7757%2802%2900285-6

[17] Mollah MYA, Schennach R, Parga JR, Cocke DL. Electrocoagulation (EC) science and applications. *J Hazard Mater.* 2001; B84: 29-41. https://doi.org/10.1016/S0304-3894(01)00176-5

[18] Hu CY, Lo SL, Kuan WH. Effects of co-existing anions on fluoride removal in electrocoagulation (EC) process using aluminum electrodes. *Water Res.*2003; 37(18): 4513-4523. https://doi.org/10.1016/S0043-1354(03)00378-6

[19] Can OT, Kobya M, Demirbas E, Bayramoglu M. Treatment of the textile wastewater by combined electrocoagulation. *Chemosphere.* 2006; 62: 181-187. https://doi.org/10.1016/j.chemosphere.2005.05.022

[20] Hasson D, Lumelsky V, Greenberg G, Pinhas Y, Semiat R. Development of the electrochemical scale removal technique for desalination applications. *Desalination* 2008; 230: 329-334 https://doi.org/10.1016/j.desal.2008.01.004.

[21] Hakizimana JN, Gourich B, Chafi M, Stiriba Y, Vial C, Drogui P, Naja J. Electrocoagulation process in water treatment: a review of electrocoagulation modeling approaches. *Desalination* 2017; 404: 1-21, https://doi.org/10.1016/j.desal.2016.10.011.

[22] Moussa DT, El-Naas MH, Nasser M, Al-Marri MJ. A comprehensive review of electrocoagulation for water treatment: potentials and challenges. *J EnvironManage.* 2017; 186: 24-41, https://doi.org/10.1016/j.jenvman.2016.10.032

[23] Lin SH, Wu CL. Electrochemical removal of nitrite and ammonia for aquaculture. *Water Res.* 1996; 30: 715-721, https://doi.org/10.1016/0043-1354(95)00208-1

[24] Malakootian M, Mansoorian HJ, Moosazadeh M. Performance evaluation of electrocoagulation process using iron-rod electrodes for removing hardness from drinking water. *Desalination* 2010; 255: 67-71. https://doi.org/10.1016/j.desal.2010.01.015

# Tehnologija elektrokoagulacije kao nova i napredna tehnologija za buduće izazove u postrojenjima za prečišćavanje vode u industriji čelika

**Jovana Gradinac i Aleksandar Jovović**

*Univerzitet u Beogradu, Mašinski fakultet, Beograd, Srbija*

(Stručni rad)

*Izvod*

Voda je osnovna životna potreba, i može se činiti nezamislivim zamisliti život bez nje. Uticaj na životnu sredinu, zajedno sa socijalnim i ekonomskim uticajem konvencionalnih i tradicionalnih tretmana vode u postrojenjima u industriji čelika i neizbežnom činjenicom nestašice vode, vode i pokreću prelazak na novu paradigmu u tretmanima vode. Ovo istraživanje je imalo za cilj da ispita efikasnost procesa elektrokoagulacije i jedinice za flotaciju rastvorenog vazduha za uklanjanje različitih nečistoća u vodi iz fabrike za proizvodnju čelika. Tokom proteklih decenija, elektrokoagulacija je prihvaćena kao efikasna i obećavajuća alternativna tehnologija u oblasti prečišćavanja vode. Elektrokoagulacija tehnika je usko povezana sa hemijskom koagulacijom, koja uključuje snabdevanje koagulantnih jona primenom električne struje na žrtvenu anodu (napravljenu od aluminijuma ili gvožđa) smeštenu u procesni rezervoar. Glavni fokus istraživanja je stavljen na ukupne rastvorene materije i provodljivost vode. U tradicionalnim sistemima, ukupne rastvorene materije i provodljivost vode su jedan od parametara na koje ne mogu uticati hemijske jedinice za doziranje. Specifični cilj je bio da se razumeju parametri koji utiču na efikasnost procesa elektrokoagulacije, tako da se utiče na ukupan sadržaj rastvorenih materija i smanjenje zaostalih neorganskih i organskih nečistoća, održavajući neophodnu ravnotežu vode.

*Ključne reči:* Ušteda vode, inovativna rešenja, zelena industrija, reciklaža, elektrohemijski proces

# Implementation of emergency measures to improve the efficiency of nickel removal from water at the existing water treatment plant

**Zorana Z. Radibratović[1], Biljana B. Cakić[1], Marija N. Vilotijević[2], Ivona R. Radović[3] and Mirjana Lj. Kijevčanin[3]**

[1]*Jaroslav Černi Water Institute JSC, Belgrade, Serbia*
[2]*Public Utility Company "Waterworks Zlatibor", Čajetina, Serbia*
[3]*University of Belgrade, Faculty of Technology and Metallurgy, Belgrade, Serbia*

*Abstract*

In this paper, based on the data of the Ribnica accumulation (Serbia), and the required quality of raw and treated water, an optimal solution for improving and optimization of the technology of water purification to drinking quality at a water treatment plant (WTP) in Zlatibor, Serbia, was proposed to ensure maximum efficiency and flexibility in system operation. Analysis of water quality has shown that after the treatment at the plant, all parameters were within the respective maximum available concentrations (MAC) stipulated by the Rulebook on the hygienic suitability of potable water of the Republic of Serbia, except for the nickel content. The paper presents the results of the nickel removal using multiple laboratory tests as well as at the WTP to achieve the best procedure for water treatment. In accordance with the results obtained the water quality problem in terms of the nickel removal was solved and the required effects are obtained (nickel content below the MAC, *i.e.* <0.02 mg dm$^{-3}$)

*Keywords:* Jar test; aluminium-sulphate; polyaluminium chloride; flocculation.

*Available on-line at the Journal web address:* http://www.ache.org.rs/HI/

ORIGINAL SCIENTIFIC PAPER

**UDC: 669.24-045.38: 628.16**

*Hem. Ind.* **79(1)** 9-17 (2025)

## 1. INTRODUCTION

Zlatibor is a mountain that covers an area of about 1000 km$^2$, largely located in the municipality of Čajetina, Serbia. Thanks to the specific climate and characteristic air currents, Zlatibor has developed into a prominent summer and winter tourist centre with the longest tourist tradition among the mountains in Serbia. The entire area of the municipality of Čajetina is provided with potable water by the public utility company (PUC) "Waterworks Zlatibor", which uses water from the river Crni Rzav, accumulated in the water supply reservoir Ribnica, with a volume of 3.5 million m$^3$. Water flows by gravity from the water intake to the water treatment plant (WTP) located directly below the dam. The WTP was built in 1972 with a capacity of 25 dm$^3$ s$^{-1}$.

Since the number of houses for rent, hotels and other accommodations was growing very quickly along with the number of visitors, the municipality gradually expanded the capacity of the plant in order to ensure the sufficient amount of drinking water, so that the capacity first was increased to 50 L s$^{-1}$, then to 80 L s$^{-1}$, to finally reach the current capacity of 150 L s$^{-1}$, by adding individual technological units.

The task considered in this paper estimates the possibility to reduce the concentration of nickel in the treated water below the maximum available concentration (MAC) of 0.02 mg dm$^{-3}$ [1], by applying the currently present technologies at the WTP. Since nickel had not been identified in raw water at the time of WTP implementation, the existing technology is not suited for nickel removal.

Nickel, a metal pollutant, is widely used by various modern industries like electroplating, tanning, textiles, etc. resulting in discharge and accumulation in large quantities into the environment. Nickel exists in the environment in the form of a divalent cation, which is very toxic. Adsorption is one of the leading techniques to remove nickel from wastewater in which pH has a significant effect on the process [2]. For metals such as nickel and lead, adsorption increases as pH rises, with the highest adsorption observed just before precipitation begins. However, for other metals,

---

Corresponding authors: Zorana Z. Radibratović, Jaroslav Černi Water Institute JSC, Belgrade, Serbia

Paper received: 25 April 2024; Paper accepted: 16 December 2024; Paper published: 4 February 2025.

E-mail: zole.radibratovic@gmail.com

https://doi.org/10.2298/HEMIND240425024R

like chromium VI, adsorption is not directly related to precipitation [3]. Adsorption techniques for nickel removal primarily rely on the use of solid adsorbents that interact with metal ions, either through electrostatic forces, ion exchange, or chelation. A variety of adsorbents have been studied, including activated carbon [4], natural materials like chitosan [5], and synthetic adsorbents such as mesoporous silica [6]. Another promising class of adsorbents for nickel removal is metal-organic frameworks (MOFs), which are highly porous materials with tunable structures and functional groups that facilitate selective ion adsorption [7]. MOFs have shown remarkable efficiency in removing nickel from aqueous solutions due to their high surface area, chemical stability, and the possibility of functionalizing their surfaces for enhanced adsorption performance [8]. Various processes for nickel removal from water solutions were investigated along with parameters affecting the removal rate and efficiency and various adsorbents such as Jordanian natural zeolite [9]. Powdered activated carbon has been also used to enhance nickel removal from soil, in the case of ground water, as well as effective removal of nickel has been achieved using chelating ion exchange resins [10]. Other experiences have shown that nickel ions could be significantly adsorbed on cationic exchange resins where the removal from aqueous solutions depends on the solution pH, adsorbent dose, contact time and initial nickel concentration [11]. Removal of nickel ions from aqueous solutions was also achieved by using ferric chloride ($FeCl_3$) coagulant and the precipitate formation during the coagulation process at pH levels 7 and 8 was accurately represented by classical adsorption isotherms [12]. Based on the available data on the water accumulation and the quality of raw and treated water, an initial proposal for solving water quality in terms of nickel content in water is given in this paper

The water quality at Ribnica acculmulation (Zlatibor) was assessed by the City Institute for Public Health from Belgrade, Serbia, and the Institute for Public Health "Batut" from Belgrade, Serbia, with the focus on content of metals. The monitoring also included other components required by Rulebook on the hygienic suitability of drinking water [1].

## 2. MATERIALS AND METHODS

### 2. 1. Existing conditions of the water treatment plant

Although the water treatment plant in Čajetina, Serbia, with the original settling tank and filters has been in operation since 1972 (50 years), it is still in relatively good condition in terms of construction so that it functionally maintains the quality of the treated water regardless of the equipment, continuously exploited over the long period of time. The current capacity of the plant is 150 $dm^3\ s^{-1}$ and the process line includes clarification (coagulation and flocculation), sedimentation, filtration on sand filters and disinfection with chlorine [13].

The chemicals used in the clarification process are aluminium-sulphate ($Al_2(SO_4)_3$) and polyelectrolyte. Clarification takes place in a lamellar clarifier (which was the last one built for a capacity of 80 to 90 $dm^3\ s^{-1}$ and two circular clarifiers, after which the clarified water is taken to gravity sand filters (8 in total), and from there into a treated water reservoir where it is disinfected. After the treatment, water is distributed through the water supply network to consumers.

Specific details on water treatment are as follows. Raw water is collected from the accumulation Ribnica and through a distribution chamber it is introduced into the coagulation chamber, where aluminium-sulphate is dosed at concentrations of 50 to 80 mg $dm^{-3}$, after which water is distributed to the first stage (Stage I) of flocculation, where polyelectrolyte is dosed at concentrations of 0.2 to 0.5 mg $dm^{-3}$. The water with the prepared flocs is distributed into the lamellar clarifier, which is sized to optimally work at 80 to 90 $dm^3\ s^{-1}$, while part of it is diverted to two circular clarifiers (one was transformed into a lamellar one with a capacity of approxatwly 40 $dm^3\ s^{-1}$ by installing lamellas), while the other receives only a small amount of water from the second stage (Stage II) of flocculation.

After sedimentation, water is distributed to eight gravity sand filters with a constant level during filtration. Clean, non-chlorinated water is used for washing filters at the plant. The filters are washed with air and water at the required intervals and lengths depending on the quality of the raw water. After filtration, the water is distributed to the treated water tank, where final disinfection is performed by chlorination.

Building for preparation of the chemicals is equipped with tubs with mixers for preparation of aluminium-sulphate solutions, as well as a modern compact unit for preparation and dosing of polyelectrolytes.

At a WTP internal laboratory chemical analyses of water are performed every 3 h, comprising analyses of raw water, water from all sedimentation tanks, after each filter, and treated water. Analyses include temperature measurement, determination of pH value, turbidity, residual chlorine, nitrite, nitrate, sulphate, organic matter, and electrical conductivity. In addition, regular controls are carried out by the Institute for Public Health from Užice, Serbia, in accordance with the Rulebook on the hygiene of drinking water of the Republic of Serbia. Bearing in mind that the water taken from the reservoir has an elevated nickel content, the laboratory was equipped with adequate equipment for measuring the Ni concentration in water.

## 2. 2. Water quality

Reservoir "Ribnica" is one of the smaller reservoirs and is quite protected, considering that it is in the rural part of Zlatibor, far from settlements and human impact. It is very important to maintain and use the reservoir "Ribnica" primarily for water supply purposes, considering that the tourist center is constantly developing and the need for healthy drinking water is the basis of the system functioningThe consumption of $KMnO_4$ (up to 40 mg dm$^{-3}$) and turbidity (up to 10 mg dm$^{-3}$) exceeded the MAC values in raw water. However, following the treatment process, these parameters were within the MAC range.

The consumption of $KMnO_4$ in the raw water in the reservoir was elevated to approximately 20 mg dm$^{-3}$, (MAC = 8 mg dm$^{-3}$), while the ammonia concentration was approx. 0.2 mg dm$^{-3}$ (MAC = 0.1 mg dm$^{-3}$). In addition, the nickel concentration was increased to about 0.04 mg dm$^{-3}$ (MAC = 0.02 mg dm$^{-3}$). Turbidity of the raw water is slightly elevated, at around 2 NTU in the measurement period (December 2015.). Quality of the water is presented in Table 1 for several sampling points, for the measurements performed in 2016 [14].

*Table 1. Quality of raw and treated water in the Ribnica accumulation*

| | Raw water | Treated water | Settling tank I | Settling tank II | Settling tank III |
|---|---|---|---|---|---|
| pH | **6.73** | **6.28*** | | | |
| Electric conductivity, mS cm$^{-1}$ | 128 | 170 | | | |
| Colour, °Pt-Co | **55** | 1 | | | |
| Turbidity, NTU | **3.35** | 0.68 | | | |
| Ammonium ion content, mg N dm$^{-3}$ | **0.17** | < 0.02 | | | |
| Total organic carbon, mgC dm$^{-3}$ | **5.64** | 1.53 | | | |
| Content of iron, mg dm$^{-3}$ | **0.41** | 0.02 | 0.05 | 0.04 | 0.07 |
| Content of nickel, μg dm$^{-3}$ | **46.4** | **25.2** | **26.6** | **26.1** | **27.9** |

*Values above MAC are bolded

The pH value, colour, ammonium ion, organic matter, iron, and nickel are among the physicochemical characteristics that are different from MAC in raw water. Except for nickel, which was still elevated at the concentration of about 0.025 mg dm$^{-3}$, all parameters after the treatment were within the MAC limits outlined by the Rulebook. Thus, an intervention was made to address the treated water quality according to this parameter using technology that is now available but not designed to remove nickel.

## 2. 3. Experimental section

In the Laboratory Jaroslav Černi at Water Institute Jaroslav Černi (JCWI) and the laboratory at the WTP "Zlatibor", during 2016 numerous tests and analyses were performed to achieve the required effects in terms of reducing nickel in water in the shortest possible time. Based on tests and analyses at laboratory conditions, guidelines were obtained in which directions for the structuring of the process treatment were outlined to overcome the problem with the increased nickel concentration in water. Accordingly, activated carbon powder and lime were dosed into the system to raise the pH to create a suitable environment for nickel removal. Many tests and dosing combinations were performed in the laboratory as well as at the WTP itself, from which numerous samples were taken to compare the obtained results, all with the aim of system reliability. The performed tests included dosing of only aluminium-sulphate, then dosing of lime and activated carbon before aluminium-sulphate, as well as dosing of ferry-chloride ($FeCl_3$), with and without the dosing of lime, *etc*.

Given the specificity of the water quality, and addition of innovation into the current system without the need for plant reconstruction, each modification represented a unique task for the participants in this effort. This paper presents two selected series of performed tests to optimize water treatment in terms of nickel removal.

Jar testing is a method that simulates a segment of the water treatment process, offering system operators a reliable understanding of how a treatment chemical will interact with a specific type of raw water. Since it mimics full-scale operation, system operators can use jar testing to help determine which treatment chemical will work best with their system's raw water. Jar testing entails adjusting the number of treatment chemicals and the sequence in which they are added to samples of raw water held in jars or beakers. The sample is then stirred so that the formation, development, and settlement of flocs can be observed just as it would be in the full-scale treatment plant (floc forms when the treatment chemicals react with material in the raw water and clump together).

To identify the ideal floc size for a certain plant, the operator then conducts several tests to examine the effects of varying concentrations of flocculation agents at various pH levels [15].

In addition to the jar tests, the experiments included a filter column through which selected samples were passed to complete the treatment process. Fixed-bed column experiments were conducted using columns of 2.54 cm internal diameter and 36 cm length. The columns were packed with anthracite - sand media.

After the preparation of the samples, the required two sets of jar testing and analysis were performed, one in the laboratory of the JCWI and the other in the laboratory of the PUC "Waterworks". Measurement of Ni content was done on ICP-OES apparatus which is a highly sensitive and accurate method for detecting heavy metals in a sample. ICP-OES stands for Inductively Coupled Plasma Optical Emission Spectroscopy.

### 2. 3. 1. Series 1 jar tests - JAR 1

Water was passed through a column of filler (sand/anthracite) as an addition to jar testing, and this type of mini treatment simulated the treatment at the plant. Jar tests and analysis have been performed for the first series of samples (A to F) termed JAR 1 with applied chemicals and doses, given in Table 2.

*Table 2. Applied chemicals during experiments in the laboratory of JCWI for series JAR 1*

| | Dose concentration, mg dm$^{-3}$ | | | | | |
|---|---|---|---|---|---|---|
| | Sample A | Sample B | Sample C | Sample D | Sample E | Sample F |
| Lime | 20 | 30 | 40 | 15 | 15 | 15 |
| Aluminium-sulphate (8 wt.%) | 55 | 55 | 55 | 45 | | |
| Polyaluminium chloride (10 wt.%) | | | | | 15* | 15** |
| Polyelectrolyte (0.1 wt.%) | 0.5 | 0.5 | 0.5 | 0.3 | 0.3 | 0.3 |

*Producer AluStar, Italy [13], **Producer Donau, Germany [13]

The general procedure for jar testing and filtration was:

- filling the appropriate number of 1000 ml transparent jars with well-mixed raw water
- placing the filled jars on a stirrer, with the paddles positioned identically in each beaker
- adding the chemicals as per the sample number for each of the series
- continuing mixing at a speed of 120 to 50 rpm for 3 min after the last chemical dosing
- continuing mixing the samples at a speed of 90 rpm for 5 min
- continuing mixing the samples at a speed of 45 to 60 rpm for 10 min
- allowing the samples to settle for 40 to 60 min
- decanting the clarified water into another beaker without disturbing the settled sludge at the bottom
- filtering the decanted water of the selected samples through a column with a filtering medium,
- analyzing the filtrate samples for the required parameters.

All experiments were conducted more than 30 times.

### 2. 3. 2. Series 2 jar tests - JAR 2

Jar tests and analyses have been performed for the second series of samples (1 to 9) termed JAR 2**,** applied chemicals and doses used are shown in Table 3. Water again was passed through a column with anthracite/sand media as an addition to jar testing. Additional test chemicals were used in this series comprising powdered granulated activated carbon (GAC), polyaluminium chloride (PAC), and ferric chloride ($FeCl_3$).

*Table 3. Applied chemicals during experiments in the laboratory of PUC for series 2*

| | Dose concentration, mg dm$^{-3}$ | | | | | | | | |
|---|---|---|---|---|---|---|---|---|---|
| | Sample 1 | Sample 2 | Sample 3 | Sample 4 | Sample 5 | Sample 6 | Sample 7 | Sample 8 | Sample 9 |
| Lime | 20 | 20 | 20 | 20 | 20 | 25 | 20 | 20 | 20 |
| GAC (0.75 %) | 7.5 | 0 | 0 | 7.5 | 7.5 | 0 | | | |
| Aluminium-sulphate (8 wt.%) | 55 | 55 | 55 | 55 | 55 | 55 | | | |
| PAC (10.0 wt.%)* | | | | | | | | 10 | 15 |
| $FeCl_3$ (2.0 wt.%) | | | | | | | 40 | | |
| PE (0.1 wt.%) | 0.5 | 0.5 | | 0.5 | 0.5 | 0.5 | 0.3 | 0.3 | |

*Producer AluStar, Italy [13]

The general procedure for jar testing and filtration through the column of anthracite and sand media was the same as in the previous testing.

Based on the obtained results of the laboratory tests, the improvement of treatment was started by the direct application of measures in the process line at the WTP.

## 3. RESULTS AND DISCUSSION

### 3. 1. JAR 1 test

The results of the JAR 1 test are shown in Table 4.

*Table 4. Results of the JAR 1 test*

| Parameter | pH | Turbidity, NTU | Concentration, mg dm$^{-3}$ | | Removal, % |
|---|---|---|---|---|---|
| | | | $KMnO_4$ | Ni | |
| Raw water | **7.64** | **3.5** | **23.50** | **0.040** | |
| A set | 8.9 | 0.8 | 8.91 | **0.023** | 43 |
| B set | 9.09 | 0.7 | 15.91 | **0.027** | 33 |
| C set | 9.28 | 0.5 | 19.73 | **0.028** | 30 |
| A anthracite / sand - through column | 6.74 | 0.3 | 8.90 | **0.022** | 45 |
| B anthracite / sand - through column | 6.69 | 0.26 | 8.91 | **0.024** | 40 |
| C anthracite/sand - through column | 7.53 | 0.42 | 13.05 | 0.018 | 55 |
| D set | 8.69 | 0.35 | 10.82 | **0.024** | 40 |
| E set | 8.76 | 0.25 | 13.05 | **0.022** | 45 |
| F set | 8.61 | 0.35 | 7.00 | **0.024** | 40 |
| D sand - through column | 7.46 | 0.19 | 11.46 | **0.023** | 43 |
| E sand - through column | 7.44 | 0.18 | 11.46 | **0.022** | 45 |

*Values above MAC are bolded

The results of the tests conducted show a significant reduction in the nickel content, but again the obtained values are above the MAC. The samples in which aluminium-sulphate was dosed as a coagulant performed better compared to those in which PAC was dosed. The sample termed C anthracite/sand showed the best results, where all parameters were below MAC including nickel (0.018 mg dm$^{-3}$) with the removal of 55 % compared to the content in raw water. The sample termed C involved dosing of 40 mg dm$^{-3}$ of lime to raise the water pH to 9.28, followed by dosing of 55 mg dm$^{-3}$ of aluminium-sulphate (8 wt.% solution) and 0.5 mg dm$^{-3}$ of polyelectrolyte (0.1 wt.% solution). The pH of water after filtration was 7.53, which is significantly lower than the value recorded after lime dosing, indicating good consumption and reaction of the added chemicals.

### 3. 2. JAR 2 test

Results of the performed analysis in the JAR 2 test are shown the Table 5.

The results of the tests conducted in JAR 2 series show a significant reduction in the nickel content. The samples in which ferric chloride was added were unsuccessful in terms of nickel removal, and the water quality decreased in terms of the other monitored parameters as well. Also, the addition of activated carbon in some samples did not significantly contribute to the improvement in terms of nickel removal.

*Table 5. Results of the JAR 2 test*

| Parameter | pH | Turbidity, NTU | KMnO$_4$ | Ni | Removal, % |
|---|---|---|---|---|---|
| | | | Concentration, mg dm$^{-3}$ | | |
| Raw water | 7.56 | **2.3** | **22.9** | **0.037** | |
| Sample 1 | 7.58 | 0.70 | **15.0** | **0.023** | 38 |
| Sample 2 | 7.56 | 0.73 | **8.9** | **0.025** | 33 |
| Sample 3 | **8.86** | 0.28 | 8.0 | **0.021** | 43 |
| F1 - through column | 7.50 | 0.55 | **14.3** | 0.018 | 51 |
| F2 - through column | 7.65 | 0.38 | **8.9** | 0.014 | 62 |
| F3 - through column | 7.65 | 0.23 | **9.2** | 0.015 | 60 |
| Sample 4 | 7.67 | 1.25 | 8.3 | **0,026** | |
| Sample 5 | 7.56 | - | - | - | |
| Sample 6 | **8.78** | - | - | - | |
| F4 - through column | 7.30 | 2.1 | **15.7** | - | |
| F5 - through column | 7.59 | 0.88 | **12.3** | **0.027** | 27 |
| F6 - through column | 7.38 | 0.38 | 8.0 | 0.014 | 62 |
| Sample 7 | **8.9** | 4.0 | **21.2** | **0.039** | |
| Sample 8 | **8.79** | 0.47 | **14.9** | **0.025** | 32 |
| Sample 9 | **8.81** | - | - | - | |
| F7 - through column | 7.4 | **4.0** | **19.0** | - | |
| F8 - through column | 7,53 | 0.45 | **16.4** | **0.022** | 40 |
| F9 - through column | - | - | - | - | |

*Values above MAC are bolded

The samples termed F2 and F6 gave the best results, as all the parameters were below MAC, especially the nickel content ranging from 0.014 to 0.018 mg dm$^{-3}$, with the removal up to 60 % compared to the content in raw water. The sample termed Sample 2 involved the dosing of 20 mg dm$^{-3}$ of lime to raise the water pH, followed by dosing of 55 mg dm$^{-3}$ of aluminium sulphate (8 wt.% solution) and 0.5 mg dm$^{-3}$ of polyelectrolyte (0.1 wt.% solution). The water pH after filtration was 7.65, indicating again good consumption and reaction of the added chemicals. The sample termed Sample 6 involved dosing of 25 mg dm$^{-3}$ of lime and same dosages of aluminium-sulphate and polyelectrolyte solutions. The water pH after filtration in this case was 7.38 similarly as in the previous case.

Since samples Sample 5, Sample 6 and Sample 9 did not precipitate, the analyses were not continued. The sample F7 still contained a significant amount of organic matter, which is the reason the concentration of nickel was not measured.

Based on the results of the experiments, emergency measures were implemented at the WTP by applying certain chemicals directly to process line. The experimental results indicated that the water pH and its precise adjustment, as well as the use of aluminium-sulphate as a coagulant, play a significant role in nickel removal. The high nickel removal was achieved because of the formation of $Al(OH)_3$ due to the reaction between the aluminum plates and water which has a large surface area to adsorb organic and inorganic materials and able to capture colloidal particles. In addition, the high removal efficiency could be achieved due to the hydroxide precipitation reaction mechanism as a result of basic condition (pH 8.5) which increased the precipitation of Nickel.

Biosorption capacities for heavy metals are highly dependent on pH, with adsorption increasing as the solution pH rises. At lower pH values, the total surface charge of the cells becomes positive, and the presence of H+ ions reduces the access of metal ions to the surface functional groups due to repulsive interactions, thereby decreasing the metal removal efficiency. Below pH 3, nickel adsorption decreases, likely due to competitive interactions with hydronium ions ($H_3O^+$). Furthermore, at elevated pH levels, the formation of insoluble hydroxyl species leads to nickel precipitation. Consequently, cationic metal biosorption is reduced at pH 7, most likely due to chemical precipitation. Sorption studies above pH 7 were not meaningful due to the formation of insoluble products, which aligns with the solubility products of metal hydroxides [16]. pH also influences processes such as hydrolysis, complexation with organic or inorganic ligands, precipitation, and the availability of toxic metals for biosorption. Additionally, pH affects the ionization and activity of functional groups in the biomass, particularly carboxylic groups [17].

The results of the application of selected chemicals in the WTP are given in Table 6 where the results show the water pH values and nickel concentrations after each of the 8 sand filters at the WTP.

*Table 6. Results after application of the improvement measures at the maximum flow rates at the plant .*

| Parameter | pH in 12 h | pH in 14 h | pH in18 h | Ni concentration, mg/dm$^3$ | Ni removal, % |
|---|---|---|---|---|---|
| Raw water | 7.1 | 7.1 | 7.2 | 0.045 | |
| F1 | 7.24 | 7.21 | 7.85 | 0.020 | 55 |
| F2 | 7.25 | 7.16 | 7.78 | 0.013 | 71 |
| F3 | 7.28 | 7.30 | 7.98 | 0.010 | 78 |
| F4 | 7.34 | 7.23 | 8.06 | 0.020 | 55 |
| F5 | 7.40 | 7.29 | 8.08 | 0.015 | 67 |
| F6 | 7.35 | 7.34 | 8.14 | 0.018 | 60 |
| F7 | 7.34 | 7.38 | 8.05 | 0.019 | 58 |
| F8 | 7.35 | 7.43 | 8.06 | 0.010 | 78 |

The obtained results show high degrees of nickel removal from raw water, which range up to 78 %, which is an excellent achievement. The problem during the application of emergency measures with lime dosing and fine pH adjustment is the high concentration of lime, since this solution creates problems in water, primarily in the filters, where they become clogged and require more frequent washing. The increase in the water pH after filtration over time is caused by the untimely reduction of lime dosage before the filters to correct the pH in relation to the reduction in nickel concentration.

In the treated water reservoir, an excellent result was recorded in terms of nickel concentration 0.016 mg dm$^{-3}$, which achieved the goal in terms of all parameters by the regulations in the Republic of Serbia.

In a relatively short period of time, results were obtained that gave effects in the removal of nickel, which means that the experiments were well conceived and performed, quickly leading to practical applications in the water treatment process. In this way, an improvement was achieved in the degree of removal of heavy metals from water, which represents a major problem in the treatment of potable water. The path has been opened in terms of nickel removal so that it is possible to obtain satisfactory purification effects by upgrading the system with new process units, such as activated carbon filters and very precise pH adjustment. For such a system to be sustainable, it is necessary to perform further laboratory testing to find an optimal way of correcting the pH value in such a way that the filters are not clogged.

The introduction of an improved technology that gave an effect and which has been applied since April 2016 is the dosing of a 0.1 % solution of granulated activated carbon powder into the raw water (the pH of the activated carbon must be greater than 8) before the dosing of aluminium-sulphate and polyelectrolyte, namely in doses of 10 to 15 g m$^{-3}$ and adding of lime in doses of 25 to 30 g m$^{-3}$ after clarification in a lamellar precipitator and in front of the filter with strict pH control that should range from 8.0 -8.5 in order to lower the nickel concentration below MAC (< 0.02 mg dm$^{-3}$) after the filter. The pH value was appropriate in the treated water tank, which made it possible for the level of organic matter to be below the MAC.

When the stability of the system was established, the nickel concentration dropped to 0.015 mg dm$^{-3}$ in the clean water reservoir. The analysis results were admirable, the nickel concentration values in water were below the MAC in all samples both at the plant and in the network.

At the beginning of July 2016, the water processing flow at the plant was increased due to the increased water consumption, resulting in a slight increase in the nickel content in the stages of the treatment process and therefore in the output water. Thus, the recommendation was to apply temporary measures to reduce the nickel content, which have already been tested from April to July 2016 leading to a successful reduction of nickel concentrations below the MAC value in the treated water, at a plant capacity of 80 to 90 dm$^3$ s$^{-1}$.

Numerous adjustments were made on the spot, during the emergency tests at the plant itself in July 2016, together with the Waterworks expert team, and the Ni content was kept within the MAC limits, even though the plant was working beyond its optimal capacity. This primarily referred to the clarification process, which is one of the key steps in lowering the Ni content in water with the existing technology. It should be mentioned that the applied methodology of chemical precipitation is an effective and by far the most widely used process for removing heavy metals [18]. Due to the large consumption of water and therefore the significant consumption of powdered carbon, the dosing of powdered carbon into the raw water was temporarily turned off and the dosing of lime before the filter was maintained to maintain the pH of the water around 8.5 [19]. Since dosing of lime causes a heavy load on the filters, causing frequent filter washing and thus a reduction in their service life, it is recommended to use sodium hydroxide instead of lime, although it is affordable and effective. Addition of sodium hydroxide, on the other hand, does not produce sediments and easily increases pH, and was successfully tested on site at laboratory conditions.

## 4. CONCLUSIONS

This work addressed a problem in a water treatment plant in the municipality Čajetina, Serbia. The water quality after the treatment in the plant did not meet the quality standards, so it was necessary to perform experiments to find an appropriate solution to primarily decrease the nickel content. Thus, two experimental series tests were conducted in two laboratories to determine methods of intervention to improve the water treatment process. The best results were obtained at the dosing of a 0.1 wt.% solution of granulated activated carbon powder into the raw water before the dosing of aluminium-sulphate and polyelectrolyte, namely at the doses of 10 to 15 g $m^{-3}$ and dosing of lime at 25 to 30 g $m^{-3}$ after clarification in a lamellar precipitator and in front of the filter, with strict pH control that should range from 8.0 to 8.5 in order to lower the nickel concentration below MAC (< 0.02 mg $dm^{-3}$) after the filter. The chosen dose of the 8 wt.% aluminium sulfate solution is 55 $mg \cdot dm^{-3}$, while the dose of the 0.1 wt.% polyelectrolyte solution is 0.5 $mg \cdot dm^{-3}$. The pH of the water after filtration is 7.38 which indicates consumption and reaction of the added chemicals. After applying this combination of chemicals, the nickel concentration decreased to 0.015 mg $dm^{-3}$, with a satisfactory pH value in the treated water.

## REFERENCES

[1] Rulebook on the hygienic suitability of drinking water. The Official Gazette of the FRY 42/98; 44/99; and Official Gazette of RS 28/19 (Pravilnik o ispravnosti vode za piće. Službeni glasnik RS 42/98; 44/99; 28/19; in Serbian) https://www.paragraf.rs/propisi/pravilnik-higijenskoj-ispravnosti-vode-pice.html

[2] Kutir P, College PG, Chakkey, J. Effect of pH on the removal of Ni (II). Int J Chem Sci. 2013; 11(3): 1493-1497. https://www.tsijournals.com/articles/effect-of-ph-on-the-removal-of-ni-ii.pdf

[3] Cruz-Lopes LP, Morgana M, Bruno E, Raquel PFG, Ideal pH for the adsorption of metal ions $Cr^{6+}$, $Ni^{2+}$, $Pb^{2+}$ in aqueous solution with different adsorbent materials. *Open Agric.* 2021; 6:115-123. https://doi.org/10.1515/opag-2021-0225

[4] Hala AH. Removal of heavy metals from wastewater using agricultural and industrial wastes as adsorbents. *HBRC J.* 2013; 9(3):276-282. https://doi.org/10.1016/j.hbrcj.2013.08.004

[5] Utkarsh U, Sreedhar I. Singh SA, Patel CM, Anitha KL, Recent advances in heavy metal removal by chitosan based adsorbents *Carbohydr Polym.* 2021; 251: 117000 . https://doi.org/10.1016/j.carbpol.2020.117000

[6] Enshirah D. Adsorption of heavy metals on functionalized-mesoporous silica. *Microporous Mesoporous Mater*. 2017; 247: 145-157. https://doi.org/10.1016/j.micromeso.2017.03.050

[7] Rasheed T, Ahmad N., Nabeel F, Anwar MT, Bilal M. Metal-organic frameworks for removal of heavy metals. In Nano-Bioremediation: Fundamentals and Applications (pp. 455-476). Elsevier; 2021 https://doi.org/10.1016/B978-0-12-823962-9.00014-3

[8] Guo L, Biao Z, Jing L, Zeying W, Shixing W, Tu H, Libo Z. A systematic review of metal organic frameworks materials for heavy metal removal: Synthesis, applications and mechanism. *Chem Eng J.* 2023; 460: 141710. https://doi.org/10.1016/j.cej.2023.141710

[9] Eman AA, Reyad A. Al Dwairi ZS, Removal of nickel (II) ions from water by Jordan natural zeolite as sorbent material. *J Saudi Chem Soc.* 2021; 25: https://doi.org/10.1016/j.jscs.2021.101233

[10] Gopal R, Neelam C, Tapan A, Nickel as a Pollutant and its Management. *Int Res J Environment Sci.* 2014; 3(10): 94-98. https://www.isca.me/IJENS/Archive/v3/i10/15.ISCA-IRJEvS-2014-189.pdf

[11] Senthil KP, Ramakrishnan K, Gayathri R, Removal of nickel (II) from aqueous solutions by ceralite IR 120 cationic exchange resins. J Eng Sci Technol. 2010; 5(2): 232-243. https://jestec.taylors.edu.my/Vol%205%20Issue%202%20June%2010/Vol_5(2)_232_243_P%20SENTHIL%20KUMAR.pdf

[12] Oleg LD, Irina RV, Galina ZS, Konstantin MN, Inna BV, Yulia KV, Alexander GY, Boris GP, Zilara FA, Coagulation removal of nickel (II) ions by ferric chloride. *Water Environ Res.* 2022; 94: e10827. https://doi.org/10.1002/wer.10827

[13] Jaroslav Černi Water Institute, Conceptual Design for WTP Zlatibor, 2016. (Technical documentation in Serbian)

[14] Jaroslav Černi Water Institute, Design for Constriction Permit for WTP Zlatibor, 2016. (Technical documentation in Serbian)

[15] Zane Satterfield PE, Jar Testing. Tech Brief, Publisher by The National Environmental Services Center. 2005; Volume 5 (1). https://www.nesc.wvu.edu/files/d/3cf372e5-ba40-450c-a3ad-cd774f4c3345/jar-testing.pdf

[16] Nadem ZM, Nadeem R, Asif HM, Biosorption of nickel from protonated rice bran. *J Hazard Mater.* 2007; 143: 478–85. https://doi.org/10.1016/j.jhazmat.2006.09.055

[17] Dash RR, Balomajumder C, Kumar A. Removal of cyanide from water and wastewater using granular activated carbon. *Chem Eng J.* 2009; 146: 40-413. https://doi.org/10.1016/j.cej.2008.06.021

[18] Inc. Metcalf & Eddy, Tchobanoglou G, Stensel H, Tsuchihashi R, Burton F, Abu-Orf M, Bowden G, Pfrang W. Wastewater Engineering: Treatment and Resource Recovery. 5th ed., New York, NY, USA: McGraw-Hill Education; 2014: 634. https://www.amazon.com/Wastewater-Engineering-Treatment-Resource-Recovery/dp/0073401188

[19] Jaroslav Černi Water Institute, Preliminary Design for WTP Zlatibor, 2016. (Technical documentation, in Serbian)

# Sprovođenje hitnih mera za poboljšanje efikasnosti uklanjanja nikla iz vode na postojećem postrojenju za prečišćavanje vode

**Zorana Z. Radibratović[1], Biljana B. Cakić[1], Marija N. Vilotijević[2], Ivona R. Radović[3] i Mirjana Lj. Kijevčanin[3]**

[1]*Institut za vodoprivredu „Jaroslav Černi“, Beograd, Srbija*
[2]*JKP “Vodovod” Zlatibor, Čajetina, Srbija*
[3]*Univerzitet u Beogradu, Tehnološko-metalurški fakultet, Beograd, Srbija*

(Naučni rad)

*Izvod*

Projektovanje postrojenja za prečišćavanje vode (PPV) podrazumeva kompleksnu analizu i primenu kriterijuma projektovanja zajedno sa praktičnim iskustvom. Osnovni kriterijumi standardnog projektovanja obuhvataju kapacitet, kvalitet sirove i prečišćene vode, lokaciju postrojenja za prečišćavanje vode i skup prihvatljivih, proverenih tehnologija. Kombinovanjem kriterijuma pouzdanosti sistema sa tehno-ekonomskim pokazateljima moglo bi se dobiti optimalno procesno rešenje za nova postrojenja, kao i za unapređenje procesa u postojećim postrojenjima. U ovom radu, na osnovu podataka iz akumulacije Ribnica, Srbija, i zahtevanog kvaliteta sirove i prečišćene vode, predloženo je optimalno rešenje za unapređenje i optimizaciju tehnologije prečišćavanja vode do kvaliteta za piće na PPV na Zlatiboru, Srbija, kako bi se osigurala maksimalna efikasnost i fleksibilnost u radu sistema. Analiza kvaliteta vode pokazala je da su nakon tretmana u postrojenju svi parametri bili u granicama odgovarajućih maksimalno dozvoljenih koncentracija propisanih Pravilnikom o higijenskoj ispravnosti vode za piće Republike Srbije, osim sadržaja nikla. U radu su prikazani rezultati uklanjanja nikla primenom višestrukih ispitivanja u laboratoriji i na PPV radi uspostavljanja najbolje procedure za tretman vode. Prema dobijenim rezultatima, rešen je problem kvaliteta vode u pogledu uklanjanja nikla i ispunjeni su zahtevani uslovi (sadržaj nikla ispod maksimalne dozvoljene koncentracije < 0.02 mg dm$^{-3}$).

*Ključne reči:* Jar test; aluminijum-sulfat; polialuminijum hlorid; flokulacija

# Experimental analysis of atmospheric corrosion of steel S235JR in industrial environment

**Jelena N. Stefanović[1], Zoran Mišković[2], Stevan Dimitrijević[3], Zlatko Marković[2] and Milan Spremić[2]**

[1]*Mining and Metallurgy Institute Bor, Bor, Serbia*
[2]*The University of Belgrade, Faculty of Civil Engineering, Belgrade, Serbia*
[3]*Innovation Center of Faculty of Technology and Metallurgy, Belgrade, Serbia*

*Abstract*

The aim of this study was evaluation of atmospheric corrosion of structural steel S235JR in an industrial environment. General corrosion testing was carried out for six months in the field, at selected atmospheric corrosion stations, near the Sulphuric acid plant, in the Electrolytic refining plant and next to the automatic air quality monitoring station in the city of Bor, Serbia. The results were compared with the standard specimens stored in the laboratory. The steel S235JR specimens were characterized regarding mechanical characteristics by tensile testing. With the aim of assessing the mutual effect of corrosion and polluted industrial environment meteorological parameters were also determined, as well as pollutants in the atmosphere (mainly $SO_2$). The X-ray diffraction method was used to identify the composition of corrosion products. Research within this work enabled a better understanding of the behavior of structural steel S235JR in which there was a reduction in load capacity due to corrosion. The corrosion rates obtained under each tested exposure condition showed noticeable differences. It was found that depending on the content of pollutants in the atmosphere and the location of the steel specimen, the corrosion products represented different compounds and solid phases.

*Keywords:* corrosion testing; atmospheric corrosion stations; corrosion products; $SO_2$; XRD analysis; standard coupon test

ORIGINAL SCIENTIFIC PAPER

**UDC: 691.714:621.78.019.84**

*Hem. Ind.* **79(1)** 19-30 (2025)

*Available on-line at the Journal web address:* http://www.ache.org.rs/HI/

## 1. INTRODUCTION

During winter months, the corrosion process proceeds at its fastest rate, due to an increase in the concentration of pollutants in the air, such as sulphur dioxide ($SO_2$), carbon dioxide ($CO_2$), chloride ions and dust. Industrial environments often involve different mixtures of these elements. Relative humidity, number of hours of sunshine, temperature of air, atmospheric pressure, as well as duration and frequency of rain are among key meteorological variables influencing the corrosion process. The effect of time and quantity of rain are very important for characterizing differences between indoor and outdoor corrosion [1]. Indoor humidity and temperature are largely influenced by the level of ventilation, air conditioning, heating, and thermal isolation [2]. Indoor corrosion intensifies at higher humidity degrees and is affected by the type and level of pollution. Indoor air is polluted from both external and internal sources. Typical indoor pollutants are $SO_2$, $NO_2$, HCl, $H_2S$, organic acids and particles [3]. In general, concentration of particles indoors is the total of those present inside and those brought in from outside.

This study focuses on deterioration of steel elements as a result of corrosion propagation because of the presence of corrosion agents in the industrial environment in the city of Bor, Serbia. Several atmospheric corrosion stations were used for the in-the-field corrosion testing over the period of 6 months. Selected places for corrosion testing were: (1) near the Sulphuric acid plant, close to air quality monitoring station in City park, (2) on the internal balcony above the Electrolysis plant (inside the building) and (3) on the roof of the Mining and Metallurgy Institute Bor, next to the automatic air quality monitoring station.

---

Corresponding authors: Jelena N. Stefanović, Institut za rudarstvo i metalurgiju Bor, Pariske komune 24, 11070 Novi Beograd
Paper received: 21 November 2024; Paper accepted: 13 March 2025; Paper published: 17 April 2025.
E-mail: jelena.stankovic@irmbor.co.rs
https://doi.org/10.2298/HEMIND241121002S

Steel S235JR was selected for assessment of the corrosion resistance by the analysis of mass loss and evaluation of mechanical properties of specimens after exposure to the tested environments in Bor for a certain period of time. Corrosion products taken from the specimens were subjected to X-ray diffraction (XRD) analysis. XRD analysis is often used in various corrosion studies, such as in improving the control of corrosion processes and preventing the impact of corrosion on water quality degradation in water distribution pipes [4]. Significant differences have been observed in the appearance of corrosion products formed on steel specimens kept in outdoor and indoor conditions.

To obtain a complete characterization of the atmosphere, and thus of the exposure conditions, meteorological data during six months in the period of the experiment duration were analyzed. The indoor conditions of the Electrolysis plant depend on the general environmental conditions of the site. Indoor relative humidity (RH) and temperature depend largely on the degree of ventilation. Pollution by $SO_2$ alone was considered in this study, being the most common and important corrosive agent. $SO_2$ indoors is expected to be 30 to 50 % lower than outdoors, as stated in literature [3]. Both mass loss and mechanical properties of the experimental specimens were measured.

Many authors have investigated degradation of mechanical properties of corroded steel. According to recent research, corrosion has reportedly been shown as having no influence on the chemical and mechanical properties of steel [5,6]. However, it clearly affects the reduction of yield plateau, ultimate stress and necking region. It was found that both the bearing capacity and ductile property of structural steel decreased as the corrosion rate increased [7,8].

Corrosion studies that have been carried out in outdoor conditions, were rarely accompanied with those carried out indoors at the same time. The main goal of this work is to provide a deeper insight into how corrosion in outdoor and indoor conditions affects the load-bearing capacity and durability of steel structures, whereby XRD analysis provides additional insight into the process of corrosion. A direct comparison between the corrosion rates of steel in an open atmosphere and in a closed one is presented in this paper.

## 2. EXPERIMENTAL

### 2. 1. Experiment preparation

The standard coupon test specimen was fabricated in accordance with the EN10002-1 standard, the thickness of the coupon for tensile strength testing was 4, 6 and 8 mm. The material used in this experiment was commercial steel S235JR (HBIS Group Serbia Iron & Steel, Serbia). In initial research by the same author [9], steel S235JR was tested on the standard plate 30x40x8 mm, by the use of inductively coupled plasma optical emission spectroscopy (ICP-OES), Ciros Vision (Spectro Analytical Instruments Inc., Germany), with the following chemical composition: 0.12 wt.% C, 0.012 wt.% Si, 0.27 wt.% Mn, 0.012 wt.% Cr, 0.003 wt.% Mo, 0.013 wt.% Ni, 0.005 wt.% P, 0.008 wt.% S, 0.036 wt.% Al, 0.041 wt.% Cu, 0.0003 wt.% B, 0.0006 wt.% Sn, 99.40 wt.% Fe and others in a small percentage.

### 2. 2. Atmospheric corrosion stations

Tests for corrosion resistance were conducted at atmospheric corrosion stations, under actual operating circumstances. These were carefully chosen locations within the industrial complex, where specimens are displayed, and corrosion-related changes are tracked.

In this study, atmospheric corrosion stations are selected for accelerated testing of Bor industrial zone. The industrial zone in Bor is in the very center of the city, so the Sulfuric acid plant is located near center of the town. The atmospheric corrosion stations were chosen next to air quality monitoring stations, in the City park and at the Mining and Metallurgy Institute Bor. The distance between these two locations is about 3 km. The automatic monitoring station in the City park is about 800 m away from the Sulfuric acid plant. This part of the study has been carried out in outdoor conditions. Another location was inside the Electrolytic refining plant (Figure 1). Steel specimens were exposed for 6 months in winter between November 2016 and May 2017. There were 6 specimens at each location, a total of 18, placed on a wooden frame, at an angle of 45° to the ground, horizontally, and facing south. It is frequently considered as the position where the specimen's greatest surface gets corroded [10,11]. In this research, there was an attempt to obtain the degradation of the material due to corrosion under real industrial conditions, in the winter months.

*Figure 1. Location of the stations across the industrial area of Bor: (1) near the Sulphuric acid plant; (2) inside the Electrolytic refining plant; (3) next to the automatic air quality monitoring station in the Mining and Metallurgy Institute Bor*

After exposure, corrosion products from all specimens, as well as from the reference specimen, were removed according to ISO 8407:2021 [12]. This standard specifies procedures for removal of corrosion products from metals and alloys, which are created on specimens for corrosion testing during their exposure to the corrosive media. On the test specimens, the products were first removed mechanically, and then chemically, for the duration defined in the standard. The procedures set out in this standard are intended to remove corrosion products without significant removal of the parent metal. To determine the mass loss of parent metal when removing the corrosion product, the parallel uncorroded, reference specimen is cleaned by the same procedure as the specimen under test. After removing the corrosion products, all specimens, 18 of them, were subjected to a standard coupon test.

### 2. 3. Standard coupon test

Standard coupon tests were conducted in this study to assess the mechanical properties, strength and the module of elasticity of specimens under different corrosion conditions. Standard coupon tests were carried out on a servo-hydraulic universal testing machine (Instron 1332 with Fast Track 8800 control system, Instron, USA) at a maximum load of 100 kN and an extensometer with a gauge length of 50 mm was installed in the middle of the specimen to measure the deformation during the standard coupon test.

### 2. 4. XRD analysis

XRD analysis was conducted to identify corrosion products formed at the three different exposure sites (Figure 1):

1. near the Sulphuric acid plant (AF)
2. inside the Electrolytic refining plant (EF)
3. next to the automatic air quality monitoring station in the Mining and Metallurgy Institute Bor (MP)

The X-ray diffraction was performed using a RIGAKU Ultima IV (Tokyo, Japan) diffractometer with Ni-filtered Cu $K\alpha$ radiation ($\lambda = 0.1540$ nm), with the X-ray tube operating at 40 kV and 40 mA. The XRD patterns of the corrosion products were recorded over the 5– 90° $2\theta$ range with a step of 0.02° and a scanning rate of 10° $\text{min}^{-1}$. The phase analysis was conducted using the PDXL2 software (version 2.0.3.0) [13].

### 2. 5. Meteorological parameters and atmospheric pollutants

Some of the most important meteorological parameters in Bor for the corrosion process are shown in Table 1.

*Table 1. Monthly average meteorological parameters (T is temperature, RH is relative humidity and TOW is the time of wetness) [14]*

| Measurement period | $T$ / °C | RH, % | TOW, h | Rainfall, $\text{mm m}^{-2}$ | Atmospheric pressure, kPa* |
|---|---|---|---|---|---|
| November 8th 2016 - December 8th 2016 | 6.9 | 70 | 168 | 50.0 | 97.63 |
| December 9th 2016 - January 8th 2017 | 2.5 | 69 | 192 | 7.4 | 98.41 |
| January 9th 2017 - February 8th2017 | 0.4 | 83 | 144 | 47.0 | 97.05 |
| February 9th 2017 - March 8th 2017 | 6.7 | 79 | 360 | 24.7 | 97.01 |
| March 9th 2017 - April 8th 2017 | 6.6 | 79 | 240 | 21.1 | 96.75 |
| April 9th 2017 - May 8th 2017 | 12.4 | 72 | 120 | 42.7 | 96.81 |

Time of wetness (TOW) was estimated from the number of hours per year that the relative humidity was equal to or above 85 % and the temperature exceeded 0 °C.

Average of $SO_2$ values in Table 2 are reported in the Annual report on air quality in the Republic of Serbia, Ministry of Environmental Protection, Environmental protection agency [15,16]. As can be seen, differences in $SO_2$ concentration are noticeable between these two stations.

*Table 2. Monthly average $SO_2$ deposition [15, 16]*

| Measurement period | $SO_2$ deposition, mg $m^{-2}$ | |
|---|---|---|
| | Air quality MP monitoring station | Air quality monitoring station in City park |
| November 8th 2016 - December 8th 2016 | 26.4 | 26.2 |
| December 9th 2016 - January 8th 2017 | 29.0 | 26.0 |
| January 9th 2017 - February 8th2017 | 54.1 | 66.8 |
| February 9th 2017 - March 8th 2017 | 24.7 | 59.3 |
| March 9th 2017 - April 8th 2017 | 20.4 | 43.6 |
| April 9th 2017 - May 8th 2017 | 16.0 | 42.3 |
| Calculated average value | 28.4 | 44.0 |
| The maximum measured value | 272.6 (measured on 01. 02. 2017) | 299.9 (measured on 01.05.2017) |

Environmental parameters that influence atmospheric corrosion, such as relative humidity, temperature and deposition rates, vary significantly between indoor and outdoor conditions.

The indoor conditions in the Electrolytic refining plant are near constant in terms of temperature, relative humidity and the concentration of pollutants in the air. Blowers were installed inside the Electrolysis plant, which permanently ventilated the facility. The temperature inside the plant ranged between 13 and 18 °C in the relevant period. The atmosphere also contained electrolyte aerosols. The electrolyte had the following composition: $H_2SO_4$ 1.7 mol $dm^{-3}$, $CuSO_4 \cdot 5H_20 \approx 160$ g $l^{-1}$, or about 40 g $l^{-1}$ of copper, and HCl 0.04 mol $dm^{-3}$. The higher humidity indoors, which was always higher than 80 %, was mainly influenced by the open electrolytic cells and a high electrolyte temperature (58 ± 2 °C).

## 3. RESULTS AND DISCUSSION

### 3. 1. X-ray diffraction analysis

The X-ray diffraction was performed on corrosion products removed from the specimens, one from each of the three locations. Main corrosion products of carbon steels are reported to be lepidocrocite (γ-FeOOH) and goethite (α-FeOOH) regardless of atmospheric conditions, even the industrial [17,18]. During the time of exposure, lepidocrocite is transformed to goethite, and $SO_2$ highly influences this process [19], which proceeds in several parallel and consecutive stages [20]. In these corrosion processes, magnetite ($Fe_3O_4$) and maghemite (γ-$Fe_2O_3$) are practically intermediates and are often detected by the XRD analysis. However, these minerals are hard to differentiate as a consequence of their almost identical crystalline structure [21]. They are usually close to the surface of the steel, leading to their identification but without determination of their quantity portion in the corrosion products. A percentage of the total identified crystalline products is given from a semi-quantitative estimate for each detected phase, where it could be expressed quantitatively.

The corrosion products of the first sample AF contain 57 wt.% lepidocrocite (γ-FeOOH) and 43 wt.% goethite (α-FeOOH) (Figure 2). The second sample EF contains 33 wt.% goethite (α-FeOOH), 20 wt.% rozenite ($FeSO_4(H_2O)_4$) and 47 wt.% jarosite ($KFe_3(SO_4)_2(OH)_6$) (Figure 3). The third sample MP contains 68 wt.% lepidocrocite (γ-FeOOH) and 32 wt.% goethite (α-FeOOH) (Figure 4). Magnetite ($Fe_3O_4$) and maghemite (γ-$Fe_2O_3$) are not quantified but detected in all three samples. Lepidocrocite was also identified in the EF specimen, although not quantified.

Figure 2 presents the XRD pattern for the sample AF exposed to industrial atmospheric conditions with a high $SO_2$ concentration (sulphuric acid plant). The diffractogram shows peaks of γ-FeOOH at the $2\theta$ angles of 14.10, 27.04, 36.48, 46.88, 52.98 and 60.98°; additionally, peak at 84.70° can also be attributed to the same compound. Moreover, the relative intensity of these peaks has the same pattern as the single high-purity crystal phase, further confirming its dominant presence. It is the primary component of the surface corrosion layer, with a content of 57 *vs.* 43 wt.% of α-FeOOH.

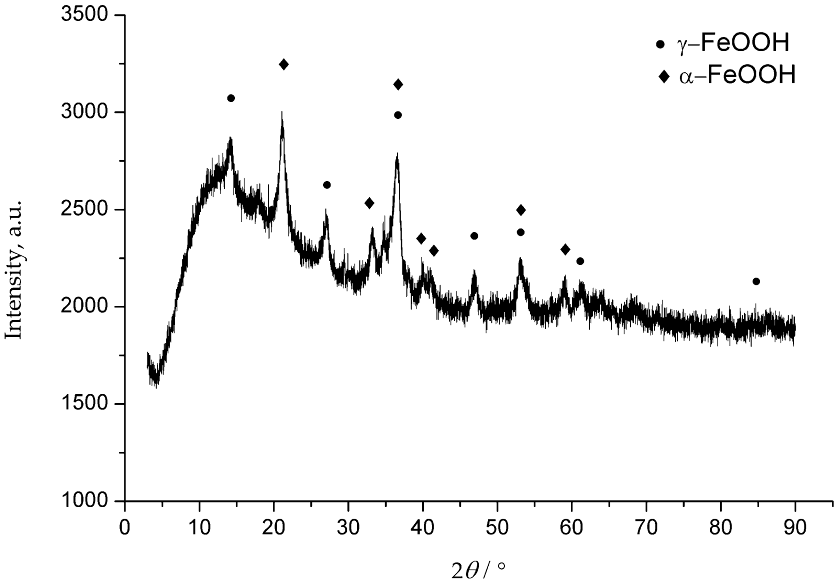

*Figure 2. X-ray diffractogram of corrosion products of steel S235JR after 6 months of exposure near the Sulphuric acid plant in Bor (AF)*

The ratio between these two variants of FeOOH is less favourable for the γ type of this iron oxyhydroxide in industrial atmosphere (at AF), than for a nonindustrial atmosphere (at MP) as a corrosion environment (Figure 4). This was expected due to the presence of higher $SO_2$ concentrations in the air (Table 2) that influence the transformation of lepidocrocite into goethite, since $SO_2$ dissolves the initially formed γ-FeOOH, promoting this phase transformation, as explained in other study [22]. In the diffractogram the presence of the peaks of α-FeOOH are also unquestionable and clear as well. These peaks are at the following positions 21.12, 33.18, 36.60, 39.86, 40.94, 53.12 and 59.16°. The presence of maghemite, peaks at 35.52° (overlapped with all other detected crystal phases), 53.46, 57.30 and 62.86°, and magnetite with peaks at 18.22 29.96 and 35.34° (overlapped with all other detected crystal phases), 62.56° have also been confirmed by XRD analysis. However, these minerals were in low quantities, practically as trace compounds.

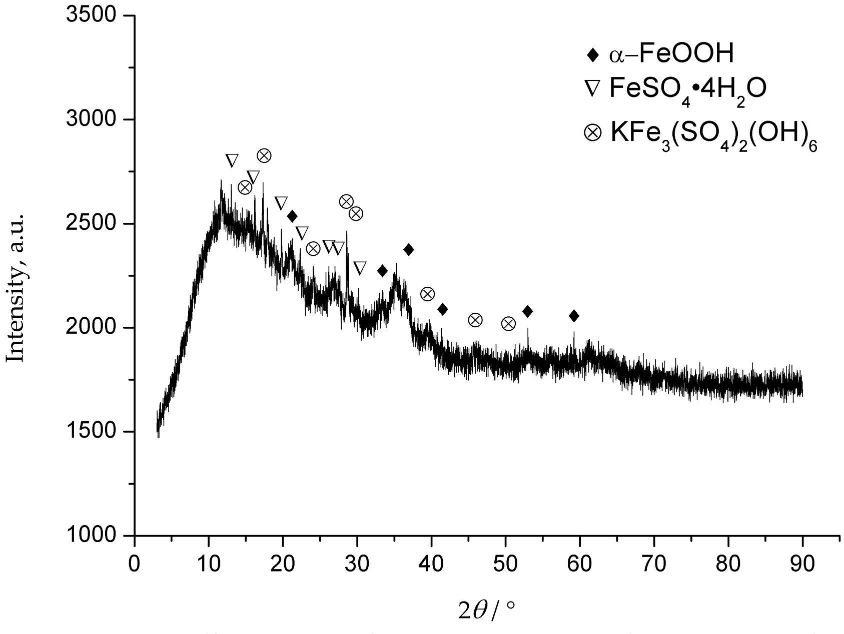

*Figure 3. X-ray diffractogram of corrosion products of steel S235JR after 6 months of exposure into the*

### *Electrolytic refining plant in Bor (EF)*

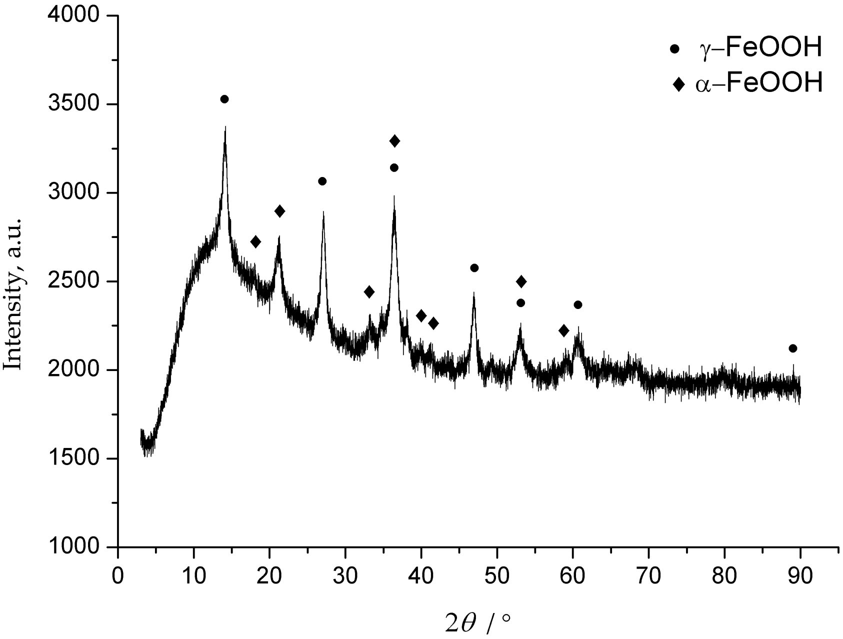

*Figure 4. X-ray diffractogram and corrosion products of steel S235JR after 6 months of exposure next to the automatic air quality monitoring station in Mining and Metallurgy Institute Bor (MP)*

Figure 4 shows the results of the XRD analysis of the steel exposed to relatively mild atmospheric conditions at MP in a six-month period. Corrosivity category for this atmosphere conditions is C2-C3 according to ISO 9223:2012 [23]. The XRD diffractograms in Figures 2 and 4 are relatively similar.. Two main constituents are gamma and alpha FeOOH. The first has diffraction peaks at 14.08, 27.08, 36.36, 46.90, 52.96, 60.74 and 89.06° which is almost identical to the appearance in Figure 2 with the better (closer to the reference) position of the peak at the highest $2\theta$ angle. Here, it should be noted that even a peak with a low intensity, at 18.0°, was detected. These more complete XRD patterns of these phases indicate even lower content of other crystal phases (maghemite and magnetite) and amorphous forms of the corrosion products compared to the influence of the industrial environment. The magnetite neither showed the peak at $2\theta$ angle of 18°, nor it was overlapped with the α-FeOOH. Nevertheless, maghemite peak at 30.16° was observed in the diagram. It has to be stressed that the semi-quantitative XRD determination of the relative contents is in accordance with the values of the peak intensities of γ-FeOOH when compared the Figures 2 and 4. Higher intensity of the main component of the corrosion layer corresponds to the higher relative content, as also reported by other authors [22].

The diffractogram in Figure 3 is the most complex of those three and much different from the other two. The main differences are a low content of γ-FeOOH and the presence of rozenite ($FeSO_4(H_2O)_4$) and jarosite ($KFe_3(SO_4)_2(OH)_6$) at the steel surface exposed in the specific industrial atmosphere at EF. The fumes of sulfuric acid and copper sulfate conditioned the appearance of these corrosion products. This presents a clear explanation for the appearance of rozenite, although additional considerations are needed to explain the presence of jarosite. The occurrence of jarosite as a product of atmospheric corrosion is not typical but was observed in marine atmospheric environments at the similar steel type (S235JR), where chloride ions with the presence of sulfate ions lead to precipitation of jarosite phase together with potassium, which originated mainly from the emissions from the oil-fired power plant and less from the marine aerosols [17]. Here, the proximity of the power plant operation and a flash smelter powered by oil in the period of exposure certainly had an influence. However, authors consider that potassium presence was primarily from the additives used in EF, being also constituents of aerosols.

The full pattern of α- FeOOH: 21.12, 33.22, 36.54, 41.36, 40.80, 53.04 and 59.22° ($2\theta$ angles) is present in Figure 3 and it is a second crystal phase by amount. Rozenite ($FeSO_4\times4H_2O$)) is a new crystal component characterized by the following peaks 13.02, 16.16, 19.80, 22.26, 26.18, 27.68 and 30.18°. It comprises about a fifth of the total corrosion products. Jarosite was the most abundant component of the corrosion layer (47 wt.% of the total quantity). All main peaks of this phase were present in the diffractogram: 15.02, 17.34, 24.32, 28.60, 28.82, 39.32, 45.96 and 49.98°. Although the presence of this crystal component is semi-quantitatively determined, its very high content was not expected and needs more research to be fully explained. γ-FeOOH was identified but only by the three peaks at 27.02, 36.34 and 61.04°, indicating the low content. Magnetite and maghemite also did not show a full XRD pattern in the diagram as well, and identification of these minerals was further complicated by some of the peaks being overlapped. Although not identified by the software, presence of magnetite ($Fe_3O_4$) in traces was possible, with pointed out peaks at 33.00 and 35.62° and partly at 49.54 and 54.16°. However, the other characteristic peaks were not visible in the XRD spectrum. Figure 3 shows also a few unmarked peaks that could indicate melanterite ($FeSO_4 \cdot 7H_2O$) and siderotil ($FeSO_4 \cdot 5H_2O$), but the presence of these minerals is not definite, although probable due to the sulphate presence.

Figures 2 to 4 show XRD patterns of corrosion products at the steel surface influenced by atmospheric conditions at three different locations. The X-ray diffraction patterns had a very similar look independent of the exposure conditions, except for the diffraction pattern of the specimen in the EF. The crystalline products formed in the rust layer are lepidocrocite (γ-FeOOH) and goethite (α-FeOOH), which are typical in the case of atmospheric corrosion of carbon steel, as it is found also in other studies [19,20]. The common feature is a very pronounced noise throughout the whole XRD diffractogram due to a high number (and amount) of amorphous components without a well-defined Bragg peak [18]. Additionally, it is influenced by crystal forms of compounds present at relatively low contents (under 5 wt.%).

### 3. 2. Corrosion rate

The mass loss for each group of the specimens with the same thickness after the exposure to different atmospheric conditions was calculated by:

$$\Delta m = m_0 \text{-} m - \frac{\sum_{i=1}^{2}(m_{0,i} \text{-} m_i)}{2} \tag{1}$$

where $\Delta m$ is the mass loss due to corrosion, $m_0$ is the initial mass prior to the corrosion test, $m$ is the mass after the corrosion test, $m_{0,i}$ and $m_i$ are the mass of control specimens before and after chemically cleaning, respectively. After the determination of the initial total surface area of specimen A and the mass loss during the test $\Delta m$, the average corrosion rate in the first year was obtained in accordance with ISO 9226:2012 [24]. The corrosion rates of S235JR steel are expressed as a mass loss per unit area over time ($r_{\text{corr}}$) or as a thickness reduction over time ($r_{\text{corr}}'$), given in Table 3.

*Table 3. Corrosion rate values and mass loss of steel specimens of different nominal thicknesses after 6 month exposure*

| Location | Nominal thickness, mm (2 specimens) | Initial mass, g | Mass loss, g | $r_{\text{corr}}$ / g m$^{-2}$ year$^{-1}$ | $r_{\text{corr}}'$ / µm year$^{-1}$ |
|---|---|---|---|---|---|
| 1. Sulphuric acid plant, AF (outdoor) | 4 | 253.66±1.05 | 6.41±0.02 | 68.39±0.28 | 8.71±0.04 |
| | 6 | 385.07±2.92 | 7.28±0.10 | 72.53±1.03 | 9.23±0.13 |
| | 8 | 520.14±1.57 | 7.64±0.16 | 71.33±1.45 | 9.07±0.18 |
| 2. Electrolytic refining plant, EF (indoor) | 4 | 253.76±0.69 | 0.82±0.01 | 8.73±0.12 | 1.11±0.01 |
| | 6 | 384.87±0.85 | 0.98±0.01 | 9.78±0.12 | 1.25±0.02 |
| | 8 | 512.52±12.36 | 0.97±0.11 | 8.98±1.00 | 1.14±0.13 |
| 3. The automatic air quality monitoring station in MMI Bor, MP (outdoor) | 4 | 254.95±2.09 | 2.03±0.04 | 21.60±0.41 | 2.75±0.06 |
| | 6 | 384.54±0.78 | 2.29±0.01 | 22.83±0.19 | 2.91±0.02 |
| | 8 | 517.15±5.74 | 1.95±0.52 | 18.15±4.86 | 2.31±0.62 |

The results of this study provide a direct comparison between the corrosion rates of steel specimens placed in outdoor and indoor conditions. In general, the indoor corrosion rates are relatively low (Table 3) due to the absence of precipitation and fog as well as higher indoor temperatures (often above the dew point), which significantly reduce the wetness duration. The outdoor corrosion rate is always higher than the indoor one, independent of the specimen thickness. Steel specimens placed outdoors are exposed to day/night change and occasionally to dew, rain, and/or fog.

At the same time, pollutant deposition is higher than that in indoor conditions. Corrosion products formed outdoor undergo significant changes as they frequently dry out during the day and absorb humidity at night, occasionally becoming wet due to rain, dew or fog.

### 3. 3. Mass and load bearing loss

Table 4 shows the reference values for etalon specimens, mass loss due to chemical cleaning and the maximum force shown here for comparison with values of specimens determined after corrosion presented in Table 5. The maximum force denotes the peak load recorded on the force-elongation curve and is used to calculate the ultimate tensile stress based on the specimen's initial cross-sectional area. To quantify the influence of corrosion, mass loss, maximum force after corrosion and depth are also shown in Table 5. Results indicated that with an increment in corrosion, mass, depth and maximum force significantly decreased. In Table 5, the change in depth $\Delta d_{\mathrm{mass}}$ based on mass loss is also shown, representing the difference between the depth before corrosion and after corrosion. Depth before corrosion and after corrosion based on mass loss are determined as follows:

$$d_0 = \frac{m_0}{A_{\mathrm{W}} D} \tag{2}$$

$$d_1 = \frac{m_1}{A_{\mathrm{W}} D} \tag{3}$$

where $m_0$ and $m_1$ are mass before and after expose to corrosion, respectively, $A_{\mathrm{W}}$ is the surface area of the specimen, and $D$ is the density.

*Table 4. Etalon specimens before and after chemically cleaning*

| Nominal thickness, mm (2 specimens) | $m_0$ / g | $d_0$ / mm | $m_1$ / g | $d_1$ / mm | $F_{\mathrm{max}}$ / N |
|---|---|---|---|---|---|
| 4 | 252.55±2.98 | 4.01±0.05 | 252.48±2.95 | 4.01±0.05 | 31624±755 |
| 6 | 386.74±1.22 | 6.14±0.02 | 386.70±1.22 | 6.14±0.02 | 50835±1261 |
| 8 | 517.28±5.92 | 8.21±0.09 | 517.25±5.93 | 8.21±0.09 | 62858±1044 |

Each values in the tables 3, 4 and 5 is expressed as the mean ± standard deviation calculated from two individual measurements. Preliminary results related to the 8 mm specimens were reported in previous publications [9]. This paper presents the comprehensive findings for all three specimens thicknesses.

*Table 5. Specimens before and after exposure to corrosion*

| Location | Nominal thickness, mm (2 specimens) | $d_0$ / mm | $d_1$ / mm | Mass loss, % | $\Delta d_{\mathrm{mass}}$ / mm | $F_{\mathrm{max}}$ / N |
|---|---|---|---|---|---|---|
| 1. Sulphuric acid plant, AF | 4 | 4.03±0.02 | 3.93±0.02 | 2.53±0.00 | 0.10±0.00 | 30146±205 |
| | 6 | 6.12±0.05 | 6.00±0.05 | 1.89±0.04 | 0.12±0.00 | 49152±1613 |
| | 8 | 8.26±0.02 | 8.14±0.03 | 1.47±0.03 | 0.12±0.00 | 61826±206 |
| 2. Electrolytic refining plant, EF | 4 | 4.03±0.01 | 4.02±0.01 | 0.32±0.00 | 0.01±0.00 | 31273±358 |
| | 6 | 6.11±0.01 | 6.10±0.01 | 0.25±0.00 | 0.02±0.00 | 50067±658 |
| | 8 | 8.14±0.20 | 8.12±0.20 | 0.19±0.03 | 0.02±0.00 | 62268±1253 |
| 3. The automatic air quality monitoring station in Mining and Metallurgy Institute Bor, MP | 4 | 4.05±0.03 | 4.02±0.03 | 0.79±0.01 | 0.03±0.00 | 30982±257 |
| | 6 | 6.11±0.01 | 6.07±0.01 | 0.60±0.01 | 0.04±0.00 | 51248±1519 |
| | 8 | 8.21±0.09 | 8.18±0.08 | 0.38±0.10 | 0.03±0.01 | 62715±832 |

After the coupon tests, the load and displacement results of the S235JR specimens exposed to different corrosion conditions were obtained. Figure 5 shows force-elongation curves of corroded and uncorroded test steel S235JR specimens of different nominal thickness. The main reason for the decrease in the maximum force is the effective reduction of the cross-sectional area of the corroded specimen. It is worth noting that the force decrease was greater in the case of a higher corrosion rate.

In the industrial atmosphere of Bor, near to AF, the colour of the rust from steel specimens is in dark brown tones; granulations of corrosion layers are larger, while on the specimens in the EF and MP granulation of corrosion layers is smaller, similar to ground powder. The dark brown colouring of the rust is the result of the presence of $SO_2$ at high concentrations and accelerating transformation of lepidocrocite into goethite [25]. In accordance with the statements of other authors [1], transformation of lepidocrocite to goethite is a measure of the corrosion process extension, so that this complies with the fact that lower corrosion is obtained at MP than near to AF in Bor. Corrosion products were definitely more compact and less porous when they are exposed to indoor conditions than outdoor conditions (they have a better protective function, which was also observed during the removal of corrosion products when measuring the mass loss). The compact corrosion products are the reason for lower mass loss (slower general corrosion) of these specimens. On the other hand, corrosion products formed outdoors exhibit layered deposits and cracks.

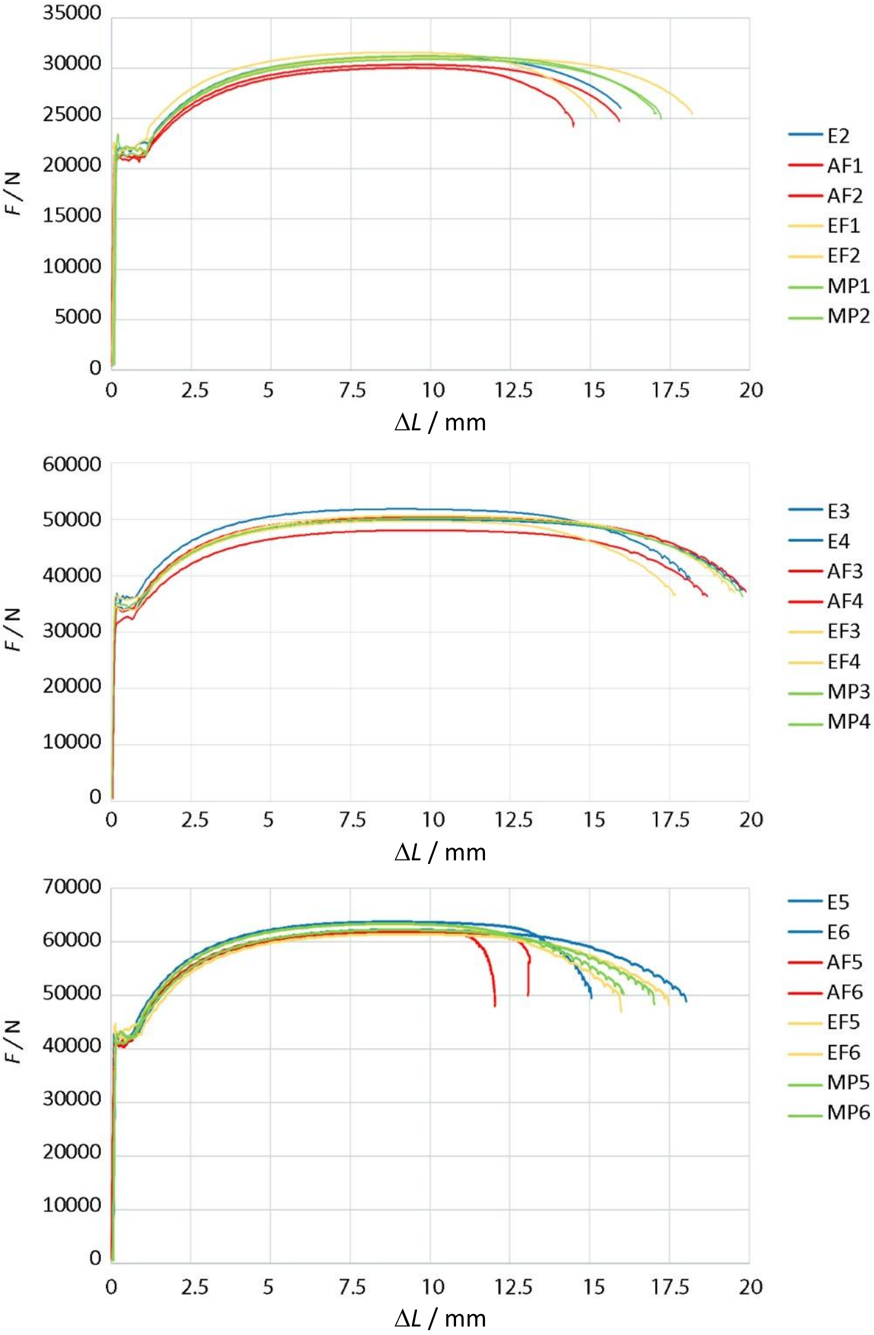

*Figure 5. Load-displacement relationships for etalon specimens (E) and tested specimens at AF, EF and MP for specimen thicknesses of: A) 4 mm (specimens are labeled with 1 and 2); B) 6 mm (specimens are labeled with 3 and 4); C) 8 mm (specimens are labeled with 5 and 6)*

Atmospheric corrosion is quantitatively assessed by measuring the mass loss and then determining the corrosion rate for each location separately. A higher corrosion rate is always obtained for specimens closer to the AF. Specimens that were exposed to corrosive agents from the outside, near the AF and next to MP, were uniformly corroded, while the dominant pitting corrosion can be observed in the specimens in EF. The highest corrosion rate values are generally associated with higher $SO_2$ levels in the air. For the corroded steel specimens, the reduction of maximum force is not linearly proportional to the degree of mass loss (Table 5). The cause of this finding is the appearance of pitting corrosion along with uniform corrosion, as well as the influence of local effects due to the inequalities on the specimens found after exposure to corrosion. Local pitting corrosion has a significant impact on strength reduction in addition to the section loss. It leads to fracture where the test specimens are weakest. The change in the path of fracture, with the development of corrosion, is also related to pitting corrosion.

In Figure 5, specimens from the same location are marked with the same colour. The force-elongation curves of the corroded specimens constantly decreased as the corrosion rate increased. Less corroded specimens (MP) have a larger "necking" area, while in more corroded specimens (AF), the "necking" area decreases together with the ductility of the elements. Specimens that suffered a greater mass loss (AF), become less ductile, due to local material damage that cannot be described by a uniform corrosion rate law and a uniform surface degradation. This statement is in agreement with the observations in a previous experiment [26] showing that in extreme corrosion cases, the yield plateau of the stress-strain curves of the corroded specimens shrinks and, in certain cases, completely vanishes, signifying a change in the steel elements, from ductile to brittle fracture.

## 4. CONCLUSION

Interaction between corrosion of steel elements and pollutants in the atmosphere is of great importance for corrosion research. The consequence of this interaction is degradation and destruction of steel structures. Corrosion of steel in an industrial environment can be uniform, developing equally over the entire surface of the metal which is characteristic of outdoor conditions, or localized, pitting corrosion (present in indoor conditions in the present study).

Uniform corrosion occurs through uniform corrosion layers of similar composition, while pitting corrosion creates types of corrosion products that differ in composition and proportions of their components, which is determined by XRD analysis in this paper. This primarily refers to the specimens that were in the indoor of the Electrolytic refining plant and for which the corrosion products were much more complex in composition than the products formed at the outdoor stations. It can be concluded that steel specimens exposed to indoor conditions experience less severe conditions, but also additional type of corrosion (pitting).

XRD analysis was used in this study as a relationship indicator between the composition of corrosion products and the type of environment in which corrosion develops. The results and data obtained in this work should contribute to the understanding of the problem of strength capacity and durability of steel structures weakened by corrosion in industrial environments such as in Bor.

***Acknowledgements**:* This work was financially supported by the Ministry of Science, Technological Development and Innovation of the Republic of Serbia, as well as the Contract on realization and financing of the scientific research work of the Mining and Metallurgy Institute Bor in 2024, contract number: 451-03-66/2024-03/200052 and also No. 200092, Faculty of Civil Engineering, University of Belgrade and 451-03-66/2024-03/200287, IC TMF. We are also kindly thankful to the Mining and Metallurgy Institute Bor for funding part of the laboratory work. The authors wish to thank Silvana Dimitrijević for help within the laboratory experiment and Zoran Avramović for field work.

## REFERENCES

[1] Mendoza A, Corvo F. Outdoor and indoor atmospheric corrosion of carbon steel. *Corros Sci*. 1999; 41: 75-86. https://doi.org/10.1016/S0010-938X(98)00081-X

[2] Gil H, Calderón J. A, Buitrago C. P, Echavarría A, Echeverría F. Indoor atmospheric corrosion of electronic materials in tropical-mountain environments. *Corros Sci.* 2010; 52(2): 327-337. https://doi.org/10.1016/j.corsci.2009.09.019

[3] Del Angel-Meraz E, Corvo F, Hernandez-Morales N, Tejero-Rivas M. Particularities of indoor atmospheric corrosion of steel inside electric boxes in the tropical climate of Tabasco, Mexico. *Indoor Built Environ.* 2020; 30(10): 1609-1619. https://doi.org/10.1177/1420326X20950411

[4] Rajaković-Ognjanović V, Grgur B. Corroded scale analysis from water distribution pipes. *Hem. Ind.* 2011; 65(5): 507-515. https://doi.org/10.2298/HEMIND110523049R

[5] Xue X, Hua J, Wang F, Wang N, Li S. Mechanical Property Model of Q620 High-Strength Steel with Corrosion Effects. *Buildings*. 2022; 12: 1651. https://doi.org/10.3390/buildings12101651

[6] Zhao N, Zhang C. Experimental Investigation of the Mechanical Behavior of Corroded Q345 and Q420 Structural Steels. *Buildings.* 2023; 13: 475. https://doi.org/10.3390/buildings13020475

[7] Di Sarno L, Majidian A, Karagiannakis G. The Effect of Atmospheric Corrosion on Steel Structures: A State-of-the-Art and Case-Study. *Buildings*. 2021; 11: 571. https://doi.org/10.3390/buildings11120571

[8] Li F, Cui C, Ma R, Tian H. An experimental study on the corrosion behaviors and mechanical properties of Q345qD steel in neutral salt spray environment considering stress state. *Dev Built Environ*. 2023; 15: 100214. https://doi.org/10.1016/j.dibe.2023.100214

[9] Stefanović J, Dimitrijević S, Filipović S, Đorđević J. Evaluation of the corrosion resistance of steel elements in the industrially aggressive environments using the accelerated corrosion testing methods. *Min Metall Eng Bor.* 2023; 1: 53-60. https://doi.org/10.5937/mmeb2104053S

[10] Sanders C, Santucci R. Jr. Experimental Design Considerations for Assessing Atmospheric Corrosion in a Marine Environment: Surrogate C1010 Steel. *Corros Mater Degrad*. 2023; 4(1): 1-17. https://doi.org/10.3390/cmd4010001

[11] Parekh SP, Pandya AV, Kadiya HK. Progressive Atmospheric Corrosion Study of Metals Like Mild Steel, Zinc and Aluminum in Urban Station of Ahmedabad District. *Int J Chemtech Res*. 2012; 4: 1700-1774. http://dx.doi.org/10.1155/2009/807376

[12] ISO Standard 8407:2021 Corrosion of Metals and Alloys: Corrosivity of atmospheres: Removal of Corrosion Products from Corrosion Test Specimens. https://www.iso.org/standard/71866.html

[13] PDXL, Version 2.0. 3.0 Integrated X-ray Powder Diffraction Software, Rigaku Corporation. Tokyo, Japan; https://rigaku-pdxl.software.informer.com/2.0/

[14] Annual and monthly reports on ambient air quality in Bor for the period 2016-2017 (Archive MMI Bor), Mining and Metallurgy Institute Bor (MMI Bor), Laboratory for Chemical Testing, Department for Environmental Protection and Climate Change, Bor, Serbia.

[15] Annual report on air quality in the Republic of Serbia in 2016, Republic of Serbia, Ministry of Environmental Protection, Environmental protection agency, Belgrade, Serbia. https://sepa.gov.rs/wp-content/uploads/2024/10/Vazduh2016.pdf. Accessed 2017.

[16] Annual report on air quality in the Republic of Serbia in 2017, Republic of Serbia, Ministry of Environmental Protection, Environmental protection agency, Belgrade, Serbia. https://sepa.gov.rs/wp-content/uploads/2024/10/Vazduh2017.pdf Accessed 2018.

[17] Seechurn Y, Surnam B, Wharton J. Marine atmospheric corrosion of carbon steel in the tropical microclimate of Port Louis. *Mater Cor.* 2022; 73: 1474-1489. https://doi.org/10.1002/maco.202112871

[18] Pan C, Han W, Wang Z, Wang C, Yu G. Evolution of Initial Atmospheric Corrosion of Carbon Steel in an Industrial Atmosphere. *JMEP*. 2016; 25: 5382-5390. https://doi.org/10.1007/s11665-016-2312-0

[19] Wu H, Luo Y, Zhou G. The Evolution of the Corrosion Mechanism of Structural Steel Exposed to the Urban Industrial Atmosphere for Seven Years. *Appl Sci.* 2023; 13: 4500. https://doi.org/10.3390/app13074500

[20] Qin H, Liu J, Shao Q, Zhang X, Teng Y, Chen S, Zhang D, Bao S. Corrosion behavior and cellular automata simulation of carbon steel in salt-spray environment. *Mater Degrad.* 2024; 8: 29. https://doi.org/10.1038/s41529-024-00447-9

[21] De la Fuente D, Díaz I, Simancas J, Chico B, Morcillo M. Long-term atmospheric corrosion of mild steel. *Cor Sci*. 2011; 53: 604-617. https://doi.org/10.1016/j.corsci.2010.10.007

[22] Dhaiveegan P, Elangovan N, Nishimura T, Rajendran N. Weathering Steel in Industrial-Marine-Urban Environment: Field Study. *MaterTrans.* 2016; 57, (2): 148-155. https://doi.org/10.2320/matertrans.M2015345

[23] ISO Standard 9223:2012 Corrosion of metals and alloys — Corrosivity of atmospheres — Classification, determination and estimation. https://www.iso.org/standard/53499.html

[24] ISO Standard 9226:2012 Corrosion of metals and alloys—Corrosivity of atmospheres—Determination of corrosion rate of standard specimens for the evaluation of corrosivity. https://www.iso.org/standard/53502.html

[25] Montoya P, Díaz I, Granizo N, de la Fuente D, Morcillo M. An study on accelerated corrosion testing of weathering steel. *Mater. Chem. Phys*. 2013; 142: 220-228. https://doi.org/10.1016/j.matchemphys.2013.07.009

[26] Zhang Z, Xu Y, Qin G, Xu S, Li R. Deterioration of Mechanical Properties and the Damage Constitutive Model of Corroded Steel in an Industrial Environment. *Materials*. 2022; 15: 8841. https://doi.org/10.3390/ma15248841

# Eksperimentalna analiza atmosferske korozije čelika S235JR u industrijskoj sredini

**Jelena N. Stefanović[1], Zoran Mišković[2], Stevan Dimitrijević[3], Zlatko Marković[2] i Milan Spremić[2]**

[1]*Institut za rudarstvo i metalurgiju Bor, Bor, Srbija*
[2]*Univerzitet u Beogradu, Građevinski fakultet, Beograd, Srbija*
[3]*Inovacioni centar Tehnološko-metalurškog fakulteta, Beograd, Srbija*

(Naučni rad)

*Izvod*

U ovom radu ispitana je atmosferska korozija konstrukcionog čelika S235JR u industrijskoj sredini. Opšta ispitivanja korozije vršena su u blizini fabrike sumporne kiseline, u postrojenju za elektrolitičku rafinaciju i pored automatske stanice za praćenje kvaliteta vazduha u Boru u periodu od 6 meseci. Za ispitivanje međusobnog dejstva korozije i zagađenja industrijske sredine, korišćen je čelik S235JR, a njegove mehaničke karakteristike su dobijene ispitivanjem zatezanjem. Određeni su i meteorološki parametri, kao i zagađujuće materije u atmosferi (uglavnom $SO_2$). Rendgenska difrakciona analiza (engl. X-ray diffraction, XRD) je korišćena za identifikaciju mineorološkog sastava produkata korozije. XRD analiza može ukazati na vezu između gubitka nosivosti i vrste sredine u kojoj se korozija razvija. Na osnovu dobijenih rezultata vrši se dalje predviđanje degradacije materijala usled korozije u industrijski agresivnoj sredini. Istraživanja u okviru ovog rada su omogućila bolje razumevanje ponašanja konstrukcionog čelika S235JR u kom je došlo do redukcije nosivosti usled korozije. Utvrđeno je da su produkti korozije različita jedinjenja u zavisnosti od sadržaja zagađujućih materija u atmosferi i lokacije čeličnih elemenata.

*Ključne reči:* Ispitivanje korozije; atmosferske korozione stanice; produkti korozije; $SO_2$; XRD analiza; ispitivanje zatezanjem

# Numerical investigation of free convection within a circular cavity with a flexible fin

**Atika Bencherif[1], Mohamed Bouzit[1], Abderrahim Mokhefi[2], Hanaa Derraz[1] and Fatima Zohra Khelif[1]**

*[1]Laboratory of Maritime Sciences and Engineering LSIM Faculty of Mechanical Engineering, University of Science and Technology of Oran Mohamed Boudiaf, Oran, Algeria*

*[2]Mechanics, Modeling and Experimentation Laboratory L2ME, Faculty of Sciences and Technology, Bechar University, Bechar, Algeria*

ORIGINAL SCIENTIFIC PAPER

**UDC: 551.509.313:631.436.1**

*Hem. Ind.* **79(1)** 31-46 (2025)

*Abstract*

The problem of unsteady natural convection inside a circular cavity containing a flexible fin is numerically studied in this work. The cavity's left side is hot, while the right side is cold. A flexible elastic fin is attached to the center of the hot wall. The fluid-structure interaction in the cavity and flexible fin is combined with Newtonian fluid. The governing equations of the fluid-flexible fin interaction are solved using the Finite Elements method and the arbitrary Lagrangian-Eulerian approach. The effects of an elastic flexible fin on natural convection within circular cavities were investigated in this study. The Rayleigh number ($10^3 \leq Ra \leq 10^5$) and Elasticity modulus ($10^{10} \leq Et \leq 10^{11}$) are the parameters studied, the average Nusselt numbers well as isotherms and streamlines, are investigated. The results show that increasing the Rayleigh number causes an increase in the average Nusselt number, which becomes significant for a higher Rayleigh number. Therefore, it is discovered that the circular shape of the cavity may improve the heat transfer rate.

*Keywords:* Newtonian fluid; fluid-structure interaction; finite elements method; elasticity modulus; average Nusselt number; Rayleigh number.

*Available on-line at the Journal web address: http://www.ache.org.rs/HI/*

## 1. INTRODUCTION

Heat transfer by natural convection in obstructed cavities is of both fundamental and industrial importance, finding applications in various fields including electronic equipment cooling, solar collector manufacturing, housing thermal management, and nuclear engineering. In recent years, extensive experimental and numerical research has been dedicated to understanding heat transfer in cavities equipped with fins.

Considering natural convection, many published works have investigated the problem of unsteady fluid-structure interaction inside various cavities, such as square cavities [1-3], circular enclosures [4], and L-shaped enclosures [5]. Additionally, several studies have explored mixed convection across different enclosures, including those with multiple openings [6], channel configurations [7], and flexible walls [8].

Further research has aimed to better comprehend this phenomenon by considering different fluids, including Newtonians, non-Newtonians, and nanofluids. For instance, many studies on Newtonian fluid natural convection have examined the effects of oscillating flexible fins [9-11] indicating an increase in the fluid flow rate amplitude with increasing fin-free end amplitude. Additionally, the heat transfer rate in the case of using of flexible fins has shown a higher Nusselt number compared to that determined when using rigid fins. Raisi *et al*. [12] presented the effect of fluid-solid interaction on transient natural convection inside a square cavity and discovered that the impact of increasing baffle length on the thermal performance of the cavity varies based on the Rayleigh number and the rigidity or flexibility of the system. Heat transfer properties in cavities with porous mediums have been also studied [13-16]. The findings

---

Corresponding author: Atika Bencherif, Laboratory of Maritime Sciences and Engineering LSIM Faculty of Mechanical Engineering, University of Science and Technology of Oran, Mohamed Boudiaf, Algeria

E-mail: atika.bencherif@univ-usto.dz

Paper received: 29 October 2023; Paper accepted: 4 February 2025; Paper published: 17 April 2025.

https://doi.org/10.2298/HEMIND231029001B

indicate that an oscillation amplitude of 0.1 significantly improves the heat transfer rate across all Rayleigh numbers, and the average Nusselt number is typically greater for Darcy models than for Darcy-Forchheimer models. A study of natural convection heat transfer in buoyancy-induced flow scenarios within a square cavity [17] has shown that in the scenario of a plate fixed at its top, the highest stress is observed with an inclination angle of 40°. In a recent study, natural convection around square cylinders and within enclosures containing heated circular cylinders has provided insights into optimal heat transfer conditions [18]. It was observed that the 45° angle of the rotation square cylinder provides the optimal and the most efficient heat transfer at a higher Rayleigh number. Investigation of unsteady natural convection heat transfer within an enclosure with a heated circular cylinder [19,20] has indicated that the enclosure performance rate is the highest when the membrane is placed at 45°, while the increase in the Prandtl number (from 0.1 to 0.2) leads to the decrease in the Nusselt number, even though the Rayleigh number is increasing. Furthermore, numerical methods such as the smoothed particle element method (SPEM) have been proposed to effectively model fluid-structure interactions in free surface problems [21]. Heat transfer enhancement in a vented cavity using an externally oscillating flexible flow modulator has been demonstrated [22], showing the increase in heat transfer as the oscillation period of the flexible modulator decreases. A numerical approach utilizing the sharp-interface CURVIB solver (curvilinear immersed boundary solver) has been employed to simulate fluid-structure interaction (FSI) problems in complex domains involving thin, flexible solid structures [23].

Investigations of natural convection of a non-Newtonian power-law fluid with utilization a flexible fin [24-26], indicated that the fin predominantly deforms in dilating non-Newtonian fluids, while rigid fins are experiencing higher maximal stresses as compared to flexible fins. Additionally, a significant decrease in the average Nusselt number is observed when the plate length is reduced. In other studies, laminar natural heat transfer was investigated for non-Newtonian power-law fluids within different enclosure geometries such as a square enclosure [27,28], rectangular enclosure [29,30], and an enclosure with a heated hexagonal block [31] as it was summarized in [37]. The compressible B-spline material point method (Weakly Compressible BSMPM) was provided and extended to resolve the complicated free surface flow of a non-Newtonian fluid following a power law rheology model [32]. Pandey *et al*. [33] examined thermal and flow characteristics of non-Newtonian fluids at Ra = $10^7$ in a circular cylinder within a square cavity. They concluded that heat transfer significantly increased for cases of a pseudoplastic fluid ($n$ <1) compared to cases of a dilatant fluid ($n$> 1). Numerical simulation of convective heat transfer and flow in a non-Newtonian power-law fluid was performed using the lattice Boltzmann method [34] showing that as the flow behavior index increases for a given Rayleigh number, the average Nusselt number at the hot wall and the rate of melting decrease. Jain *et al.* [35] investigated the heat transfer and flow characteristics of natural convection from a hot cylinder body in a square enclosure, and the results showed ~11% increase in heat transfer for an arc radius approaching 0 mm. The investigation of natural convection in a non-Newtonian fluid within a cavity is conducted over time, focusing on controlling parameters such as Rayleigh number, power-law index, and side oscillation frequency [36]. The smoothed particle hydrodynamics (SPH) method was used to simulate natural convection in a differentially heated square cavity at high Rayleigh numbers when the chaotic motion has a significant influence on the heat transfer characteristic [38].

In summary, research has addressed natural convection within various enclosure geometries using advanced numerical methods, shedding light on fundamental heat transfer phenomena. The purpose of this study is to investigate the effects of an elastic flexible fin on natural convection in a Newtonian fluid within a circular cavity, considering fluid-structure interactions.

## 2. MODELING APPROACH

Geometry considered in the current study is a circular cavity with a flexible fin attached to the central part of the hot left wall, as shown in Figure 1. The right wall is maintained cold at a temperature $T_c$*, while the left wall is brought to a higher temperature $T_h$*. The fluid circulating in the cavity is considered Newtonian and incompressible, while the flow is laminar and two-dimensional.

Based on these assumptions and the arbitrary Lagrangian-Eulerian (ALE) approach, the equations representing the hydrodynamic and thermal features of the problem are stated as follows, Equations. (1) to (7).

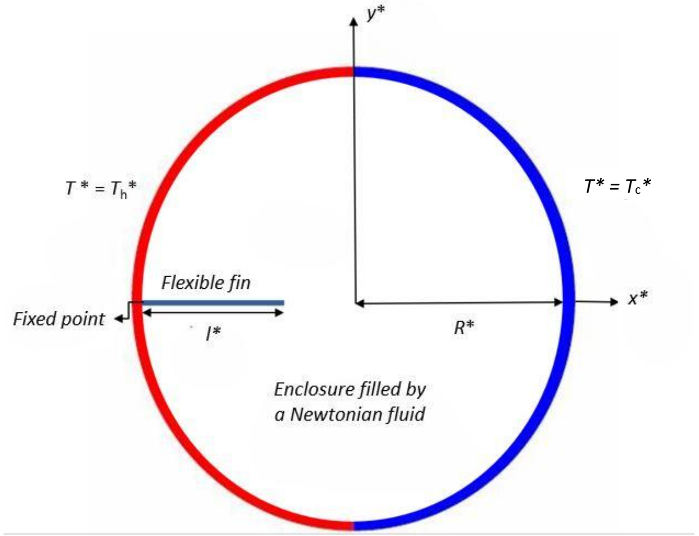

*Figure 1. Physical model of convection in a cavity with a flexible fin and coordinate system where T* represents the dimensional temperature field, (x*, y*) shows the dimensional Cartesian coordinate system, R* and l* represent the dimensional characteristic size of the cavity and the length of the flexible fin, respectively*

Continuity equation:

$$\nabla * \mathbf{u}* = 0 \tag{1}$$

Momentum equations:

$$\rho_{\mathrm{f}}\left[\frac{\partial \mathbf{u}*}{\partial t}+\left(\mathbf{u}*-\mathbf{w}*\right)\nabla*\mathbf{u}*\right]-\nabla*\left[-P*I+\mu\left(\nabla*\mathbf{u}*+\left(\nabla*\mathbf{u}*\right)^{tr}\right)\right]-\rho_{\mathrm{f}}\beta\mathbf{g}\left(T*-T_{\mathrm{c}}*\right)=0 \tag{2}$$

The energy equation for the fluid:

$$\left(\rho c_{\mathrm{p}}\right)_{\mathrm{f}}\left[\frac{\partial T*}{\partial t}+\left(\mathbf{u}*-\mathbf{w}*\right)\nabla*T*\right]-k_{\mathrm{f}}\nabla*^{2}T*=0\cdot \tag{3}$$

For the elastic structure domain, the energy equation for the fin can be written as:

$$\left(\rho c_{\mathrm{p}}\right)_{f}\frac{\partial T*}{\partial t}-k_{\mathrm{s}}\nabla*^{2}T*=0\cdot \tag{4}$$

where **u*** represents the velocity vector, **w*** shows the moving mesh velocity vector, and *P* represents the pressure field, *I* represent the identity tensor, *tr* is the transpose of a matrix, **g** is the gravity vector, $\alpha$ and $\beta$ represent the thermal diffusivity and volumetric thermal expansion respectively, $\rho$ is the density, $c_p$ is the specific heat at constant pressure, $k_f$ and $k_s$ signify the thermal conductivity of the fluid and the solid, respectively.

The Neo-Hookean solid model is applied to express the stress tensor $\sigma$*:

$$\sigma*=J^{-1}FSF^{tr}\,\Big|\,F=(I+\nabla*\mathbf{d}_{\mathrm{s}}*),\ J=\det(F)\ \text{and}\ S=\partial W_{\mathrm{s}}/\partial\varepsilon\cdot \tag{5}$$

$$W_{\mathrm{s}}=\frac{1}{2}l(J^{-1}I_{1}-3)-l\ln J+\frac{1}{2}\lambda(\ln J)^{2}\,\left|\,\begin{array}{c} l=E/(2(1+\nu)) \\ \lambda=E\nu/((1+\nu)(1-2\nu)) \end{array}\right. . \tag{6}$$

$$\varepsilon=\frac{1}{2}\left(\nabla*\mathbf{d}_{\mathrm{s}}*+\nabla*\mathbf{d}_{\mathrm{s}}*^{\mathrm{tr}}+\nabla*_{\mathrm{s}}*^{\mathrm{tr}}\nabla*\mathbf{d}_{\mathrm{s}}*\right)\cdot \tag{7}$$

where *F* is the deformation gradient tensor, $F^{tr}$ is the transpose of the deformation gradient tensor, $d_s$*****represents the solid displacement vector, *S* the second Piola-Kirchhoff, $W_s$ is the strain energy density function, $I_1$ represents the first invariant of the right Cauchy–Green deformation tensor, *E* the young's modulus of the solid, *v* the poisson's ratio of the solid, *ε* is the strain.

Boundary conditions applicable to the external walls Eqs. (8) and (9), and the flexible fin interface Eq. (10) are expressed as:

At the hot wall:

$$T^* = T_h^*,\ \mathbf{u}^* = v^* = 0 \tag{8}$$

At the cold wall

$$T^* = T_c^*,\ \mathbf{u}^* = v^* = 0 \tag{9}$$

At the interface of the flexible fin:

$$k_f \left.\frac{\partial y}{\partial x}\right|_f = k_s \left.\frac{\partial y}{\partial x}\right|_s \cdot \tag{10}$$

This equation ensures that the heat flux leaving the fin is equal to the heat flux entering the substrate, where *y* typically represents temperature, which is a function of the position (*x*) in this case.

Also, the Rayleigh and Prandtl numbers (Ra and Pr, respectively) and the elasticity modulus ($E_\tau$) are introduced as:

$$\mathrm{Ra} = \frac{\rho_0^{\ 2} c_p \mathbf{g} \beta \Delta T 2R^3}{\mu_B k} \cdot \tag{11}$$

$$\mathrm{Pr} = \frac{c_p \mu_B}{k} \cdot \tag{12}$$

$$E_\tau = \frac{E 2R^{*2}}{\rho_f \alpha_f^{\ 2}} \cdot \tag{13}$$

To quantify the heat transfer between the flexible fin and the fluid, we used the Nusselt number as follows in the Eqs. (14) and (15):

$$\mathrm{Nu}_f = -\frac{\partial \theta}{\partial X} \cdot \tag{14}$$

$$\mathrm{Nu}_s = -k_r \frac{\partial \theta}{\partial X}. \tag{15}$$

$\mathrm{Nu}_f$ quantifies the heat transfer rate at the interface between the flexible fin and the surrounding fluid, and the $\mathrm{Nu}_s$ describes the heat transfer within the fin material. $\theta$ represents the dimensionless temperature, *X* is a dimensionless spatial coordinate along the fin, and $k_r$ represents the thermal conductivity ratio.

The average Nusselt number on the wall is presented as follows:

$$\overline{\mathrm{Nu}} = \int_0^{s_1} \mathrm{Nu}_f \mathrm{d}y + \int_{s_1}^{s_2} \mathrm{Nu}_s \mathrm{d}y + \int_{s_2}^{1} \mathrm{Nu}_f \mathrm{d}y \left. \vphantom{\int_0^1} \right|_{\substack{s_1 = \frac{1}{2} - \frac{t_{fin}}{2} \\ s_2 = \frac{1}{2} + \frac{t_{fin}}{2}}} \cdot \tag{16}$$

where $s_1$ and $s_2$ represent the positions along the wall based on the thickness of the fin.

## 3. NUMERICAL METHOD, GRID STUDY AND VALIDATION

### 3. 1. Numerical approach and mesh independency

The governing equations and boundary conditions are transformed into weak form before being numerically solved in the moving grid system using the finite element method. An Arbitrary Lagrangian-Eulerian (ALE) method for fluid-flexible fin interaction is utilized. The computational domain is discretized into triangular non-uniform elements as shown in Figure 2. To simplify the nonlinear terms in the momentum equations, a Newton iteration algorithm is used. Physical and thermal properties of the fin and fluid adopted for simulations are shown in Table 1.

The equations are solved using the finite element method. The process starts by defining physics, PDEs, and boundary conditions, followed by mesh generation and discretization. The system is then assembled into a global matrix (*Ax* = *b*) and solved using iterative solvers.

In numerical methods for solving physical problems, grid-independence tests are achieved to confirm that the results are independent of the number of mesh elements. Table 2 examines the average Nusselt number ($\mathrm{Nu}_{avg}$) on the hot wall at Ra = $10^5$, Et = $10^{10}$, and Pr = 10 for five different mesh sizes. Table 2 shows the number of elements used in the fluid domain and the Nusselt number for various mesh sizes at a steady state. As a result, it can be determined that the grid with 245180 elements (case 4) is appropriate for use in all the computations in this paper.

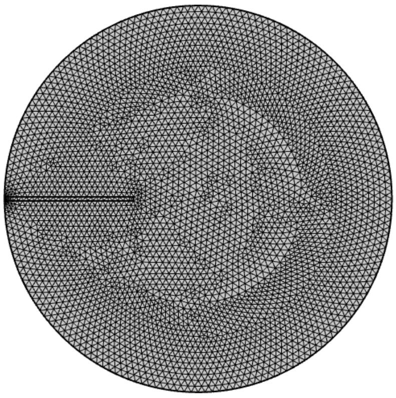

*Figure 2. The schematic presentation of the utilized grid*

*Table 1. Physical and thermal properties of materials*

| Material | Physical properties | Thermal properties | Dimensionless parameters |
|---|---|---|---|
| Fluid | $\rho_f$ = 1000 kg m$^{-3}$<br>$\mu_f$ = 1.457 Pa s | $\alpha$ = 0.14627 mm$^2$ s$^{-1}$<br>$k_f$ = 0.609 W m$^{-1}$ K$^{-1}$<br>$C_p$ = 4179 J kg$^{-1}$ K$^{-1}$<br>$\beta$ = 1.2E-7 K$^{-1}$ | Pr =10<br>Fv = 0<br>$k_r$ = 100<br>$\rho_r$ = 1 |
| Fin | $\rho_s$ = 1500 kg m$^{-3}$<br>$t_{fin}$ = 0.226 mm | $k_s$ = 1000 W m$^{-1}$ K$^{-1}$<br>$C_p$ = 100 J kg$^{-1}$ K$^{-1}$ | |

*Table 2. The average Nusselt number at the steady state solution for different grids when Et = $10^{10}$, Ra = $10^5$ and Pr = 10*

| Grid | Number of elements | Time, s | $Nu_{avg}$ |
|---|---|---|---|
| Case (1) | 63154 | 2012 | 7.96685 |
| Case (2) | 110656 | 3910 | 8.07652 |
| Case (3) | 171800 | 5846 | 8.16314 |
| Case (4) | 245180 | 8573 | 8.22831 |
| Case (5) | 332260 | 11679 | 8.22837 |

### 3. 2. Validation with others results

Another critical step in the simulation to ensure the accuracy and correctness of the obtained results is the validation through other studies. This work is validated on the basis of a study reported in literature [24]. In the literature [24], the study focused on the flow and heat transfer of a power-law non-Newtonian fluid within a cavity, driven by buoyancy forces. The interaction between the non-Newtonian flow in the cavity and the hot fin was modeled through Fluid-Structure Interaction (FSI), where the flow caused the fin to deform, which subsequently influenced both the flow and heat transfer. This two-way coupling was simulated using the Arbitrary Lagrangian-Eulerian (ALE) method with a moving mesh, while the governing equations were solved by using the finite element method.

First, the findings of this investigation are compared to the contours of isotherms obtained in that study [24] when Pr = 10 and Et = $10^{10}$ have been used for the validation of this study. As shown in Figure 3, the present numerical results are in thorough agreement with the literature results [24].

Second, streamlines reported in literature [24] when Pr = 10 and Et = $10^{10}$ are compared for different Rayleigh numbers (Ra) with those obtained by the present method (Fig. 4), showing satisfactory agreement.

Finally, for validation of the natural convection mechanism of a Newtonian fluid within a cavity, numerical modeling in the reference [24] has been re-simulated by the code employed in the present study. The evaluation of the Nusselt number for different values of the Rayleigh number (Ra) is represented in Table 3, showing satisfactory agreements of the results.

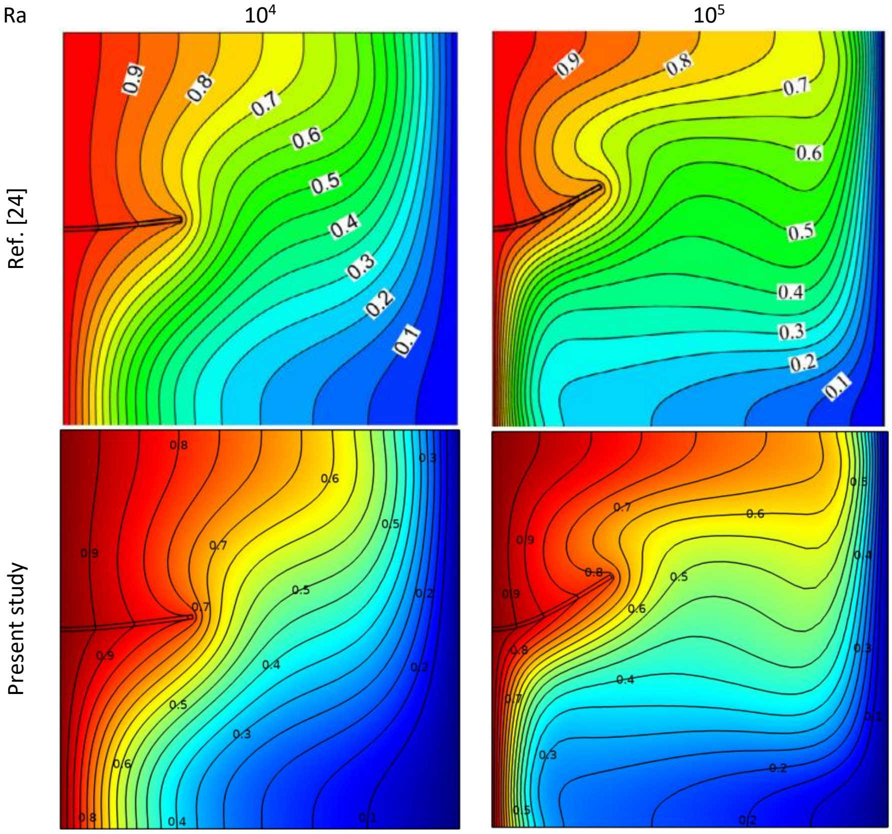

*Figure 3. Comparing the results of the present study and the contours of isotherms reported by in literature [24] when Pr = 10 and Et = $10^{10}$*

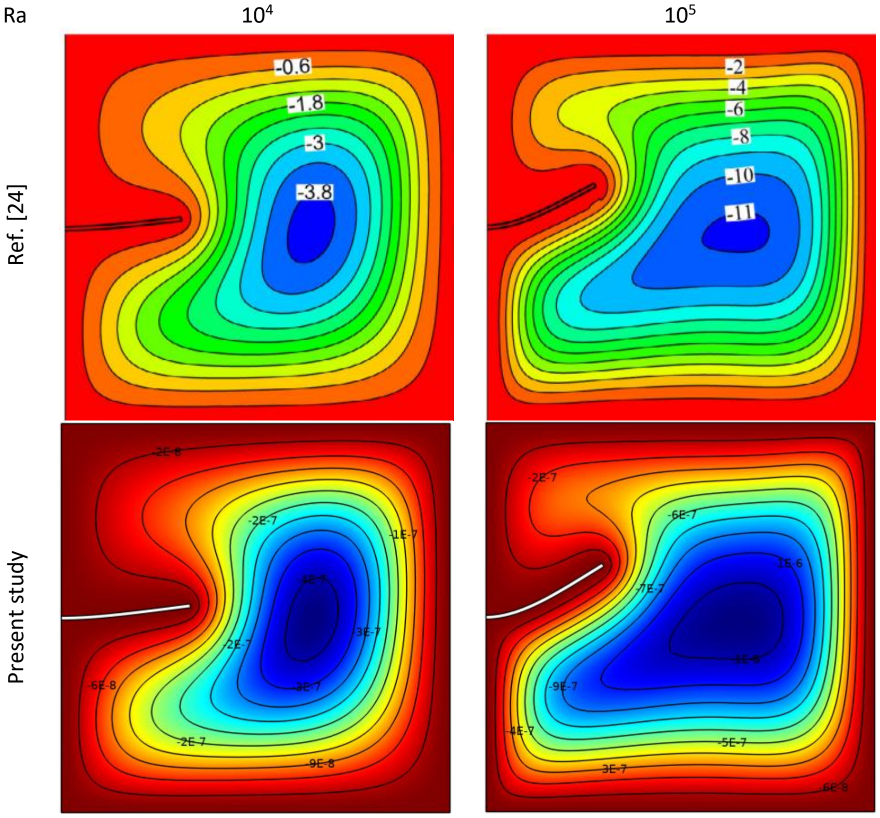

*Figure 4. Comparison of the results obtained in the present study and the streamlines reported in literature [24] when Pr = 10 and Et = $10^{10}$*

*Table 3. The average Nusselt (Nu) for different values of the Rayleigh number at Pr =10*

| Ra | $Nu_{avg}$ | | Error, % |
|---|---|---|---|
| | Shahabadi *et al.* [24] | Present study | |
| $10^3$ | 1.11883 | 1.12423 | 0.480 |
| $10^4$ | 1.92385 | 1.92536 | 0.784 |
| $10^5$ | 4.41245 | 4.41632 | 0.387 |

## 4. RESULTS AND DISCUSSION

This study examines the impact of various factors on thermo-flow fields and deformation of an elastic fin. The factors under investigation include the Rayleigh number ($10^3 \le Ra \le 10^5$), and the elasticity modulus ($10^{10} \le Et \le 10^{11}$). This research aims to inform readers about the consequences of different parameters on the behavior of the fin.

Figure 5 illustrates the changes in isotherms over time in a scenario with Ra = $10^5$, Pr = 10, and Et = $10^{10}$.

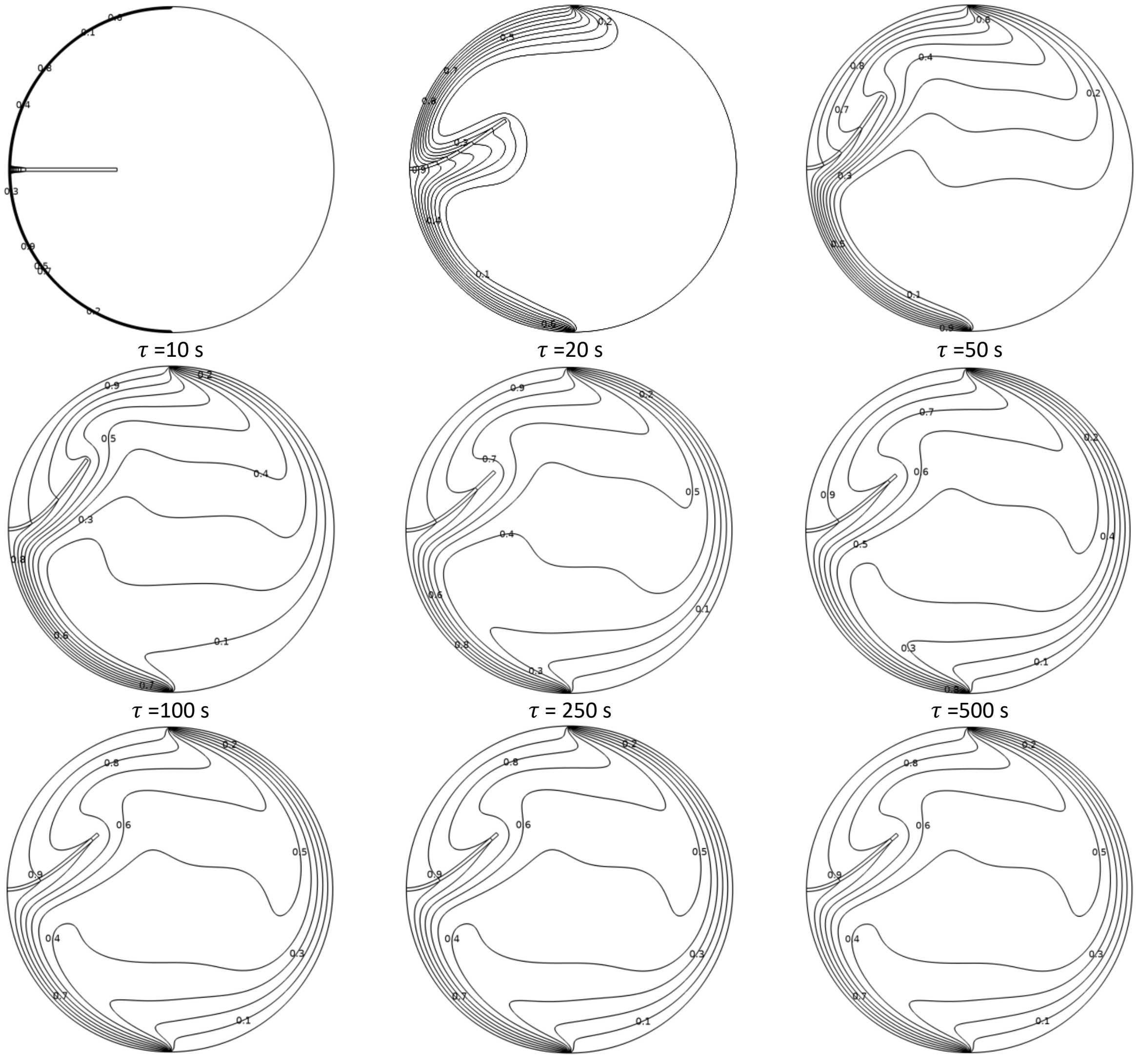

$\tau$ =10 s $\tau$ =20 s $\tau$ =50 s

$\tau$ =100 s $\tau$ = 250 s $\tau$ =500 s

$\tau$ =700 s $\tau$ =900 s $\tau$ =1000 s

*Figure 5. Development of isotherms and deformation of the flexible fin overtime ($\tau$) for Ra = $10^5$, Pr = 10, and Et = $10^{10}$*

Initially, at overtime $\tau$ = 10 s, the flexible heat-conducting fin remains stationary due to the dominance of conduction in heat transfer. As time progresses to $\tau$ = 20 s, there is a noticeable flow of fluid and heat transfer, causing the flexible fin to move towards the hot wall. Between 50 s < $\tau$ < 250 s, more vortices appear around the fin, leading to a shift in the isotherms towards the fin. Consequently, the role of convection becomes more significant compared to conduction in the heat transfer mechanism. Finally, in the steady state at $\tau$ = 1000 s, the fin movement aligns with the flow direction, leading to rotational flows in the upper left wall. This convection cell exhibits the highest circulation intensity among all-time instances. It can also be observed that the flexible fin reaches its highest level of displacement during this period.

Figure 6 shows an evolution of the streamlines with time at Ra = $10^5$, Pr =10 and Et = $10^{10}$. According to this figure, two weak vortices are seen at the initial time above and under the fin on the hot wall due to the negligible convective heat transfer. As time passes, we can see one vortex under the fin close to the left wall. In the time period 500 s <$\tau$< 1000 s, there are two weak vortices: one vortex is next to the cold wall, and another is on the hot wall.

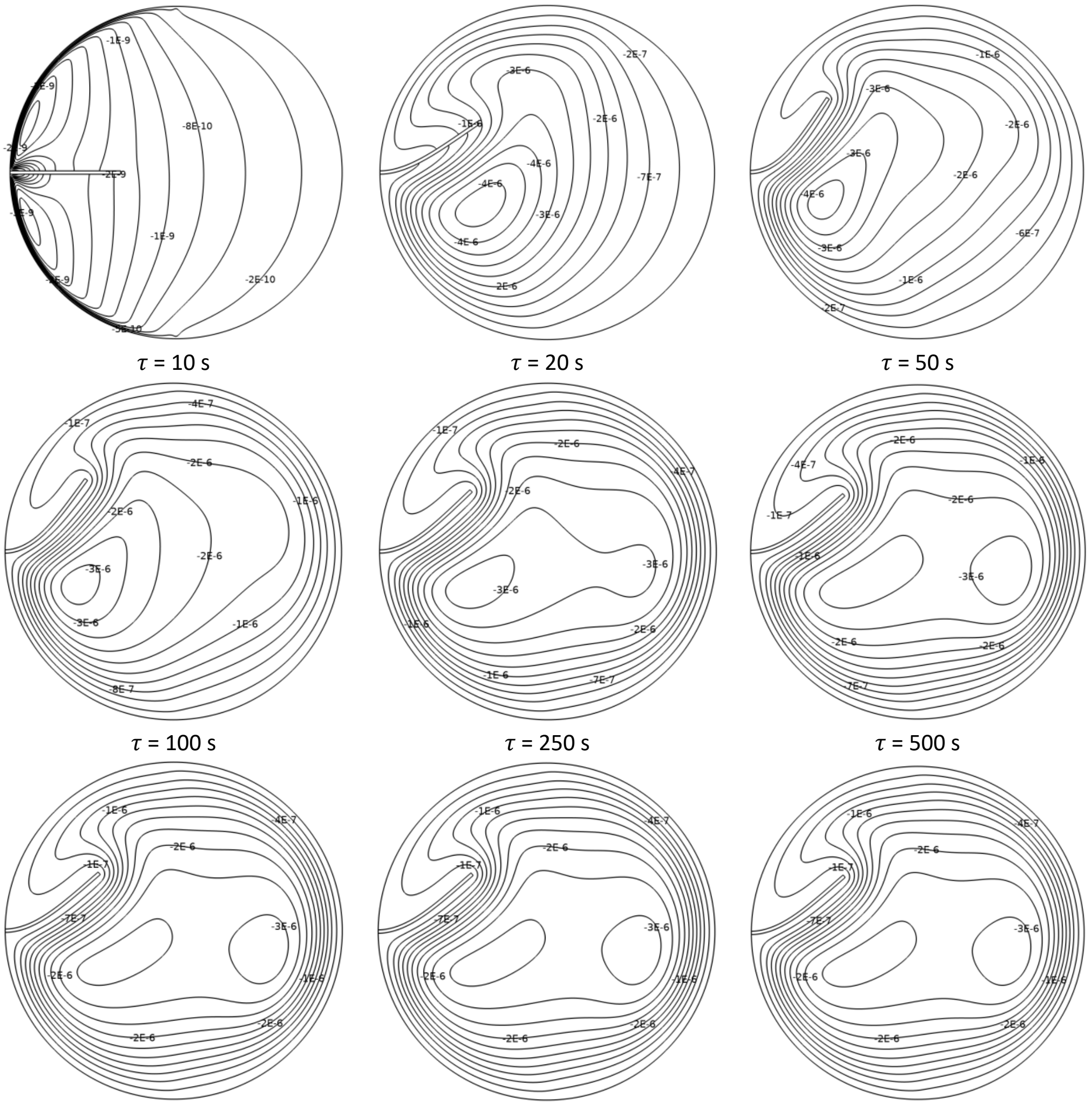

$\tau$ = 10 s $\tau$ = 20 s $\tau$ = 50 s

$\tau$ = 100 s $\tau$ = 250 s $\tau$ = 500 s

$\tau$ = 700 s $\tau$ = 900 s $\tau$ = 1000 s

*Figure 6. Development of streamlines and deformation of the flexible fin overtime for Ra = $10^5$, Pr = 10 and Et = $10^{10}$*

Figure 7 displays the effects of elasticity modulus (Et) and different values of the Rayleigh number (Ra) on the isotherms at the steady state at Pr = 10. According to the figure, at the lower Rayleigh number (Ra = $10^3$), the elastic fin is not moving. Meanwhile, the isotherms are parallel to the cold and hot vertical walls of the cavity, indicating that conduction is the main mechanism of heat transfer. In the case of increasing the Rayleigh number *i.e*. Ra = $10^4$, motion of the fin is solely affected, and natural convection becomes more intense. In addition, the increase in the Rayleigh number indicates that the isotherms are deviating from the vertical state, and the buoyant-driven flow is beginning to dominate the heat transfer mechanism. At the higher Rayleigh number of Ra = $10^5$, natural convection is the main heat transfer mechanism. It is interesting to note that the motion of the fin mostly affects the upper left hot wall for a lower elasticity modulus of Et = $10^{10}$. The reason for this behavior could be the increase in the convective flow.

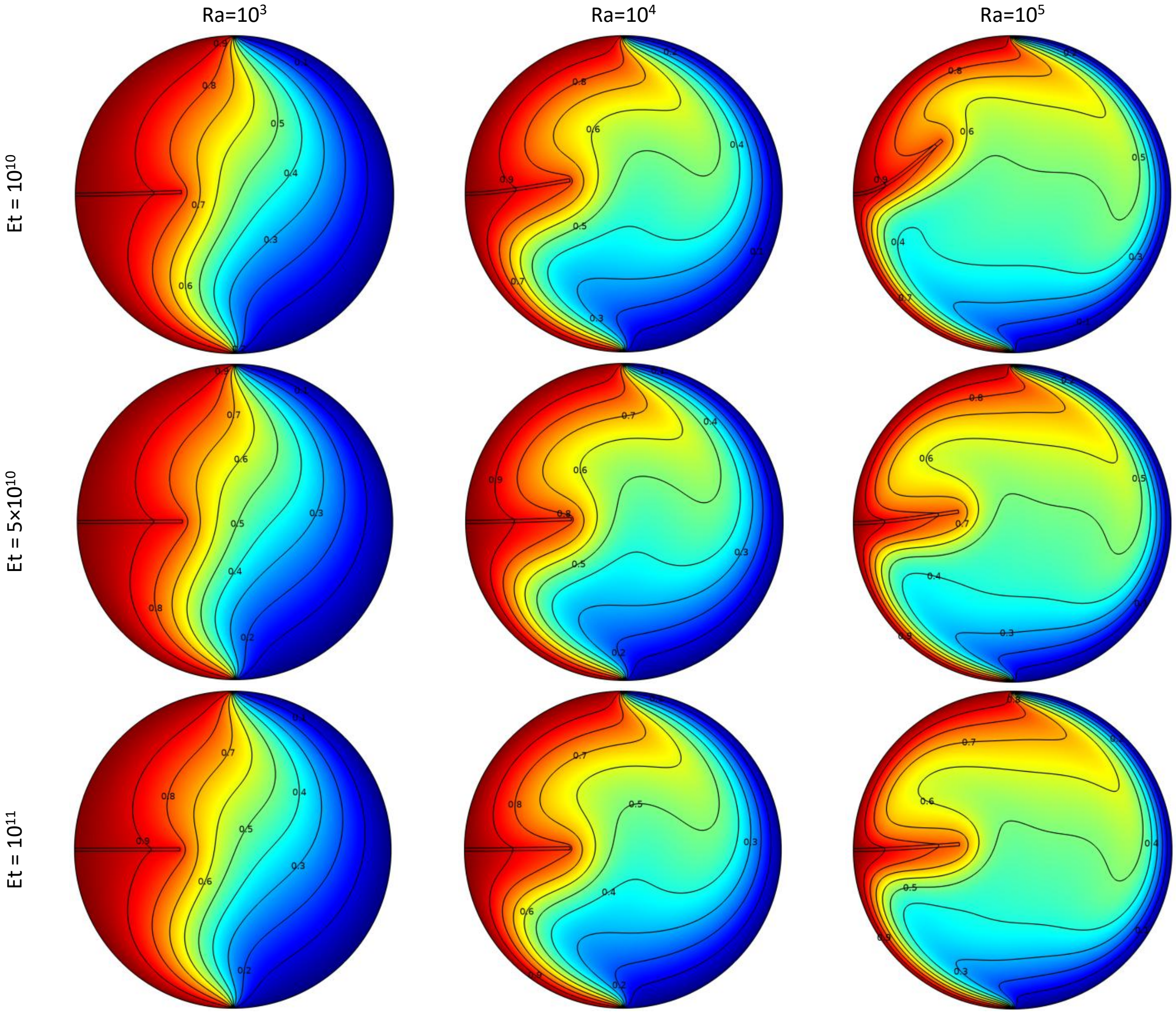

*Figure 7. Isotherm contours for various Rayleigh numbers (Ra) and different values of elasticity modulus (Et) at Pr = 10*

The results of the isothermal and steady-state streamlines at Pr = 10 and for various values of the Rayleigh number and elasticity modulus are shown in Figure 8. According to the figure, at a lower Rayleigh number (Ra = $10^3$), the streamlines are symmetrical relative to the vertical centerline and the streamline pattern indicates that conduction is the main mechanism of heat transfer. At a Rayleigh number of Ra = $10^4$, the streamlines become asymmetric regarding the vertical centerline, and a lateral vortex formed on the sides of the ribs moves to the right side of the cavity. Further, a double-eye circulation for a lower elasticity modulus (Et = $10^{10}$) is depicted for a higher Rayleigh number of Ra = $10^5$. The two vortices are central, and there is one vortex under the flexible fin close to the hot wall and another one next to the cold wall of the cavity. It is worth mentioning that vortices are less pronounced near the left upper portion of the fin, which rotates in counterclockwise direction, compared to other regions of the fin where vortices are more prominent.

Figure 9 shows the average Nusselt number overtime for different Rayleigh numbers at Et=$10^{10}$ and Pr = 10. The average Nusselt number was the highest for Ra = $10^5$ as compared to those determined for the other two Rayleigh numbers (*i.e.* $10^4$ and $10^3$). It is interesting to note that the average Nusselt number increases as the Rayleigh number is increased.

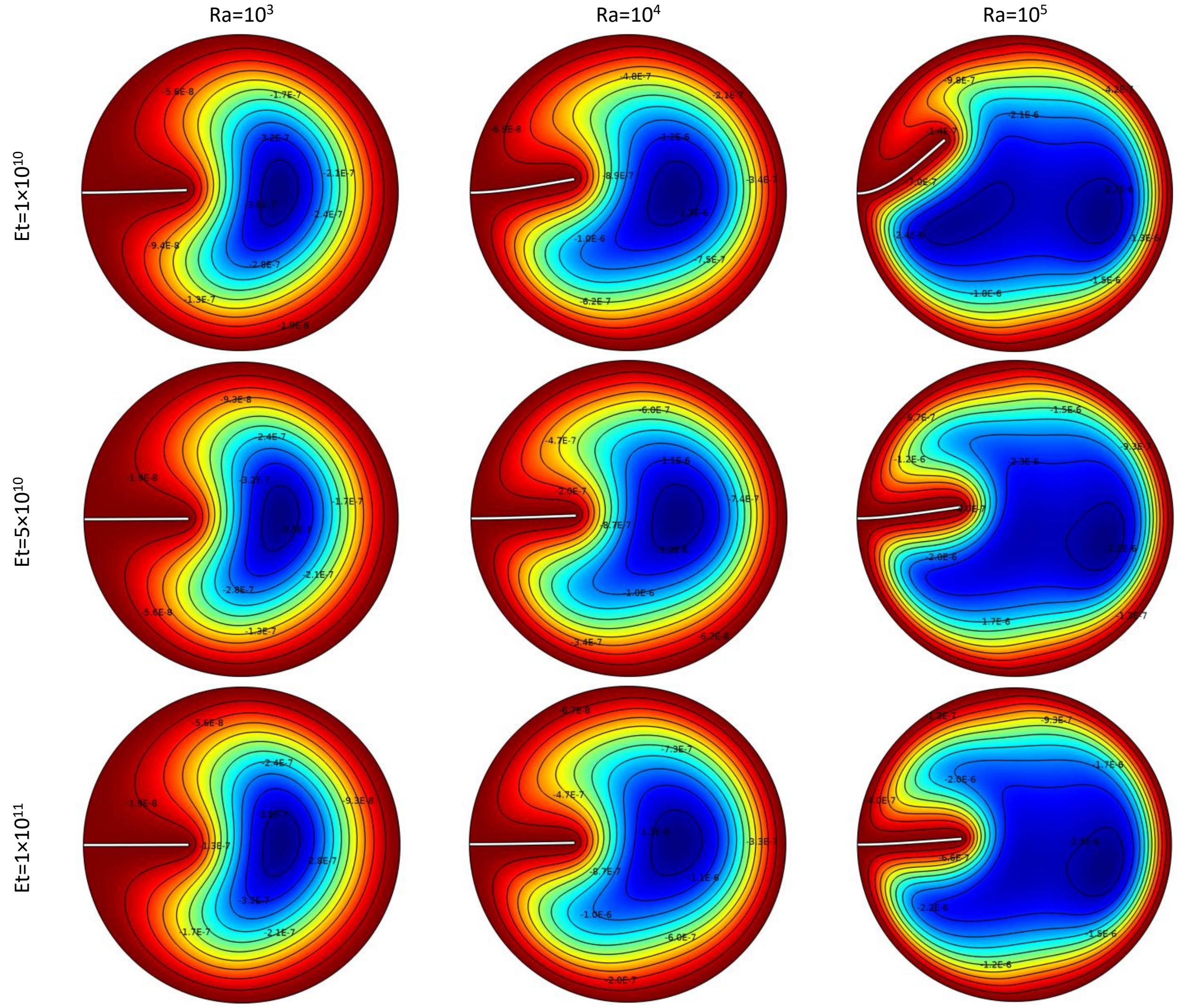

*Figure 8. Streamline contours for various Rayleigh numbers (Ra) and different values of elasticity modulus (Et) at Pr = 10*

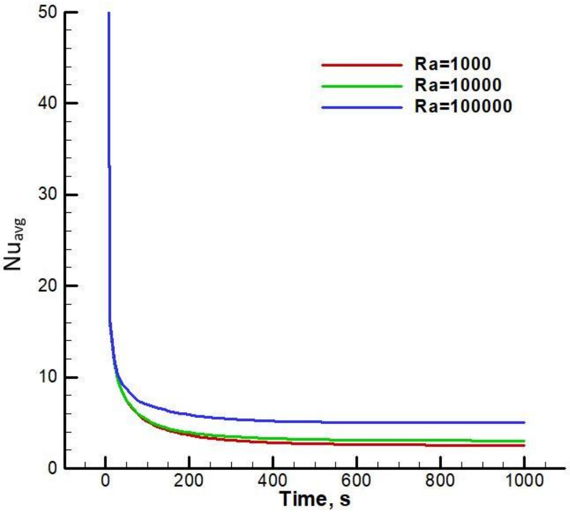

*Figure 9. The average Nusselt number along the hot wall over time for different Rayleigh numbers at Et = $10^{10}$ and Pr = 10*

Figure 10 presents the average Nusselt number on the hot wall over time for different values of elasticity modulus at Ra =$10^5$ and Pr = 10. This number decreases as the elasticity modulus reduces. Globally, the elasticity modulus has a negligible effect on the average Nusselt number. The higher average Nusselt number is seen at the steady state for the highest elasticity modulus (Et = $10^{11}$).

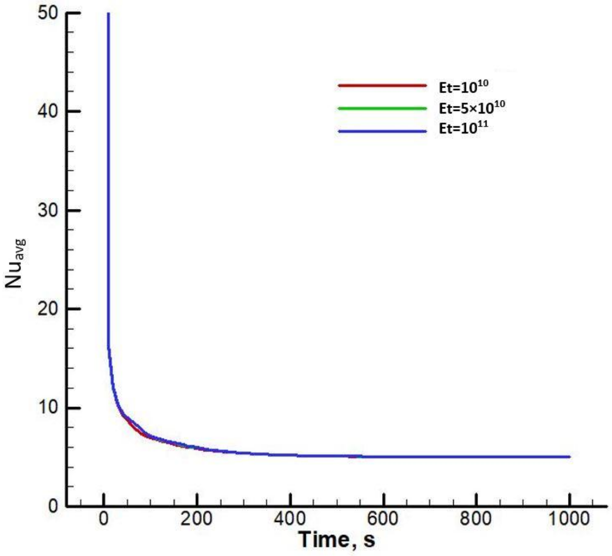

*Figure 10. The average Nusselt number ($Nu_{avg}$) along the hot wall over time for different elasticity modulus at Et = $10^{10}$ and Pr = 10*

Figure 11 shows the velocity magnitude along the vertical centerline of the cavity at the steady state for different Rayleigh numbers at Et = $10^{10}$ and Pr = 10. The maximal velocity values were observed in the fluid near the lower and upper walls at the highest Rayleigh number. Notably, lower velocity values can be seen at the level of the flexible fin for all Rayleigh numbers.

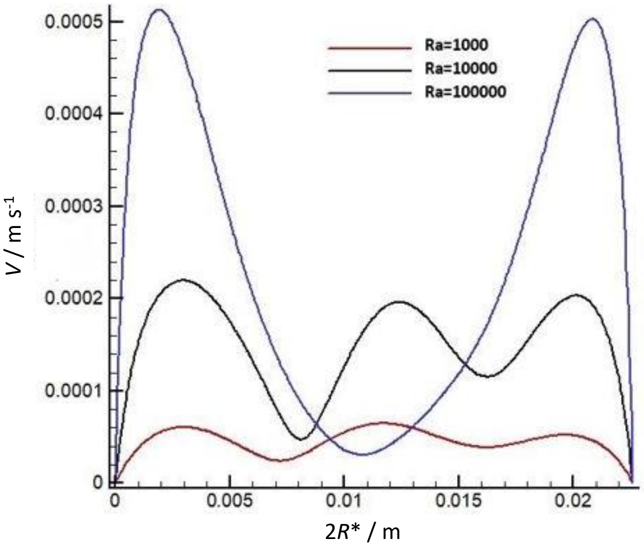

*Figure 11. Velocity (V) along the vertical centerline for different Rayleigh numbers at Et = $10^{10}$ and Pr = 10*

Figure 12 depicts the steady-state velocity values along the vertical centerline of the cavity for different elasticity moduli at Ra = $10^5$ and Pr = 10. As can be seen, the elastic modulus has a negligible effect on fluid velocity. It is worth noting that the fluid velocity decreases at the maximal deformation of the flexible fin.

Figure 13 illustrates the maximum stress values with the deformation of the flexible fin for different Rayleigh numbers at Et = $10^{10}$ and Pr = 10. As observed, the maximum deformation of the fin increases by increasing the Rayleigh number. This finding is due to the augmented effect of the natural convective flow. Also, at a low Rayleigh number natural convective heat transfer is reduced and values of maximum deformation become lower.

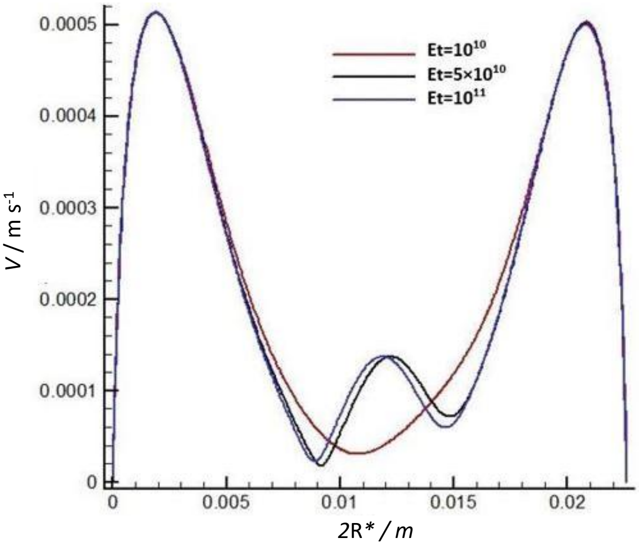

*Figure 12. Velocity (V) along the vertical centerline for different elasticity modulus at Ra = $10^5$and Pr = 10.*

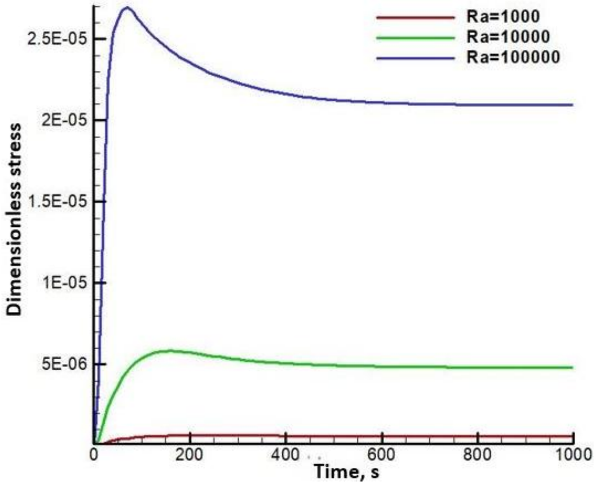

*Figure 13. Maximal stress values of the flexible fin for different Rayleigh numbers at Et = $10^{10}$ and Pr = 10*

Figure 14 shows the maximum stress values with the deformation of the flexible fin for different elasticity moduli at Ra = $10^5$ and Pr = 10. The maximum deformation of the fin increases as the elasticity modulus is decreased, resulting in a greater degree of flexibility and higher overall maximal deformation. When the elasticity modulus increases, the fin becomes more rigid, and the maximal deformation decreases.

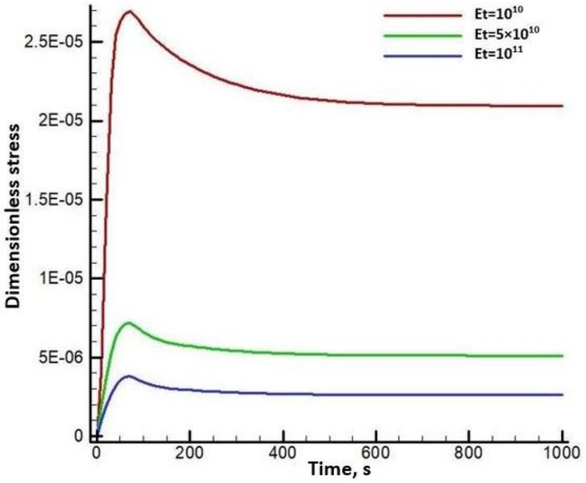

*Figure 14. Maximal deformation stress values of the flexible fin over time for different elasticity modulus at Ra = $10^5$and Pr = 10.*

Figure 15 illustrates the impact of the fin length on the stress with the deformation of the flexible fin overtime at Et = $10^{10}$ and Ra = $10^5$. It has been observed that the stress and deformation of the fin increase as the fin length is increased.

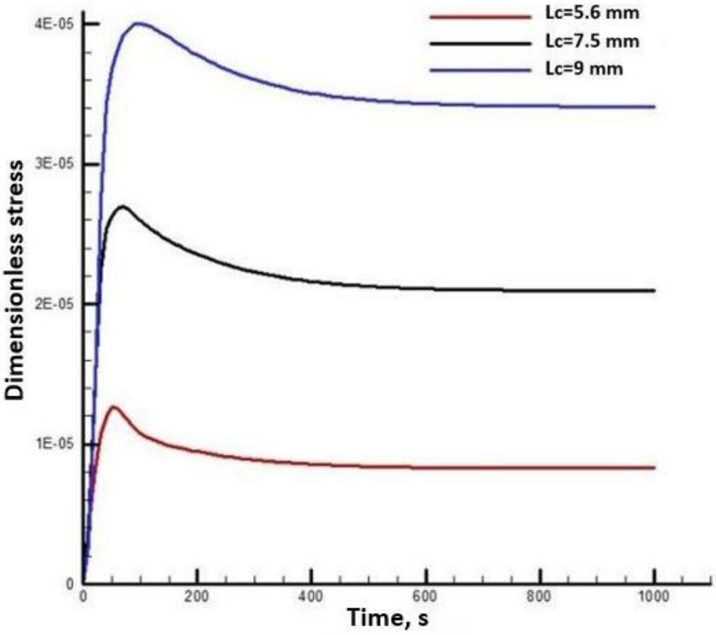

*Figure 15. Maximum stress values of the flexible fin over time for different fin lengths (Lc) at Ra = $10^5$ and Et = $10^{10}$*

Figure 16 depicts the Nusselt number along the hot wall over time for different fin positions (left side, right side, and top side) at Et = $10^{10}$ and Ra = $10^5$. As can be seen, attachment of the fin at the top of the cavity has an improving impact on the heat transfer. It is worth noting that the left (hot wall) and right (cold wall) positions of the fin have the same effects on heat transfer.

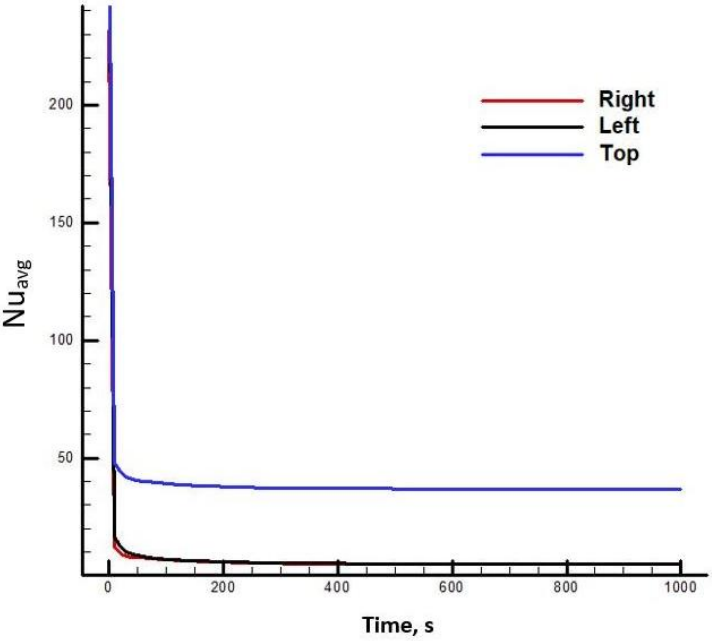

*Figure 16. The average Nusselt number along the hot wall over time for different fin positions at Et = $10^{10}$ and Ra = $10^5$*

Figure 17 represents the fin maximal stress over time for different fin positions at Ra = $10^5$ and Et = $10^{10}$. The right fin position shows the maximal deformation stress, while the top position results in the lowest fin deformation stress.

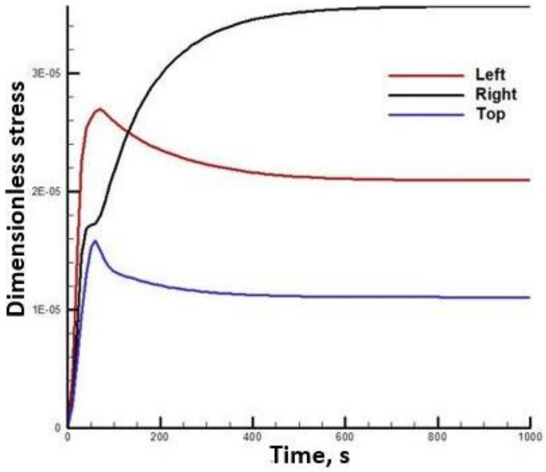

*Figure 17. Maximum stress values of the flexible fin over time for different fin positions at Ra = $10^5$ and Et = $10^{10}$*

## 5. CONCLUSION

Numerical investigations have been carried out on natural convective flow for Newtonian fluids in a circular enclosure using the finite elements method. The influences of the Rayleigh number (Ra) and elasticity modulus (Et) on the convective flow and heat transfer have been examined and discussed. Summary of the major results is as follows.

- Conduction is the primary mode of heat transfer in the early stages, but it gradually converts to natural convection. For higher Rayleigh numbers, the effects of the buoyancy force on vortices that form in the cavity are most important.
- The highest deformation of the fin is observed at the steady state when the fin elasticity modulus is low. Still the elasticity modulus does not affect the average Nusselt number on the hot wall.
- The increase in the Rayleigh number causes an increase in the convective flow intensity and heat transfer,
- It may be deduced that the placement of the fin on the top of the cavity improves heat transfer.

## REFERENCES

[1] Turkyilmazoglu M. Exponential nonuniform wall heating of a square cavity and natural convection. *Chin J Phys*. 2022; 77: 2122-2135.https://dx.doi.org/10.1016/j.cjph.2021.12.021

[2] Mehryan SAM, Ghalambaz M, Ismael MA, Chamkha AJ. Analysis of fluid-solid interaction in MHD natural convection in a square cavity equally partitioned by a vertical flexible membrane. *J Magn Magn*. 2016; 424: 161-173. https://dx.doi.org/10.1016/j.jmmm.2016.09.123

[3] Jamesahar I, Halambaz MG, Chamkha AJ. Fluid–solid interaction in natural convection heat transfer in a square cavity with a perfectly thermal-conductive flexible diagonal partition. *Int J Heat Mass Transf*. 2016; 100: 303-319. https://dx.doi.org/https://doi.org/10.1016/j.ijheatmasstransfer.2016.04.046

[4] Shahrestani AB, Alshuraiaan B, Izadi M. Combined natural convection-FSI inside a circular enclosure divided by a movable barrier. *Int Commun Heat Mass Transf*. 2021; 126: 105426. https://dx.doi.org/10.1016/j.icheatmasstransfer.2021.105426

[5] Ghalambaz M, Mehryan SAM, Alsabery AI, Hajjar A, Izadi M,Chamkha A. Controlling the natural convection flow through a flexible baffle in an L-shaped enclosure. *Meccanica*. 2020; 55: 1561-1584. https://dx.doi.org/10.1007/s11012-020-01194-2

[6] Ismael MA, Jasim HF. Role of the fluid-structure interaction in mixed convection in a vented cavity. *Int J Mech. Sci*. 2017; 135: 190-202. https://dx.doi.org/10.1016/j.ijmecsci.2017.11.001

[7] Sabbar WA, Ismael MA, Almudhaffar M. Fluid-structure interaction of mixed convection in a cavity-channel assembly of flexible wall. *Int J Mech. Sci*. 2018; 149: 73-83. https://dx.doi.org/10.1016/j.ijmecsci.2018.09.041

[8] Alsabery AI, Selimefendigil F, Hashim I, Chamkha AJ, Ghalambaz M. Fluid-structure interaction analysis of entropy generation and mixed convection inside a cavity with flexible right wall and heated rotating cylinder. *Int J Heat Mass Transf*. 2019; 140: 331-345. https://dx.doi.org/10.1016/j.ijheatmasstransfer.2019.06.003

[9] Alsabery AI, Sheremet MA, Ghalambaz M, Chamkha AJ, Hashim I. Fluid-structure interaction in natural convection heat transfer in an oblique cavity with a flexible oscillating fin and partial heating. *Appl Therm Eng*. 2018; 145: 80-97. https://dx.doi.org/10.1016/j.applthermaleng.2018.09.039

[10] Ghalambaz M, Jamesahar E, Ismael MA, Chamkha AJ. Fluid-structure interaction study of natural convection heat transfer over a flexible oscillating fin in a square cavity. *Int J Therm Sci*. 2016; 111: 256-273. https://dx.doi.org/10.1016/j.ijthermalsci.2016.09.001

[11] Saleh H, Naganthran K, Hashim I, Ghalambaz M, Nazar R. Role of fluid-structure interaction in free convection in square open cavity with double flexible oscillating fins. *Alex Eng J*. 2021; 61: 1217-1234. https://dx.doi.org/10.1016/j.aej.2021.04.073

[12] Raisi A, Arvin I. A numerical study of the effect of fluid-structure interaction on transient natural convection in an air-filled square cavity. *Int J Therm Sci*. 2018; 128: 1-14. https://dx.doi.org/10.1016/j.ijthermalsci.2018.02.012

[13] Khanafer K, Vafai K. Effect of a circular cylinder and flexible wall on natural convective heat transfer characteristics in a cavity filled with a porous medium. *Appl Therm Eng*. 2020; 181: 115989. https://dx.doi.org/10.1016/j.applthermaleng.2020.115989

[14] Khalil WH, Azzawi IDJ, Al-damook A. The optimisation of MHD free convection inside porous trapezoidal cavity with the wavy bottom wall using response surface method. *Int Commun Heat Mass Transf*. 2022; 134: 106035. https://dx.doi.org/10.1016/j.icheatmasstransfer.2022.106035

[15] Moria H. Natural convection in an L-shape cavity equipped with heating blocks and porous layers. *Int Commun Heat Mass Transf*. 2021; 126: 105375. https://dx.doi.org/10.1016/j.icheatmasstransfer.2021.105375

[16] Saleh H, Hashim I, Jamesearl E, Ghalambaz M. Effects of flexible fin on natural convection in enclosure partially-filled with porous medium. *Alex Eng J*. 2020; 59: 3515-3529. https://dx.doi.org/10.1016/j.aej.2020.05.034

[17] Mehryan SAM, Alsabery A, Modir A, Izadpanahi E, Ghalambaz M. Fluid-structure interaction of a hot flexible thin plate inside an enclosure. *Int J Therm Sci*. 2020; 153: 106340. https://dx.doi.org/10.1016/j.ijthermalsci.2020.106340

[18] Savio RR, Shaik S, Kumar RS. Numerical study of natural convection around a square cylinder within a square enclosure for different orientations. *J Therm Anal Calorim*. 2021; 147: 1711-1725. https://dx.doi.org/10.1007/s10973-020-10499-z

[19] Subhani S, Kumar RS. Natural Convection Heat Transfer Enhancement of Circular Obstacle within Square Enclosure. *J Therm Anal Calorim*. 2021; 147: 4711-4729. https://dx.doi.org/10.1007/s10973-021-10829-9

[20] Pal GC, Nammi G, Pati S, Randive PR, Baranyi L. Natural convection in an enclosure with a pair of cylinders under magnetic field. *Case Stud Therm Eng*. 2022; 30: 101763. https://dx.doi.org/10.1016/j.csite.2022.101763

[21] Long T, Huang C, Hu D, Liu M. Coupling edge-based smoothed finite element method with smoothed particle hydrodynamics for fluid structure interaction problems. *Ocean Eng*. 2021; 225: 108772. https://dx.doi.org/10.1016/j.oceaneng.2021.108772

[22] Hakim MdA, Ahad AI, Karim AUl, Saha S, Hasan MN. Fluid structure interaction and heat transfer enhancement with dynamic flexible flow modulator. *Int Commun Heat Mass Transf*. 2022; 134: 105983. https://dx.doi.org/10.1016/j.icheatmasstransfer.2022.105983

[23] Gilmanov A, Le TB, Sotiropoulos FA. Numerical approach for simulating fluid structure interaction of flexible thin shells undergoing arbitrarily large deformations in complex domains. *J Comput Phys*. 2015; 300: 814-843. https://dx.doi.org/10.1016/j.jcp.2015.08.008

[24] Shahabadi M, Mehryan SAM, Ghalambaz M, Ismael M. Controlling the natural convection of a non-Newtonian fluid using a flexible fin. *Appl Math Model*. 2020; 92: 669-686. https://dx.doi.org/10.1016/j.apm.2020.11.029

[25] Ghalambaz M, Mehryan SAM, Feeoj RK, Hajjar A, Hashim I, Mahan RB. Free convective heat transfer of a non-Newtonian fluid in a cavity containing a thin flexible heater plate: an Eulerian–Lagrangian approach. *J Therm Anal Calorim*. 2020; 147: 1809-1824. https://dx.doi.org/10.1007/s10973-020-10292-y

[26] Zadeh SMH, Mehryan SAM, Izadpanahic E, Ghalambaz M. Impacts of the flexibility of a thin heater plate on the natural convection heat transfer. *Int J Therm Sci*. 2019; 145: 106001. https://dx.doi.org/10.1016/j.ijthermalsci.2019.106001

[27] Sairamu M, Chhabra RP. Natural convection in power-law fluids from a tilted square in an enclosure. *Ocean Eng*. 2012; 56: 319-339. https://dx.doi.org/j.ijheatmasstransfer.2012.09.033

[28] Turan O, Sachdeva A, Chakraborty N, Poole RJ. Laminar natural convection of power-law fluids in a square enclosure with differentially heated side walls subjected to constant temperatures. *J Non-Newton Fluid Mech*. 2011; 166: 1049-1063. https://dx.doi.org/10.1016/j.jnnfm.2011.06.003

[29] Su ZG, Li TF, Luo K, Wu J, Yi HL. Electro-thermo-convection in non-Newtonian power-law fluids within rectangular enclosures. *J Non-Newton Fluid Mech*. 2020; 288: 2122-2135. https://dx.doi.org/10.1016/j.jnnfm.2020.104470

[30] Salehpour A, Sadatlub MA, Sojoudi A. Unsteady Natural Convection in a Differentially Heated Rectangular Enclosure Possessing Sinusoidal Corrugated Side Walls Loaded with Power Law Non-Newtonian Fluid. *Fluid Dyn*. 2019; 54: 159-176. https://dx.doi.org/10.1134/S0015462819010129

[31] Gangawane KM, Manikandan B. Laminar natural convection characteristics in an enclosure with heated hexagonal block for non-Newtonian power-law fluids. *Chin J Chem Eng*. 2016; 25: 555-571. https://dx.doi.org/10.1016/j.cjche.2016.08.028

[32] Zhou X, Sun Z. Numerical investigation of non-Newtonian power-law flows using B-spline material point method. *J Non-Newton Fluid Mech*. 2021; 298: 104678. https://dx.doi.org/10.1016/j.jnnfm.2021.104678

[33] Pandey S, Cho HW, Choi HK, Park YG, Seo YM, Ha MY. Thermal and flow characteristics of buoyancy-driven non-Newtonian flows at a high Rayleigh number of $10^7$ and predictions from an artificial neural network. *J Mech Sci Technol*. 2021;35: 1791-1805. https://dx.doi.org/10.1007/s12206-021-0341-6

[34] KebritiS, Moqtaderi H. Numerical simulation of convective non-Newtonian power-law solid-liquid phase change using the lattice Boltzmann method. *Int J Therm Sci*. 2020; 159: 106574. https://dx.doi.org/10.1016/j.ijthermalsci.2020.106574

[35] Jain SR, Subhani S, Kumar, RS. Numerical study on performance enhancement of a square enclosure with a circular cylinder of varying geometries. *J Therm Anal Calorim*. 2021; 147: 2579-2599. https://dx.doi.org/10.1007/s10973-021-10641-5

[36] Loenko DS, Shenoy A, Sheremet MA. Effect of time-dependent wall temperature on natural convection of a non-Newtonian fluid in an enclosure. Ocean Eng. 2021; 166: 319-339. https://dx.doi.org/10.1016/j.ijthermalsci.2021.106973

[37] Abdulkadhim A, Abed IM, Said NM. Review of Natural Convection Within Various Shapes of Enclosures. Arab J Sci Eng. 2021; 46: 11543-11586. https://dx.doi.org/10.1007/s13369-021-05952-6

[38] Yang P, Huang C, Zhang Z, Long T, Liu M. Simulating natural convection with high Rayleigh numbers using the Smoothed Particle Hydrodynamics method. *Int J Heat Mass Transf*. 2020; 166: 2122-2135. https://dx.doi.org/10.1016/j.cjph.2021.12.021

# Numeričko ispitivanje slobodne konvekcije unutar kružne šupljine sa fleksibilnim perajem

**Atika Bencherif[1], Mohamed Bouzit[1], Abderrahim Mokhefi[2], Hanaa Derraz[1] i Fatima Zohra Khelif[1]**

*[1]Laboratory of Maritime Sciences and Engineering LSIM Faculty of Mechanical Engineering, University of Science and Technology of Oran Mohamed Boudiaf, Oran, Algeria*

*[2]Mechanics, Modeling and Experimentation Laboratory L2ME, Faculty of Sciences and Technology, Bechar University, Bechar, Algeria*

(Naučni rad)

*Izvod*

U ovom radu numerički je proučavan problem nestalne prirodne konvekcije unutar kružne šupljine koja sadrži fleksibilno peraje. Leva strana šupljine je vruća, dok je desna hladna. Fleksibilno elastično peraje je pričvršćeno za centar vrućeg zida. Interakcija fluida i strukture u šupljini i fleksibilnim perajem je kombinovana sa Njutnovim fluidom. Glavne jednačine interakcije fluid-fleksibilna peraja su rešene primenom metode konačnih elemenata i proizvoljnog Lagranž-Eulerovog pristupa. U ovoj studiji ispitivani su efekti elastičnog fleksibilnog peraja na prirodnu konvekciju unutar kružnih šupljina. Rejlijev broj ($10^3 \leq Ra \leq 10^5$) i modul elastičnosti ($10^{10} \leq Et \leq 10^{11}$) su parametri koji su ispitivani, kao i prosečni Nuseltovi brojevi i izoterme i strujne linije. Rezultati pokazuju da povećanje Relejovog broja izaziva povećanje prosečnog Nuseltovog broja, koji postaje značajan za veći Rejlijev broj. Time je otkriveno da kružni oblik šupljine može poboljšati brzinu prenosa toplote.

*Ključne reči:* Njutnovski fluid; interakcija fluid-struktura; metoda konačnih elemenata; modul elastičnosti; prosečan Nuseltov broj; Rejlijev broj

# Harnessing the potential of selected plant pigments in dye-sensitized solar cells: the current status

**Anita M. Lazić**[1]**, Luka R. Matović**[1]**, Nemanja P. Trišović**[2] **and Nataša V. Valentić**[2]

[1]*Innovation Center of the Faculty of Technology and Metallurgy, Belgrade, Serbia*
[2]*University of Belgrade, Faculty of Technology and Metallurgy, Belgrade, Serbia*

LET'S REFRESH OUR KNOWLEDGE

**UDC: 667.272/.276:621.383.51**

*Hem. Ind.* **79(1)** 47-65 (2025)

*Abstract*

Dye-sensitized solar cells (DSSC) represent the third generation of solar cells which have revolutionized sustainable energy research owing to the fact that they act as a renewable energy source integrated with employment of environmentally benign light-harvesting pigments as sensitizers and cost-effective materials for manufacture. This review compiles the exploration of plant pigments with a potential for use as photosensitizers in solar cells, focusing on their isolation and the factors that affect their physicochemical properties to identify those pigments providing the optimum performance. Newly reported considerations of flavonoids, anthocyanins, carotenoids, betalains, and chlorophyll, as light-harvesting pigments are summarized. Further, outcomes of the solar cell efficiency obtained by various semiconductors and types of electrolytes are compared and discussed. The main goal of this review is to highlight the significance of naturally obtained light-harvesting pigments, which will be used as the promising class of sensitizers in DSSC.

*Keywords:* photovoltaics; flavonoids; anthocyanins; carotenoids; betalains; chlorophyll

## 1. INTRODUCTION

It is a well-known fact that the daily energy utilization is about 17.4 TW worldwide of which 80% is gained from natural gas, fossil fuels, and coal. To find a sustainable energy source which is environmentally friendly and cheap, scientists suggest the use of solar power. Solar radiation is about 3.8 million exajoules per year, namely 10,000 times more than humanity needs [1]. In addition, solar power represents renewable source of energy that could be applied as one-time investment and, during the photovoltaic transformation, harmful gases are not released [2]. Since the production of electric energy by illumination of certain organic molecules was disclosed in the 1960s [3], dye-sensitized solar cells (DSSCs) have revolutionized sustainable energy research [2]. Due to eco-friendly preparation methods that require the use of cost-effective materials [2], DSSCs have been extensively studied.

According to their architecture and the type of implemented materials, all solar cells are generally classified into four main categories termed generations [2,4-6].

1) First generation
    - Crystalline Si
        - Monocrystalline Si
        - Polycrystalline (multicrystalline) Si
    - III-V Single-junction solar cells
2) Second generation
    - Amorphous Si (a-Si)
    - Microcrystalline Si (μc-Si)
    - Chalcogenides
        - Copper-Indium-Gallium-Selenide (CIGS)
        - Cadmium-Telluride (CdTe)
        - Cadmium-Sulphide (CdS)
        - Others

---

Corresponding authors: Nataša V. Valentić, University of Belgrade, Faculty of Technology and Metallurgy, Karnegijeva 4, 11120, Belgrade
Paper received: 18 February 2025; Paper accepted: 30 March 2025; Paper published: 15 April 2025.
E-mail: naca@tmf.bg.ac.rs
https://doi.org/10.2298/HEMIND250218007L

3) Third generation
    - Dye-sensitized solar cells (DSSC)
    - Perovskite solar cells (PSC)
    - Quantum dot-sensitized solar cells (QDSSC)
    - Organic and polymer materials (OPV)
    - III-V Multi-junction solar cells
4) Fourth generation
    - Graphene and its derivatives
    - Carbon nanotubes
    - Metal nanoparticles and metal oxides.

The conventional structure/design of a DSSC (proposed by O'Regan and Gratzel) consists of four fundamental parts:

1. a photoanode—mesoporous metal oxide (usually $TiO_2$) adsorbed on the transparent conductive oxide (TCO; usually fluorine-doped tin oxide (FTO) or indium tin oxide (ITO)) of a glass substrate,
2. a sensitizer—a dye molecule,
3. an electrolyte—usually a $I_3^-/3I^-$ redox couple in aprotic polar organic solvent, and
4. a photocathode—photocatalytic material adsorbed onto TCO of a glass substrate [7].

To address the challenges associated with the application of synthetic dyes as sensitizers in DSSCs, such as a high cost, propensity to degradation and employment of toxic substances, biocompatible natural sensitizers have been applied. These natural sensitizers contain various pigments managing the absorption of light and insert of charges to the conduction band of $TiO_2$ [7].

It was demonstrated in literature [8] that a DSSC containing a mixture of anthocyanin pigment, more precisely, a mixture of cyanin-3-glycoside and cyanin-3-rutinoside, as a sensitizer for $TiO_2$, can produce a conversion efficiency of $\eta$ = 0.56 %, the open-circuit voltages in the range of $V_{oc}$ = 0.4 to 0.5 V, and short-circuit currents in the range of $J_{SC}$ = 1.5 to 2.2 mA cm$^{-2}$. Additionally, the maximum current of 4 mA, the maximum voltage of 300 mV and the overall efficiency of 1 % were obtained by using a blackberry extract to sensitize $TiO_2$ [9]. Garcia and coworkers revealed that employment of natural dyes extracted from chaste tree fruit, mulberry and cabbage-palm as $TiO_2$ sensitizers, produce a short-circuit current and open-circuit voltage close to those of conventional dyes [10]. Inspired by these results, this review compiles the performance of natural dye based DSSCs coupled with different biocompatible plant pigments extracted from diverse natural products and implemented in solar cells. Recent explorations of plant pigments are coupled with data about their chemical stability, extraction, and purification methods. In addition, a comparative study based on the findings of various research groups related to natural dye-sensitized solar cells is also described. The main goal of this review is to highlight the application potential of natural pigments as sensitizers for the future development of solar cells with promising performance.

## 2. CLASSIFICATION OF LIGHT-HARVESTING PIGMENTS AND APPLICATION-BASED FUTURE PERSPECTIVES

Pigments occurring in plants represent one of the most important natural components for absorption of solar radiation and generation of electrons. To ensure the optimal performance of DSSCs, two conditions should be fulfilled: a greater number of so-called light-harvesting pigments extracted from different parts of plants and the existence of anchoring groups (*e.g.* hydroxyl, carbonyl group) for chemisorption of the dye molecule on semiconductor's surface [2]. In accordance with this, an efficient light-harvesting pigment should fulfil the following:

1. broad absorption in the visible and near-infrared part of the solar spectrum, providing a high molar attenuation coefficient,
2. a strong interaction with the semiconductor's surface through the anchoring groups, in order to provide the efficient injection of photoexcited electrons from the LUMO (lowest unoccupied molecular orbital) of the dye to the conduction band (CB) of the semiconductor,
3. faster injection rate of photoexcited electrons compared to the rate of decomposition of the dye,
4. a value of the LUMO energy level of the dye higher than the value of CB energy level of the semiconductor to enable injection of photoexcited electrons,

5. a value of the HOMO (highest occupied molecular orbital) energy level of the dye lower than the value of the redox couple energy level to enable efficient reduction of the oxidized dye molecule/regeneration of the oxidized dye molecule [1].

A literature review indicates that plant compounds such as flavonoids, anthocyanins, carotenoids, betalains and chlorophyll, meet these criteria and possess advantages including: large absorption coefficients, high light-harvesting efficiencies, biodegradability, low production costs and easy processability [2,11].

In recent years, there has been a growing number of papers and patents dealing with application of natural pigments in DSSCs [12-15]. Here, we provide a new perspective on their selection with the emphasis on molecular scaffolds and functional groups that influence, among others, the following properties: the pigment stability, light absorption and the electron injection efficiency. In this context, the classification of natural pigments is presented in detail together with their sourcing. A key insight from this review is the structural variety of natural pigments, which offers guidelines for optimizing their properties to improve the DSSC efficiency and operational stability.

### 2. 1. Flavonoids

In the 1930s, a new compound isolated from oranges was recognized as a vitamin family member and was named vitamin P. It was later discovered that it was the unique antioxidant flavonoid (rutin, citrus flavonoid glycoside) [16]. Flavonoids comprise different polyphenolic compounds found in plants. The core structure of these polyphenolics is built of a 15-carbon phenyl-benzopyrone skeleton (C6-C3-C6 system), which consists of a benzene ring (designated as B) associated to a benzo-gamma-pyrone structure (condensed fragments A and C) (Figure 1) [17-19].

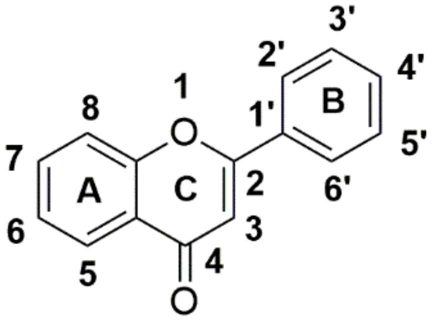

***Figure 1.*** *General structure of flavonoids*

Flavonoids are present in plants as both aglycones (free form) and *O*-glycosidic (rarely *C*-glycosidic) conjugates that is the most frequent form; other altered forms exist as well [19,20]. *O*-glycosides are less reactive, but more polar and their transport across cell membranes is improved [19,20]. In the *O*-glycosidic form, at least one hydroxyl group is connected with a sugar moiety (*e.g.* glucose, galactose, rhamnose, xylose *etc.*) *via* the acid-labile acetal bond in the following way: the hydroxyl group at C7 in flavones, flavanones and isoflavones, the hydroxyl group at C3 and C7 in flavonols and flavanols and the hydroxyl group at C3 and C5 in flavonoid-related anthocyanidins [20].

Flavonoid compounds are very abundant natural plant pigments secreted as secondary metabolites. In times of stress, plants often release secondary metabolites as a defensive response. These flavonoid phytochemicals can serve as signal molecules, UV-filters and scavengers for reactive oxygen species (ROS) and have essential roles in enhancing tolerance to drought, heat, and freezing conditions [17,20,21]. Among the flavonoid family, there are various subclasses such as flavones, flavonols, flavanones, flavanonols, isoflavones, flavanols, anthocyanidins and others (*e.g.* chalcones and aurones) [16,20]. The general structures and examples of some typical flavonoid subclasses are shown in Table 1. In this review, anthocyanidins are especially highlighted because of their great importance among the light-harvesting plant pigments; they are not bundled with the rest of flavonoids. According to unsaturation and oxidation degree of the central heterocyclic ring C (Figure 1), most of flavonoids are divided into flavones and flavonols (possess the benzo-gamma-pyrone moiety) and their dihydro derivatives. Flavan-3-ols are somewhat different from the rest, because they do not possess a carbonyl group in the heterocyclic moiety. The position of the benzenoid substituent classifies them into flavonoids (2-position) and isoflavonoids (3-position) [16,20]. There are also homoisoflavonoids, an infrequent flavonoid subclass, with a core structure similar to isoflavonoids, but with a 16-carbon skeleton (*e.g.* sappanin-type homoisoflavonoids bear a 3-benzylchroman-4-one key unit) [22,23].

***Table 1.***General structures and examples of some typical flavonoid subclasses*

| Subclass of flavonoid | General structure | Examples |
|---|---|---|
| Flavones | 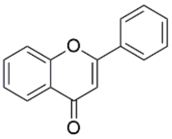 | 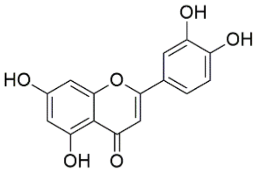<br>Luteolin<br>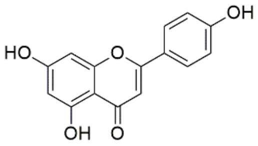<br>Apigenin<br>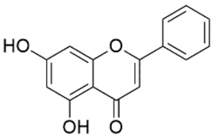<br>Chrysin |
| Flavonols | 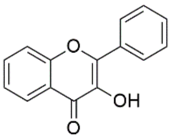 | 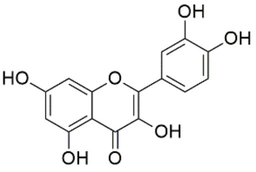<br>Quercetin<br>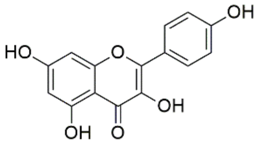<br>Kaempferol<br>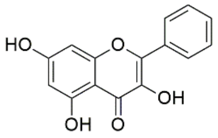<br>Galangin |
| Flavanones | 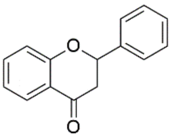 | 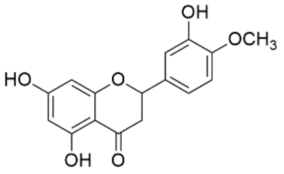<br>Hesperetin<br>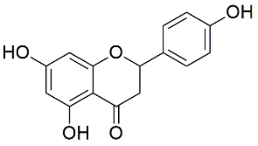<br>Naringenin |
| Flavanonols | 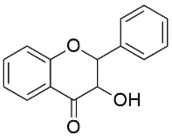 | 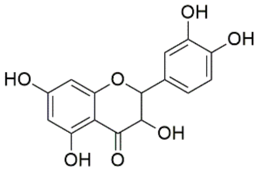<br>Taxifolin |
| Isoflavones | 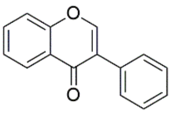 | 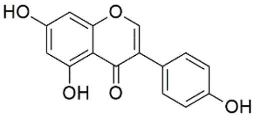<br>Genistein<br>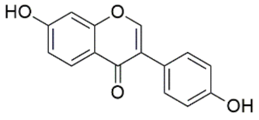<br>Daidzein |
| Flavan-3-ols | 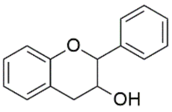 | 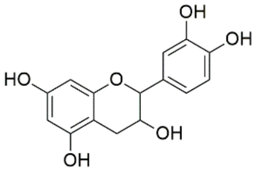<br>Catechin<br>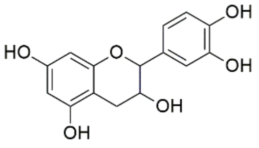<br>Epicatechin |
| Homoiso-flavonoids | Five basic scaffolds | 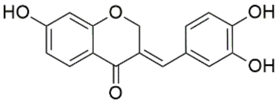<br>Sappanone A<br>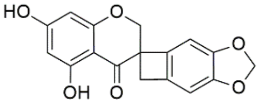<br>Scillascillin<br>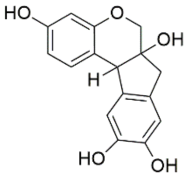<br>Brazilin |

The wide application of flavonoids in the various branches of industry implies the existence of various methods for their extraction. The polarity of flavonoid molecules is crucial for the solvent selection. For example, highly alkylated aglycones are extracted using ethyl acetate, while the more hydroxylated aglycones are extracted using acetone, alcohol, water of their mixtures [17].

Using flavonoids and betacyanins (water-soluble, nitrogen-containing pigments) extracted from *Nerium Oleander*, *Tecomastan*, and *Bougainvillea* as light-harvesting pigments, and $TiO_2$ nanoparticles as semiconductor implied on a FTO glass plate, Devi and coworkers fabricated DSSC with $V_{oc}$ in the range of 132 to 554 mV, $J_{sc}$ in the range of 3.22 to 15.22 mA cm$^{-2}$, and $\eta$ in the range of 0.30-0.68 % [24]. Results of an optical analysis indicated that the observed efficient sensitizing behaviour of the pigments can be related to the $n \rightarrow \pi^*$ and $\pi \rightarrow \pi^*$ electronic transitions in the heterocyclic moieties of flavonoids and betacyanins [24]. Homoisoflavonoids isolated from *Caesalpinia sappan* represent interesting optically active pigments because, upon excitation at 383 nm, they produce emission at 563 nm, while the results of a current-voltage analysis indicate good photovoltaic performances as follows: $V_{oc}$ = 487 mV, $J_{sc}$ = 0.10 mA cm$^{-2}$ and a fill factor (FF) of 87.6 % [25]. In another study, it was demonstrated that a DSSC containing chokeberry (*Aronia melanocarpa*) juice pigments as sensitizers had the photovoltaic parameters similar to those of the Ru(II) complex N719 as a reference dye [26]. By using hybrid nanostructures like $TiO_2$ hollow spheres of tetragonal form as semiconductor, and natural pigments isolated from *Punica garanatum* and *Acacia catechu*, a DSSC was fabricated with a higher power conversion efficiency (PCE) of 0.26, $V_{oc}$ of 530 mV and a fill factor of 85 % [27]. At the same time, in another research it was denoted that cells built from crude plant extracts containing mixtures of alkaloids, carotenoids, flavonoids and antraquinones, with $TiO_2$ as semiconductor, produce a respectable $V_{oc}$ and very low $J_{sc}$ compared to the standard cell containing the N719 dye. Among them, the highest performance exhibited a cell containing extract isolated from *Sorghum bicolor*, with a maximum power of $P_{max}$ = 0.18 mW/cm$^2$, which can be attributed to a high anthocyanin content [28]. By using extracts from *Trifolium pratense*, *Mirabilis jalapa* and *Bassia scoparia*, Muhammad and coworkers constructed a DSSC with the efficiency of 0.15, 0.05 and 0.18 %, respectively [29]. According to the fluorescence spectroscopy analysis, chlorophyll extracted from *Bassia scoparia* displayed the highest light absorption, photon emission and stacking capability with $TiO_2$ semiconductor [29]. Spectral properties of flavonoids isolated from red/yellow gambier fruits suggest that these pigments have a high application potential as natural light-harvesting pigments in solar cells. Also, *I-V* measurements showed that the DSSC efficiency linearly correlated with their concentration. An efficiency of 3.248 % was reached in a DSSC with the concentration of yellow gambier fruit pigment of 70 %, while the efficiency of 0.72 % was reached in a DSSC with the concentration of red gambier fruit pigment of 30 % [30]. A DSSC was manufactured by using $TiO_2$ nanostructures and fruit extracts originated from grape, pineapple, and orange (G-$TiO_2$, P-$TiO_2$ and O-$TiO_2$, respectively) as reducing agents (or electron donors) and using flavonoids isolated from *Murraya koenigii* as a natural sensitizer [31]. Owning to a light scattering ability and a strengthened electron transfer related to the above-mentioned analogs, the DSSC constituted of G-$TiO_2$ exerted the best photovoltaic parameters: $V_{oc}$ = 628 mV, $J_{sc}$ = 4.88 mA cm$^{-2}$, FF = 58 % and $\eta$ = 1.78 % [31]. DSSCs were made using flavonoids, isolated from *Argemone mexicana* flower, as photosensitizer and fabricated by employing microwave processing to anneal a $TiO_2$ layer. The optimum photovoltaic parameters were obtained for microwave annealed solar cells with a blocking layer and irradiation time of 7 min. The observed photovoltaic parameters were: $V_{oc}$ = 472 mV, $J_{sc}$ = 2.73 mA cm$^{-2}$, FF = 0.54 % and $\eta$ = 0.69 % [32]. A broad absorption maximum of these pigments at 359 nm, and fast adsorption on the $TiO_2$ surface qualified these flavonoids as appropriate sensitizers for solar cell applications [32]. By using natural pigment scopoletin isolated from *Malva sylvestris*, Karoui and coworkers fabricated a DSSC with a short-circuit density of 0.69 mA cm$^{-2}$ and very stable performance under illumination [33]. To enhance the efficiency of DSSCs containing natural light-harvesting pigments extracted from *Cytisus*, *Alearosea,* and *Roselle*, zinc oxide quantum dots (ZnO-QDs) were applied manufactured through co-precipitation in an ethanolic solution. Results of transmission electron microscopy (TEM), dynamic light scattering (DLS), and photoluminescence (PL) revealed that ZnO-QDs 3 nm in size and a maximum emission intensity in the range 1550 to 520 nm improved the efficiency of the DSSC by 17 % [34]. Table 2 shows the corresponding photovoltaic parameters of DSSCs sensitized with flavonoids, flavonoid-related anthocyanins and other pigments.

***Table 2.*** *Photovoltaic parameters of DSSCs sensitized with flavonoids, flavonoid-related anthocyanins and other pigments*

| No. | Name of plant | Class/name of pigment | Semi-conductor | Electrolyte | Photovoltaic parameters | | | | Ref. |
|---|---|---|---|---|---|---|---|---|---|
| | | | | | $V_{oc}$ / mV | $J_{sc}$ / mA cm$^{-2}$ | FF, % | $\eta$ / % | |
| 1 | Pink *Plumeria rubra* | Flavonoid | $TiO_2$ | $I^-/I^-_3$ | 310 | 0.55 | 0.30 | 0.05 | [28] |
| 2 | Yellow *Plumeria rubra* | Flavonoid | $TiO_2$ | $I^-/I^-_3$ | 420 | 1.12 | 0.32 | 0.15 | [28] |
| 3 | *Nerium oleander* | Flavonoid | Nano-$TiO_2$ | $NaI/I_2$ | 358 | 7.41 | 0.20 | 0.54 | [24] |
| 4 | *Nerium oleander* | Flavonoid | Nano-$TiO_2$ | $KI/I_2$ | 544 | 3.22 | 0.39 | 0.68 | [24] |
| 5 | *Tecoma stan* | Flavonoid | Nano-$TiO_2$ | $NaI/I_2$ | 413 | 3.56 | 0.20 | 0.30 | [24] |
| 6 | *Tecoma stan* | Flavonoid | Nano-$TiO_2$ | $KI/I_2$ | 439 | 3.69 | 0.23 | 0.38 | [24] |
| 7 | *Terminalia chebula* | Flavonoid | $TiO_2$ | $I^-/I^-_3$ | 470 | 0.11 | 0.40 | 0.24 | [27] |
| 8 | Yellow gambier fruit | Flavonoid | $TiO_2$ | $KI/I_2$ | 649 | 1.11 | 0.43 | 3.25 | 30] |
| 9 | Red gambier fruit | Flavonoid | $TiO_2$ | $KI/I_2$ | 442 | 0.76 | 0.21 | 0.72 | [30] |
| 10 | *Murraya koenigii* | Flavonoid | Grape extract+TiO | $I^-/I^-_3$ | 628 | 4.88 | 58 | 1.78 | [31] |
| 11 | *Murraya koenigii* | Flavonoid | Pineapple extract+$TiO_2$ | $I^-/I^-_3$ | 626 | 4.60 | 47 | 1.61 | [31] |
| 12 | *Murraya koenigii* | Flavonoid | Orange extract+$TiO_2$ | $I^-/I^-_3$ | 576 | 6.48 | 40 | 1.52 | [31] |
| 13 | *Argemone mexicana* | Flavonoid | $TiO_2$ | $I^-/I^-_3$ | 427 | 2.73 | 0.54 | 0.69 | [32] |
| 14 | *Biancaea sappan* | Flavone and homoisoflavonoid | $TiO_2$ | $I^-/I^-_3$ | 390 | 0.05 | 0.43 | 0.11 | [27] |
| 15 | *Caesalpinia sappan* | Homoisoflavonoid | $TiO_2$ | $I^-/I^-_3$ | 487 | 0.10 | 87.6 | / | [25] |
| 16 | *Lawsonia inermis* | Lawsone | $TiO_2$ | $I^-/I^-_3$ | 470 | 0.66 | 0.50 | 0.16 | [33] |
| 17 | *Malva sylvestris* | Scopoletin | $TiO_2$ | $I^-/I^-_3$ | 600 | 0.69 | 0.55 | 0.21 | [33] |
| 18 | *Cytisus scoparius* | Flavonoid and Anthocyanin | $TiO_2$ | $I^-/I^-_3$ | 161 | 1.01 | 0.70 | 0.45 | [34] |
| 19 | *Cytisus scoparius* | Flavonoid and Anthocyanin | $TiO_2$/ ZnO-Qd$^a$ | $I^-/I^-_3$ | 614 | 1.18 | 0.67 | 0.49 | [34] |
| 20 | *Alcea rosea* | Flavonoid and Anthocyanin | $TiO_2$ | $I^-/I^-_3$ | 621 | 1.91 | 0.68 | 0.80 | [34] |
| 21 | *Alcea rosea* | Flavonoid and Anthocyanin | $TiO_2$/ZnO-Qd | $I^-/I^-_3$ | 624 | 2.21 | 0.67 | 0.93 | [34] |
| 22 | *Hibiscus sabdariffa* | Flavonoid and Anthocyanin | $TiO_2$ | $I^-/I^-_3$ | 644 | 1.91 | 0.68 | 0.84 | [34] |
| 23 | *Hibiscus sabdariffa* | Flavonoid and Anthocyanin | $TiO_2$/ZnO-Qd | $I^-/I^-_3$ | 648 | 2.25 | 0.65 | 0.98 | [34] |
| 24 | *Acacia catechu* | Catechin and epicatechin | $TiO_2$ | $I^-/I^-_3$ | 580 | 0.20 | 0.84 | 1.15 | [27] |

$^a$zinc oxide quantum dots (ZnO-Qd) applied on titanium dioxide ($TiO_2$) coating; entries 1, 2, 8, 9: indium tin oxide (ITO) glass counter electrode; entries 3-7, 10-24: fluorine-doped tin oxide (FTO) glass counter electrode

## 2. 2. Anthocyanins

Anthocyanins are polyphenolic water-soluble plant pigments that have been recognized as promising natural sensitizers for DSSCs application; furthermore, they are the most extensively investigated photosensitizers [11]. The resonant structure of the flavylium ion (Figure 2) plays a crucial role in determining the colour intensity of anthocyanins [11]. Aglycones of anthocyanins, anthocyanidins (Figure 2), are polyhydroxy and polymethoxy derivatives of flavylium salts [20,35]. A variety of anthocyanidins (Figure 2) are formed *via* hydroxylation of a flavylium cation backbone in various positions, typically on C3, C5, C6, C7, as well as C3', C4', and C5'; some hydroxyl groups may be further methylated (mainly at position 3' and 5') [11,35]. The basic chemical structure of anthocyanidins consists of an aromatic ring A fused with a pyrylium ring

C, which is further connected *via* a C-C bond to the second aromatic ring B [36]. Distinctive red to blue colour of flowers (tulips, roses and orchids), fruits (grapes, berries and apples), and vegetables (red cabbage and radishes) originate from high concentrations of water-soluble vacuolar pigments, known as anthocyanins [36].

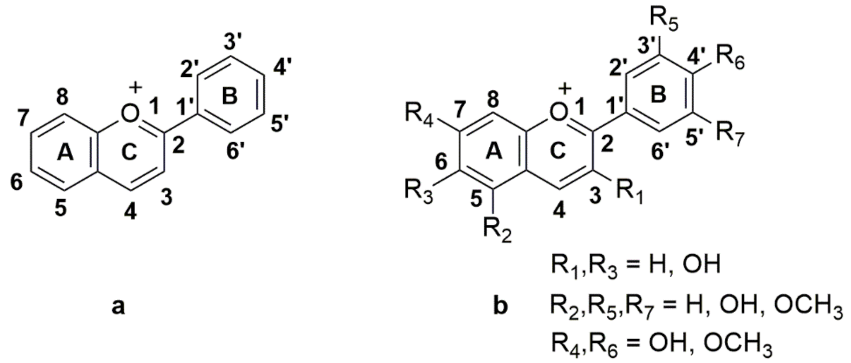

***Figure 2.*** *General structure of: flavylium cation (a), anthocyanidins (b)*

*O*-Glycosylation of this polyphenol aromatic structure, which results in formation of appropriate anthocyanins, could take place on various hydroxyl moieties, among which the position 3 (Figure 3) is the most frequent.

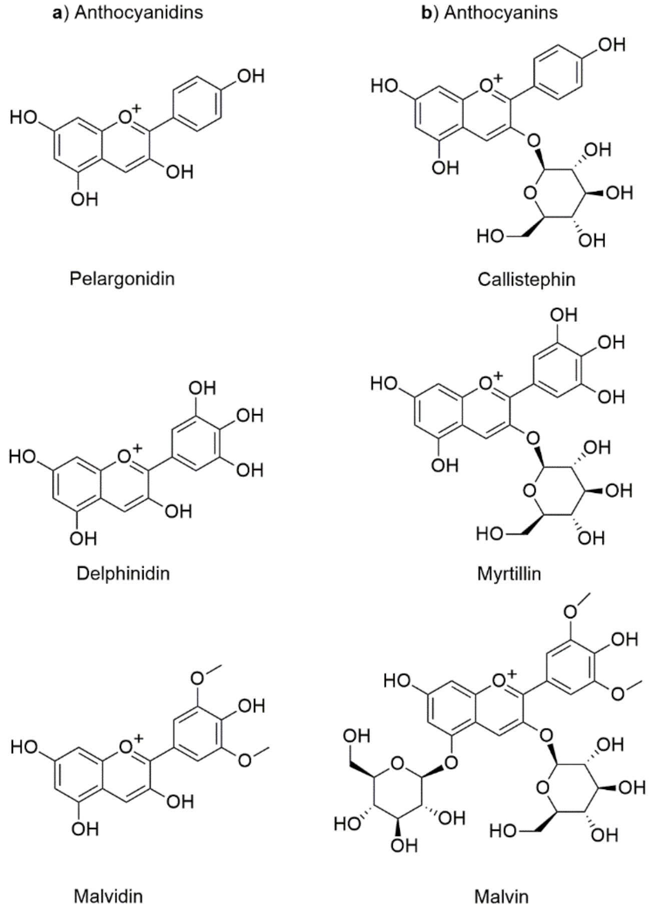

***Figure 3.*** *Chemical structure of some natural occurring anthocyanidins (a) and corresponding mono- or di-glycosides (anthocyanins) (b)*

In carbohydrate-conjugated forms of anthocyanidins, the sugar residue might be glucose, xylose, galactose, arabinose, rhamnose or rutinose [37]. Although there is an enormous diversity of anthocyanins found in nature, only six of their aglycones (anthocyanidins) are predominant in vascular plants, namely: cyanidin, delphinidin, pelargonidin, peonidin, petunidin, and malvidin (Figure 3) [11,35]. Anthocyanins, which are most often found in nature, are glycosidic derivatives of cyanidin, delphinidin, and pelargonidin. Their chemical stability/colour is highly affected by many factors including pH, storage temperature, concentration and chemical structure, oxygen, presence of enzymes (and other accompanying substances/metal ions), light and solvents [35,36].

Structural modifications of anthocyanins are correlated with changes in pH-values as follows (Figure 4) [35,36]:

1. at the pH 1, anthocyanins exist in the predominant equilibrium form of the red flavylium cation (A),
2. at a pH value in the range of 2–4, the blue quinonoidal species (B–D) are the most dominant,
3. at a pH value in the range of 5–6, a colourless carbinol pseudobase (E) and a chalcone (F), are the only two species that can be observed,
4. at a pH value greater than 7, anthocyanins are degraded, which is controlled by the substituent type.

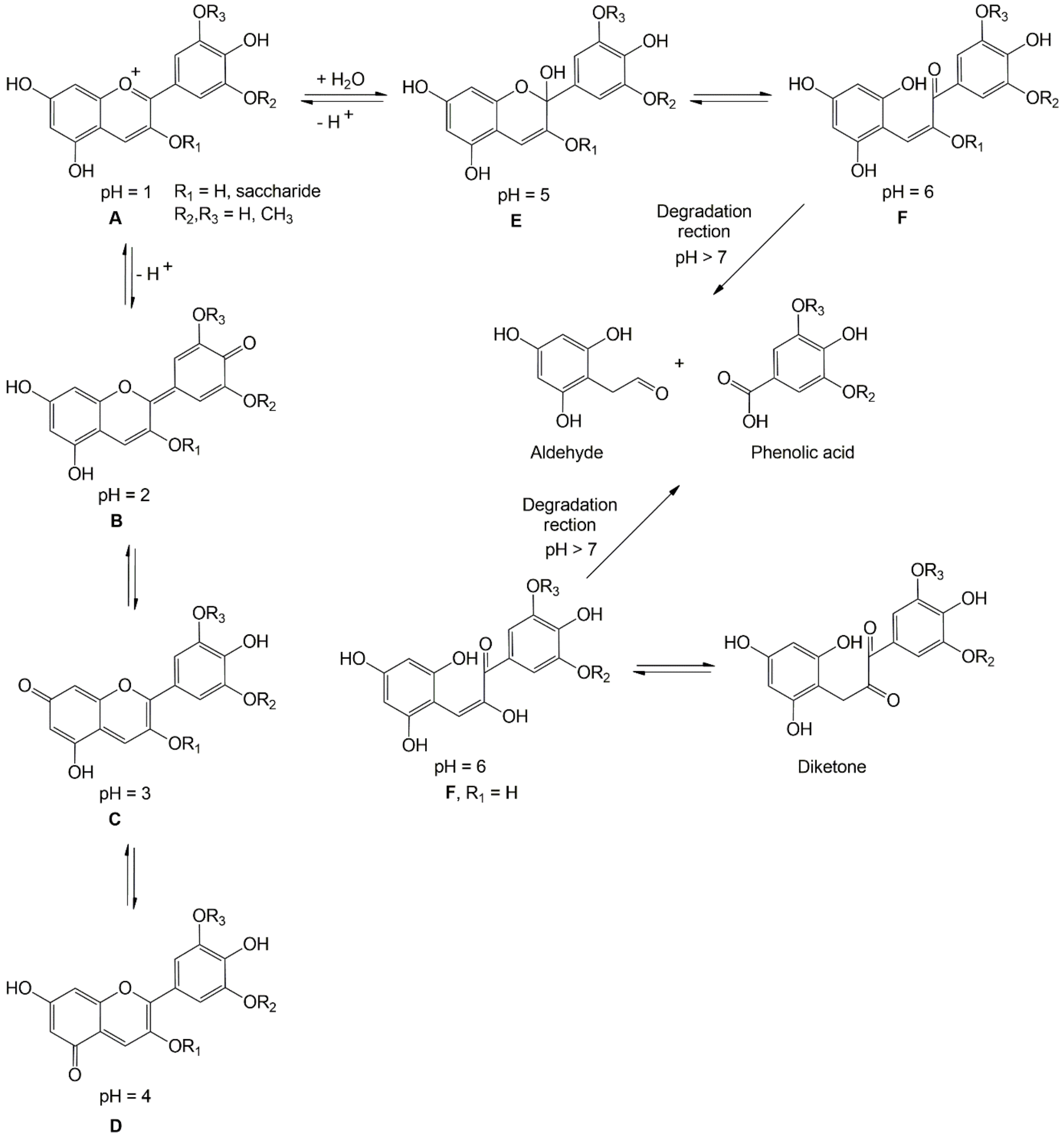

***Figure 4.*** *Chemical forms of anthocyanins depending on the pH and degradation reaction*

As can be concluded from Figure 4 (structures D, A and E), the equilibrium between qunoidal bases and carbinol takes place through the flavylium cation, which is the predominant species in more acidic conditions (*e.g.* at a pH value in the range of 4 to 6, four structural forms exist at the same time: the red flavylium cation, the anhydrous blue quinoidal base, the colourless carbinol pseudobase, and the pale yellow chalcone). In addition, the anthocyanins stability is controlled by the number of the hydroxyl/methoxy groups attached to the second aromatic ring B (Figure 2, structure b), because they decrease the aglycon stability in the neutral media [35,36].

One way to increase the stability of anthocyanins is to form co-pigments, systems rich in $\pi$-electrons and capable to interact with systems poor in $\pi$-electrons, like the flavylium cation. This inter/intramolecular interaction provides shielding of the flavylium cation (Figure 2) from the nucleophilic attack of the water molecule in position 2 and from peroxides and sulphur dioxide in position 4 [36]. Taking into account all the factors affecting the stability of anthocyanins, the best method for their extraction implies the use of acidified methanol or ethanol, at temperatures ranging from 20 to 50 °C, or the use of modern techniques including ultrasound-assisted extraction, microwave-assisted extraction, supercritical fluid extraction, and high-hydrostatic pressure extraction [11].

It was demonstrated in literature that a DSSC containing acidified anthocyanin extracted from *Syzygium cumini* achieved better performances compared to the original pigment previously utilized [38]. This is due to the interaction of light-harvesting pigment with concentrated hydrochloric acid which results in breaking-down of the flavylium cation *O*-glycosidic linkage and releasing the anthocyanidin. The optical analysis of the acidified anthocyanin indicates better delocalization of $\pi$-electrons within the pigment structure compared to the one not treated with acid and a smaller HOMO-LUMO energy gap [38]. Furthermore, a DSSC was constructed with a fill factor of 0.2 and overall efficiency of 1.33 % using an anthocyanin pigment extracted from *Eugenia claviflora*, and $TiO_2$/conjugated polymer poly(3,4-ethylenedioxythiophene):polystyrene sulfonate (PEDOT:PSS) as semiconductor [39]. Erande and coworkers fabricated and investigated efficiency of DSSCs with pomegranate dye (specifically anthocyanin) treated $TiO_2$ thin films. The higher power conversion efficiency was succeeded for DSSCs fabricated by using anthocyanin than that of bare $TiO_2$ ($\eta$ = 0.20 and 0.17 %, respectively) [40]. Photocatalytic activity of $TiO_2$ triggers degradation of natural pigments in DSSC, so Prabavathy and coworkers increased the anthocyanin performance by co-sensitizing it with astaxanthin isolated form *Haematococcus pluvialis* at the ratio 70:30. Fluorescence lifetime measurements indicated that astaxanthin reduces the degradation rate of anthocyanin without disturbing its band gap [41]. By employing anthocyanins isolated from *Canarium ovatum*, and $TiO_2$ nanoparticles accumulated on translucent ITO glass, Gasga and coworkers fabricated solar cells with the aim of determining the ideal $TiO_2$ film thickness and soaking time in dye. According to results obtained by using response surface methodology, the solar cells running at 55.249 µm $TiO_2$ film thickness and soaked for 12 h gave the photovoltaic performances as follows: $V_{oc}$ = 446 mV, $J_{sc}$ = 6.29 mA cm$^{-2}$, FF = 0.60 % and $\eta$ = 1.79 % [42]. The corresponding photovoltaic parameters of DSSCs sensitized with anthocyanins are shown in Table 3.

***Table 3.** Photovoltaic parameters of DSSCs sensitized with anthocyanins and with anthocyanin/carotenoid mixture*

| No. | Name of plant | Class/name of pigment | Semi-conductor | Counter electrode | Electrolyte | Photovoltaic parameters | | | | Ref. |
|---|---|---|---|---|---|---|---|---|---|---|
| | | | | | | $V_{oc}$ / mV | $J_{sc}$ / mA cm$^{-2}$ | FF, % | $\eta$ / % | |
| 1 | *Punica granatum* | Anthocyanin | $TiO_2$ | Pt paste coated on FTO glass | $I^-/I_3^-$ | 520 | 0.34 | 0.65 | 0.12 | [44] |
| 2 | *Punica granatum* | Anthocyanin | $TiO_2$ | FTO glass | $I^-/I_3^-$ | 500 | 0.73 | 0.59 | 2.58 | [27] |
| 3 | *Sorghum bicolor* | Anthocyanin | $TiO_2$ | ITO glass | $I^-/I_3^-$ | 340 | 1.69 | 0.31 | 0.18 | [28] |
| 4 | *Delonix regia* | Anthocyanin | $TiO_2$ | ITO glass | $I^-/I_3^-$ | 420 | 0.81 | 0.29 | 0.10 | [28] |
| 5 | *Syzygium cumini* | Anthocyanin | $TiO_2$ | Pt paste coated on FTO glass | $I^-/I_3^-$ | 200 | 1.29 | 26.1 | 0.27 | [38] |
| 6 | *Syzygium cumini*$^a$ | Anthocyanin | $TiO_2$ | Pt paste coated on FTO glass | $I^-/I^-_3$ | 370 | 2.76 | 33.7 | 1.39 | [38] |
| 7 | *Syzygium cumini* | Anthocyanin | $TiO_2$ NP/TiNT$^b$ | FTO glass | $I^-/I_3^-$ | 510 | 5.43 | 14.7 | 0.40 | [45] |
| 8 | *Trifolium pratense* | Anthocyanin | $TiO_2$ | FTO glass | $I^-/I_3^-$ | 0.58 | 0.34 | 0.75 | 0.15 | [29] |
| 9 | *Eugenia claviflora* | Anthocyanin | $TiO_2$/ conjugated polymer PEDOT:PSS$^c$ | ITO glass | $I^-/I_3^-$ | 430 | 0.12 | 0.20 | 1.33 | [39] |

| No. | Name of plant | Class/name of pigment | Semi-conductor | Counter electrode | Electrolyte | Photovoltaic parameters | | | | Ref. |
|---|---|---|---|---|---|---|---|---|---|---|
| | | | | | | $V_{oc}$ / mV | $J_{sc}$ / mA cm$^{-2}$ | FF, % | $\eta$ / % | |
| 10 | *Punica granatum* | Anthocyanin | $TiO_2$ | ITO glass | $KI/I_2/EG$ | 304 | 1.62 | 0.21 | 0.20 | [40] |
| 11 | *Zea mays* | Anthocyanin | $TiO_2$ | Pt paste coated on FTO glass | $TBAI/I_2$[d] | 586 | 0.88 | 0.59 | 0.31 | [43] |
| 12 | *Brassica oleracea* | Anthocyanin | $TiO_2$ | FTO glass | $I^-/I_3^-$ | 461 | 0.97 | 0.28 | 0.13 | [33] |
| 13 | Rose / *H. pluvialis* | Anthocyanin: Astaxanthin = 70:30[e] | $TiO_2$ | FTO glass | $I^-/I_3^-$ | 740 | 8.6 | 0.70 | 2.82 | [41] |
| 14 | *Canarium ovatum* | Anthocyanin | $TiO_2$ | ITO glass | $I^-/I_3^-$ | 446 | 6.29 | 0.60 | 1.79 | [42] |
| 15 | *Tropaeolum majus* | Anthocyanin and Carotenoid | $TiO_2$ | Pt paste coated on FTOglass | $I^-/I_3^-$ | 502 | 0.70 | 0.62 | 0.22 | [46] |

[a]acidified extract; [b]composite of $TiO_2$ nanoparticle/$TiO_2$ nanotube paste; [c]poly(3,4-ethylenedioxythiophene):polystyrene sulfonate; [d]0.6 M of tetra-*n*-butylammonium iodide and 0.05 M of iodine in acetonitrile; [e]volume ratio

### 2. 3. Carotenoids

Research on carotenoids began with the isolation of an apocarotenoid from the crocin family (now known as crocetin) from saffron a little more than 200 years ago [47]. Later, a carrot pigment, carotene (today known as β-carotene), was isolated from carrot-juice [47,48]. In the 1930s, C40 structure of β-carotene and lycopene was described (Figure 5). Carotenoids, mostly 40-carbon skeleton isoprenoid natural pigments that can be synthesized by plants and microorganisms a la photosynthetic bacteria, fungi and algae, are responsible for the red, orange, and yellow colours of flowers, fruits, and vegetables. Together with chlorophylls, they are irreplaceable pigments in photosynthetic organs [49,50]. Even though there are several hundreds of naturally occurring carotenoids, only 50 of them have noteworthy pharmacological and industrial significance, particularly due to their provitamin A activity, antioxidant properties, potential as protective agents, and use as natural dyes [47,48,51].

According to the number of C atoms in their chemical structure, carotenoids can be divided into C30, C40, C45 and C50 carotenoids, while naturally most frequent are tetraterpene carotenoids (C40 compounds) with eight isoprene units [47]. Originally, they are mostly present as all-E geometric forms that undergo E/Z-isomerization [49,50]. Naturally occurring carotenoids can be primary classified as carotenes and xanthopylls. Carotenes consist of linear hydrocarbon chains, which can be cyclized at one/both ends, while xanthopylls represent the oxygenated derivatives of carotenes containing different functional groups such as hydroxyl, epoxy or keto (Figure 5) [47-49]. Some chemical modifications of carotenoids exist in nature. In addition to their free form, xanthopylls are also present in the form of fatty acid esters, glycosides, sulphates and complexes with proteins [47,49]. Allene and acetylene carotenoid structures are also examples of naturally occurring, chemically modified carotenoids [47,52].

In microorganisms and plants, tetraterpene carotenoids (C40 compounds) are the object of enzymatic (in the presence of carotenoid cleavage dioxygenases (CCDs) enzymes) and non-enzymatic (*via* singlet oxygen attack) oxidative cleavage resulting in wide variety of carotenoid-derived compounds called apocarotenoids [47,53,54]. For instance, biosynthesis of apocarotenoid bixin begins with the enzymatic oxidative cleavage of its precursor, lycopene, which produces bixin aldehyde that undergoes oxidation giving norbixin. Finally, bixin is formed by methylation of norbixin [53,55]. Both oxidation of bixin aldehyde and methylation of norbixin are also taking place in the presence of enzymes (dehydrogenase and methyltransferase, respectively).

There is a great interest in carotenoids as natural sensitizers for application in DSSCs due to their light-harvesting and photoprotecting function in plants [56]. Considering all-*E* long conjugated C=C system in carotenoid molecules, they absorb in the blue-green region of the electromagnetic spectrum. Orange-red pigments from apocarotenoid pigment group, bixin and norbixin, are promising natural dye photosensitizers for DSSCs application as well [57].

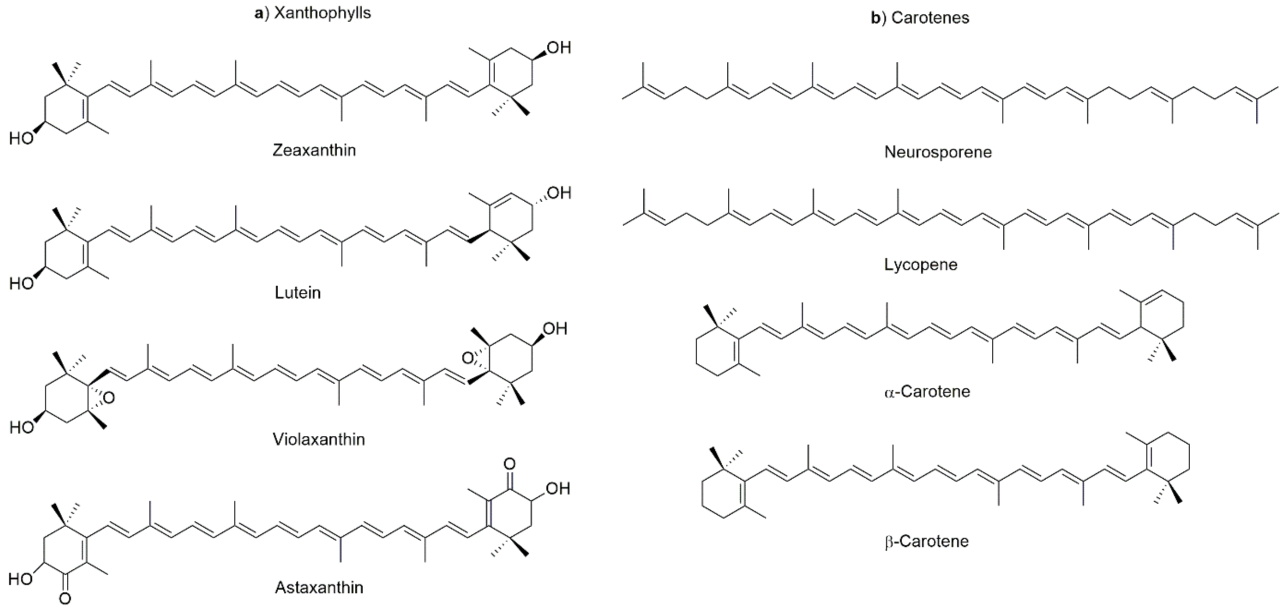

***Figure 5.*** *Carotenoid structure: a) Xanthophylls: zeaxanthin, lutein, violaxanthin and astaxanthin; b) Carotenes: neurosporene, lycopene, α-carotene and β-carotene*

DSSCs assembled with two apocarotenoids indicated that the photocurrent conversion efficiency of norbixin ($\eta$ = 0.28 %) is twice as high as that of bixin sensitized cells ($\eta$ = 0.12 %). It was shown that the semiconductor $TiO_2$ can act as a catalyst for photodegradation process with a common mechanism with the formation of apocar radical cation [56]. DSSCs were also investigated using *Rauvolfia vomitoria* fruit extract rich in carotenoids as natural sensitizer of a $TiO_2$ thin film. Namely, a DSSC with 10 µm $TiO_2$ film exhibited the best performances: $V_{oc}$ = 650 mV, $J_{sc}$ = 0.10 mA cm$^{-2}$, FF = 0.65 % and $\eta$ = 0.05 %. The short-circuit current density value increased directly with increasing the thickness of the $TiO_2$ film in the range of 5–10 nm which could be explained by the fact that a thicker electrode can absorb more photons, leading to a higher $J_{sc}$ [58]. Relevant photovoltaic parameters of DSSCs sensitized with carotenoids and apocarotenoids are shown in Table 4.

***Table 4.****Photovoltaic parameters of DSSCs sensitized with carotenoids and apocarotenoids*

| No. | Name of plant | Class/name of pigment | Semi-conductor | Counter electrode | Electrolyte | Photovoltaic parameters | | | | Ref. |
|---|---|---|---|---|---|---|---|---|---|---|
| | | | | | | $V_{oc}$ / mV | $J_{sc}$ / mA cm$^{-2}$ | FF, % | $\eta$ / % | |
| 1 | *Bixa orellana* | Bixin and Norbixin | $TiO_2$ | ITO glass | $I^-/I_3^-$ | 350 | 1.28 | 0.35 | 0.16 | [28] |
| 2 | *Tabebuia rosea* | Carotenoid | $TiO_2$ | ITO glass | $I^-/I_3^-$ | 320 | 0.88 | 0.36 | 0.10 | [28] |
| 3 | *Rauvolfia vomitoria* | Carotenoid | $TiO_2$ | FTO glass | $I^-/I_3^-$ | 650 | 0.10 | 0.65 | 0.05 | [58] |
| 4 | *Bixa orellana* | Bixin | $TiO_2$ | Pt/$TiO_2$ glass | $I^-/I_3^-$ | 410 | 0.65 | 46.7 | 0.12 | [56] |
| 5 | *Bixa orellana* | Bixin | $TiO_2$ | Pt paste coated on FTO glass | TBAI/$I_2$ | 600 | 0.99 | 0.61 | 0.36 | [43] |
| 6 | *Bixa orellana* | Bixin and Norbixin | $TiO_2$ NP/TiNT | FTO glass | $I^-/I_3^-$ | 630 | 6.19 | 18.9 | 0.74 | [45] |
| 7 | *Bixa orellana* | Norbixin | $TiO_2$ | Pt/$TiO_2$ glass | $I^-/I_3^-$ | 500 | 1.13 | 48.6 | 0.28 | [56] |
| 8 | *Tagetes* | Lutein | $TiO_2$ | FTO glass | $I^-/I_3^-$ | 460 | 0.06 | 0.46 | 0.15 | [27] |

## 2. 4. Betalains

The best known pigments among betalains, betanin and indicaxanthin, were isolated and identified in the early 1960s. Indicaxanthin is a betaxanthin pigment from yellow-orange cactus pear (*Opuntia ficus-indica*), while betanin is a betacyanin pigment that is primarily responsible for the deep red colour of beet (*Beta vulgaris*) [59]. Betalains are natural hydrophilic, nitrogen-containing, Tyr-derived pigments, most frequently accumulated in epidermal/subepidermal tissues of herbs belonging to the order *Caryophyllales* (red beet roots, graining/leafy amaranth, and coloured Swiss chard), and subfamilies of higher fungi including agaric *Amanita muscaria*, *Hydrocybe,* and *Hydrophorus* [60,61]. Even though betalains and anthocyanins differ both in their chemical structure and the biosynthetic pathway, they seem to have similar functions. Considering that those two pigments have never been found together in the same plant, it seems that they cannot exist together [60,61]. This is confirmed by the original name of betalain subgroups namely, betacyanins, which were labelled as "nitrogenous anthocyanins", while the betaxanthins were labelled as flavonoids (Figure 6) [61]. Red beet containing roughly 75 to 95 % of betacyanins and 5 to 25 % of betaxanthins has been continually treated as the exclusive source of the betalains. The basic structure of all betalains is betalamic acid [4-(2-oxoethylidene)-1,2,3,4-tetrahydropyridine-2,6-dicarboxylic acid], which condensed with *cyclo*-DOPA [cyclo-L-(3,4-dihydroxyohenylalanine)] or its glycosyl derivatives builds red-violet betacyanins; hence, when condensed with various amino acids or amines, builds the yellow-orange immonium condensation products betaxanthins [61].

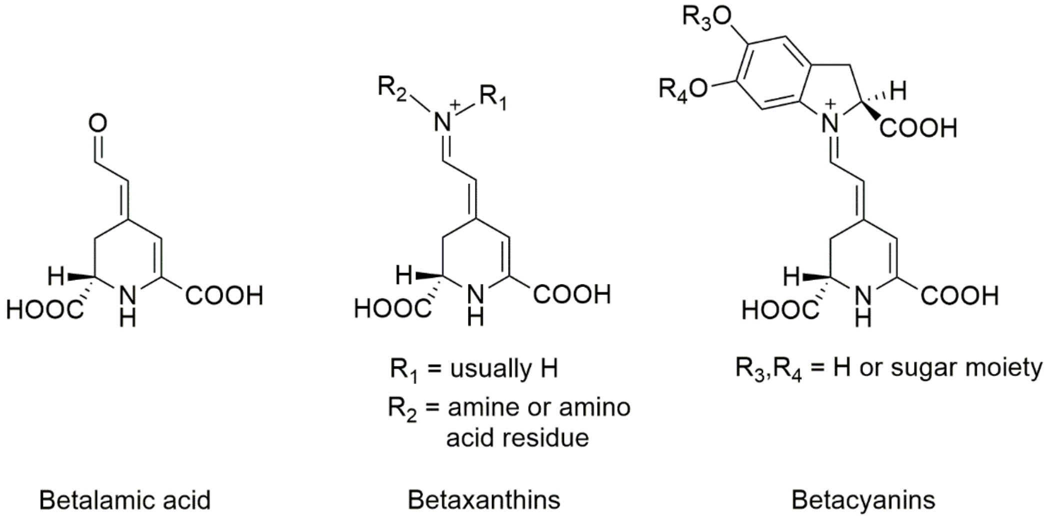

***Figure 6**. Structure of betalamic acid, betaxanthins and betacyanins*

Generally speaking, the absorption properties of betalains are affected by both structural modifications/substituent effects and changing the acid-basic properties of the solvent used [60,62]. Owing to a strongly conjugated 1,7-diazaheptamethine system, betalamic acid-derived moiety is the key chromophore of all betalains [60,63]. The visible region of absorption maximum for betaxanthins is between 460 and 475 nm, while betacyanins exhibit a shift of the absorbance maximum from 480 to 540 nm as a result of extended resonance (interaction of conjugated double bonds of 1,7-diazaheptamethine system and aromatic ring of *cyclo*-DOPA) [63]. The second absorption maximum for betacyanins is in the UV region in the range of 270 to 280 nm due to *cyclo*-DOPA [61,62]. To provide the greatest stability of these hydrophilic pigments, the best method for their extraction represents the employment of water or 20 to 50 % methanol/ethanol solutions [62].

In addition to their charming colours, antioxidant activity and other biological properties such as anticancer, anti-inflammatory, chemopreventive *etc*., betalain pigments have attracted the attention with their potential as natural sensitizers in DSSCs due to their 1,7-diazaheptametine substructure [59,63].

Bharathi Devi and coworkers explored effects of microwave annealing on the performance of a DSSC assembled using betacyanins and betaxanthins extracted from *Beta vu*lgaris. It was observed that the efficiency of microwave annealed DSSCs is much lower ($\eta$ = 0.16 to 0.29 % depending on the irradiation time) than that of the conventionally annealed ones ($\eta$ = 1.11 %) due to inefficient light scattering efficiency [64]. Analysis of the optical properties of a DSSC fabricated using betalain isolated from *Beta vulgari*s as a sensitizer, C, N, S co-doped $TiO_2$ (TU-$TiO_2$) as a semiconductor, and 75 % molar concentration of thiourea doped into $TiO_2$ nanoparticles, indicated a relative increase in the efficiency for 94 % and a decrease in the band gap making the solar cell more perceptive to visible light [65]. Table 5 shows the corresponding photovoltaic parameters of DSSCs sensitized with betalains.

***Table 5.****Photovoltaic parameters of DSSCs sensitized with betalains*

| No. | Name of plant | Class/name of pigment | Semi-conductor | Counter electrode | Electrolyte | Photovoltaic parameters | | | | Ref. |
|---|---|---|---|---|---|---|---|---|---|---|
| | | | | | | $V_{oc}$ / mV | $J_{sc}$ / mA cm$^{-2}$ | FF, % | $\eta$ / % | |
| 1 | *Mirabilis jalapa* | Betalain | $TiO_2$ | FTO glass | $I^-/I_3^-$ | 0.46 | 0.16 | 0.72 | 0.05 | [29] |
| 2 | *Beta vulgaris* | Betalain | $TiO_2$ | FTO glass | $I^-/I_3^-$ | 370 | 0.76 | 0.39 | 0.11 | [33] |
| 3 | *Beta vulgaris* | Betalain | C,N,S co-doped $TiO_2$-(TU0.75)[a] | FTO glass | $I^-/I_3^-$ | 350 | 0.42 | 0.61 | 0.36 | [65] |
| 4 | *Bougainvillea* | Betacyanin | Nano-$TiO_2$ | FTO glass | NaI/$I_2$ | 132 | 15.22 | 0.20 | 0.40 | [24] |
| 5 | *Bougainvillea* | Betacyanin | Nano-$TiO_2$ | FTO glass | KI/$I_2$ | 405 | 3.91 | 0.27 | 0.42 | [24] |
| 6 | *Beta vulgaris* | Betacyanin and Betaxanthin (conventional extraction) | $TiO_2$ | FTO glass | KI/$I_2$/EG | 310 | 7.47 | 0.48 | 1.11 | [64] |
| 7 | *Beta vulgaris* | Betacyanin and Betaxanthin (5 min MW extraction) | $TiO_2$ | FTO glass | KI/$I_2$/EG | 150 | 1.59 | 0.66 | 0.16 | [64] |

[a] carbon-nitrogen-sulphur (C-N-S) co-doped titanium dioxide ($TiO_2$) nanoparticles containing 75 % of thiourea

## 2. 5. Chlorophyll

Energy for plant growth and further development is provided by natural complex green pigment molecules accumulated in plants, algae and some bacteria, known as chlorophylls (Chls) [66-68]. In 1818 Pelletier and Caventou [69] isolated Chls for the first time and coined this term meaning "green leaf" (translation from Greek). Three Nobel prizes were conferred to Willstätter R. in 1915 [70], Fischer H. in 1930 [71] and Woodward R. in 1965 [72], for their scientific contributions in elucidating the structure and chemical synthesis of Chls. There are five major chlorophyll (Chl) pigments (Chl *a, b, c,* d and *f*), varying mutually by a type of side chains linked to the tetrapyrrole moiety on the chlorin/porphyrin ring [67,68]. Chlorophylls *a* and *b* (Figure 7) are the key components of the photosynthetic systems in land plants and green algae. While Chl *b* is an antenna chlorophyll, Chl *a* is crucial in photochemistry and has a role both in light-harvesting and energy conversion [67,73].

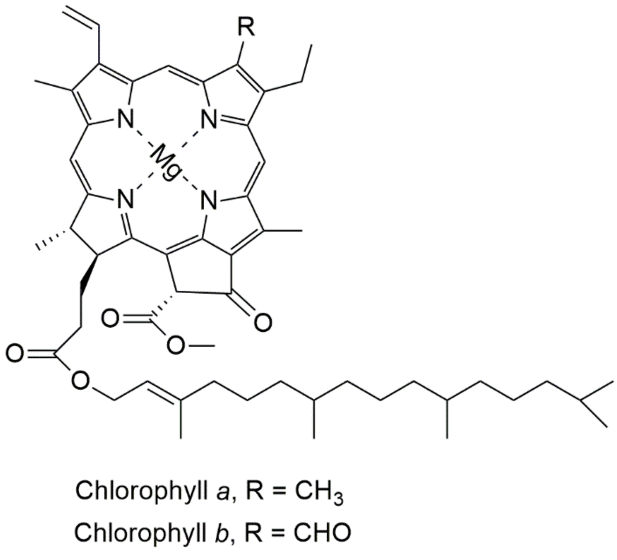

***Figure 7.*** *Structure of natural chlorophylls: chlorophyll a and chlorophyll b*

Due to strongly conjugated tetrapyrrole moiety, Chls are capable to absorb light in the visible range. Chl *a* mostly exhibits visible light absorption in the red-orange region, while Chl *b* mostly absorbs in the blue-purple region of the electromagnetic spectrum [66]; poor absorption in the green spectral region is typical for both. Green appearance of Chls is due to their absorption features [67]. Natural Chls (Chl *a* and *b*) and Zn- or Cu-Chl derivatives (*i.e.* Zn- or Cu-chlorophyllins, pheophytins, pyropheophytins) are antioxidant, antimutagenic, antigenotoxic, anticancer, chemoprotective, and antiobesogenic compounds with potential applications in medicine [67,68]. Chls and Chl-derivatives (various chlorophyllins) are in use as authorized food colorants E140 and E141 (food codes in the EU) [67,74]. Considering their advantageous light absorption properties, Chl pigments have the potential to serve as natural photosensitizers for DSSCs [75].

By using nanocomposite ZnO:$TiO_2$ (weight ratio 1:3) as a semiconductor material, and Chl extracted from broccoli, as a light-harvesting pigment, a DSSC was constructed with the efficiency of 0.171 % [76]. On the other hand, while using the same nanocomposite material, and the same natural pigment extracted from *Brassica rapa*, in another study a DSSC was produced exhibiting a slightly higher efficiency of 0.21 % [77]. When comparing the photovoltaic performances of DSSCs containing Chl and Chl:betalain mixture (volume ratio 1:1) as natural sensitizers, and the tetragonal $TiO_2$ nanoparticles as semiconductor, it was concluded that, cosenzitation of light-harvesting pigments produces 5.5 times greater solar cell efficiency relative to a plain chlorophyll [78]. In this frame, Mensah-Darkwa and coworkers demonstrated that an increase in the efficiency of a DSSC based on a double-layer $TiO_2$/graphite oxide (GO) photoanodes compared to the one with a single-layer pristine $TiO_2$ photoanodes, might be a consequence of the rising GO content [78,79]. Siregar and coworkers investigated the significance of the annealing temperature of Mg-doped ZnO photoanode, of the manufactured DSSC containing natural light-harvesting pigment extracted from *Rhodomyrtus tomentosa*, which exhibits a strong absorption band at 610 nm. The maximum efficiency of $\eta$ = 3.53 % was obtained in a DSSC with Mg-ZnO photoanode annealed at 500 °C [80]. When absorbed on $TiO_2$ nanoparticles, the absorption band of turmeric dye (containing up to 3 % curcumin as the active ingredient) is shifted to higher energy in the visible region. The broad absorption range indicates that the dye is effectively absorbed onto the $TiO_2$ nanoparticles, enabling it to harvest solar energy from a broader spectral range, which ultimately leads to a higher photocurrent. The overall efficiency $\eta$ = 0.22 % was reached in a DSSC fabricated using turmeric dye [45]. Results of combined atomic force microscopy and photoluminescence analyses indicated that *Curcuma longa* dye thin films with a non-uniform granular structure absorbed in the range of 400 to 500 nm. The photoelectrochemical parameters determined by the finite element method simulation of a DSSC such us the short circuit current, the open-circuit voltage, and the fill factor were 0.13 mA cm$^{-2}$, 0.52 mV, and 0.83 %, respectively. The simulated DSSC based on *Curcuma longa* dye exhibited an efficiency about 0.86 % [81]. The corresponding photovoltaic parameters of DSSCs sensitized with Chls and other pigments are shown in Table 6.

***Table 6.****Photovoltaic parameters of DSSCs sensitized with Chl and other pigments*

| No. | Name of plant | Class/name of pigment | Semi-conductor | Counter electrode | Electrolyte | Photovoltaic parameters | | | | Ref. |
|---|---|---|---|---|---|---|---|---|---|---|
| | | | | | | $V_{oc}$ / mV | $J_{sc}$ / mA cm$^{-2}$ | FF, % | $H$ / % | |
| 1 | *Tridax procumbens* | Chlorophyll | $TiO_2$ | FTO glass | $I_2$/KI-lugol solution | 170 | 0.31 | 0.40 | 0.02 | [78] |
| 2 | *Tridax procumbens / Beta vulgaris* | Chlorophyll : Betalain = 1:1[a] | $TiO_2$ | FTO glass | $I_2$/KI-lugol solution | 270 | 1.16 | 0.34 | 0.11 | [78] |
| 3 | *Brassia oleraea var. italica* | Chlorophyll | Nano-composite ZnO/$TiO_2$ (1:3) | FTO glass | $I^-/I_3^-$ | 0.55 | / | / | 0.17 | [76] |
| 4 | *Mimosa pudica* | Chlorophyll | DL-0.71 wt.% GO[b] | Graphite | $I^-/I_3^-$ | 284 | 0.016 | 0.035 | 0.1 | [79] |
| 5 | *Malva verticillata* | Chlorophyll | $TiO_2$ | Pt paste coated on FTO glass | $I^-/I_3^-$ | 540 | 1.42 | 55.4 | 1.70 | [38] |
| 6 | *Brassica rapa* | Chlorophyll | Nano-composite ZnO/$TiO_2$ (1:1) | | PEO:KI/$I_2$ | 0.333 | / | / | 0.076 | [77] |
| 7 | *Brassica rapa* | Chlorophyll | Nano-composite ZnO/$TiO_2$ (1:2) | | PEO:KI/$I_2$ | 0.546 | / | / | 0.194 | [77] |
| 8 | *Brassica rapa* | Chlorophyll | Nano-composite ZnO/$TiO_2$ (1:3) | | PEO:KI/$I_2$ | 0.500 | / | / | 0.210 | [77] |
| 9 | *Bassiasco paria* | Chlorophyll | $TiO_2$ | FTO glass | $I^-/I_3^-$ | 0.58 | 0.42 | 0.76 | 0.18 | [29] |
| 10 | *Curcuma longa* | Curcumin | $TiO_2$ NP / TiNT | FTO glass | $I^-/I_3^-$ | 620 | 4.59 | 7.99 | 0.22 | [45] |
| 11 | *Rubia tinctorum* | Anthraquinone | $TiO_2$ | FTO glass | $I^-/I_3^-$ | 330 | 0.03 | 0.36 | 0.05 | [27] |

[a]volume ratio; [b]doublelayer photoanode with 0.71 wt.% graphene oxide

## 3. CONCLUSION

This review outlines various materials used in manufacturing DSSCs including semiconductor nanoparticles, types of electrolytes and types of counter electrodes. A special emphasis is placed on the selection of light-harvesting pigments as the DSSC part responsible for achieving high photovoltaic performances. Effects of the chemical structure of the pigment, particularly the anchoring groups, on the photovoltaic performance are also discussed together with the mechanism of their chemisorption onto the semiconductor.

In addition to beneficial environmental effects, the favourable physico-chemical properties together with affordability and sustainability make natural pigments promising candidates for advancing the DSSC technology. On the other hand, low efficiency and low stability still prevent their application at a larger scale. Regardless of the class they belong to, natural pigments do not achieve efficiencies greater than 3 %, either used alone or in a mixture. Hence, their future application, which would provide photovoltaic performance similar to that achieved by applying synthetic dyes, requires a concerted effort in terms of various optimizations of all DSSC components.

***Acknowledgements:*** This work was supported by the Ministry of Science, Technological Development and Innovation of the Republic of Serbia (Contract No. 451-03-136/2025-03/200135 and 451-03-136/2025-03/200287).

## REFERENCES

[1] Yahya M, Bouziani A, Ocak C, Seferoğlu Z, Sillanpää M. Organic/metal-organic photosensitizers for dye-sensitized solar cells (DSSC): Recent developments, new trends, and future perceptions. *Dyes Pigments.* 2021; 192: 109227. https://doi.org/10.1016/j.dyepig.2021.109227

[2] Bist A, Chatterjee S. Review on Efficiency Enhancement Using Natural Extract Mediated Dye-Sensitized Solar Cell for Sustainable Photovoltaics. *Energy Technol.*2021; 9(8):2001058. https://doi.org/10.1002/ente.202001058

[3] Sharma K, Sharma V, Sharma S. Dye-Sensitized Solar Cells: Fundamentals and Current Status.*Nanoscale Res Lett.* 2018; 13: 381. https://doi.org/10.1186/s11671-018-2760-6

[4] Pastuszak J, Węgierek P. Photovoltaic cell generations and current research directions for their development. *Materials.* 2022; 15: 5542. https://dx.doi.org/10.3390/ma15165542

[5] Luceño-Sánchez JA, Díez-Pascual AM,Peña Capilla R. Materials for Photovoltaics: State of Art and Recent Developments. *Int J Mol Sci.* 2019; 20: 976. https://dx.doi.org/10.3390/ijms20040976

[6] Dambhare MV, Butey B, Moharil SV. Solar photovoltaic technology: A review of different types of solar cells and its future trends. *J Phys: Conf Ser.* 2021; 1913: 012053. https://dx.doi.org/10.1088/1742-6596/1913/1/012053

[7] Shalini S, Balasundara Prabhu R, Prasanna S, Mallick TK, Senthilarasu S. Review on natural dye sensitized solar cells: Operation, materials and methods. *Renew Sustain Energy Rev.* 2015; 51(C): 1306-1325. https://doi.org/10.1016/j.rser.2015.07.052

[8] Cherepy NJ, Smestad GP, Gratzel M, Zhang JZ. Ultrafast electron injection: implications for a photo electrochemical cell utilizing an anthocyanin dyesensitized TiO2 nanocrystalline electrode. *J Phys Chem B.* 1997; 101(45): 9342-9351. https://doi.org/10.1021/jp972197w

[9] Olea A, Ponce G, Sebastian PJ. Electron transfer via organic dyes for solar conversion. *J Sol Energy Mater Sol Cells.* 1997; 59: 137-143. https://doi.org/10.1016/S0927-0248(99)00038-0

[10] Garcia CG, Polo AS, Iha NYM. Fruit extracts and ruthenium polypyridinic dyes for sensitization of TiO2 in photo electrochemical solar cells. *J Photochem Photobiol.* 2003; 160: 87-91. https://doi.org/10.1016/S1010-6030(03)00225-9

[11] Amogne NY, Ayele DW, Tsigie YA. Recent advances in anthocyanin dyes extracted from plants for dye sensitized solar cell. *Mater Renew Sustain Energy.* 2020;9: 23. https://doi.org/10.1007/s40243-020-00183-5

[12] Mehmood U, Rahman S, Harrabi K, Hussein IA, Reddy BVS. Recent advances in dye sensitized solar cells. *Adv Mater Sci Eng.* 2014: 974782. http://dx.doi.org/10.1155/2014/974782

[13] Mahajan U, Prajapat K, Dhonde M, Sahu K, Shirage PM. Natural dyes for dye-sensitized solar cells (DSSCs): An overview of extraction, characterization and performance. *Nano-Struct Nano-Objects*. 2024; 37: 101111. https://doi.org/10.1016/j.nanoso.2024.101111

[14] Prajapat K, Mahajan U, Sahu K, Dhonde M, Shirage PM. The evolution of natural dye-sensitized solar cells: Current advances and future outlook. *Sol Energy*. 2024; 284: 113081. https://doi.org/10.1016/j.solener.2024.113081

[15] Malhotra SS, Ahmed M, Gupta MK, Ansari. Metal-free and natural dye-sensitized solar cells: recent advancements and future perspectives. *Sustain Energ Fuels.* 2024; 8: 4127. https://doi.org/10.1039/D4SE00406J

[16] Kumar S, Pandey AK. Chemistry and biological activities of flavonoids: An overview. *Sci World J.*2013; 2013: 162750. http://dx.doi.org/10.1155/2013/162750

[17] Dias MC, Pinto DCGA, Silva AMS. Plant flavonoids: Chemical characteristics and biological activity. *Molecules.* 2021;26: 5377. https://doi.org/10.3390/molecules26175377

[18] Bone K, Mills S. *Principles and practice of phytotherapy: modern herbal medicine.* 2nd ed., Elsevier Ltd.; 2013. ISBN: 978-0-443-06992-5

[19] Šamec D, Karalija E, Šola I, Vujčić Bok V, Salopek-Sondi B. The Role of Polyphenols in Abiotic Stress Response: The Influence of Molecular Structure. *Plants.* 2021; 10: 118. https://doi.org/10.3390/plants10010118

[20] Corradini E, Foglia P, Giansanti P, Gubbiotti R, Samperi R, Laganà A. Flavonoids: Chemical properties and analytical methodologies of identification and quantitation in foods and plants. *Nat Prod Res.* 2011; 25(5): 469-495. http://dx.doi.org/10.1080/14786419.2010.482054

[21] Roy A, Khan A, Alghamdi S, Rajab BS, Babalghith AO, Alshahrani MY, Islam S, Islam MdR. Flavonoids a bioactive compound from medicinal plants and its therapeutic applications. *Bio Med Res Int.* 2022; 2022: 5445291. https://doi.org/10.1155/2022/5445291

[22] DuToit K, Drewes SE, Bodenstein J. The chemical structures, plant origins, ethnobotany and biological activities of homoisoflavanones. *Nat Prod Res.* 2010; 24(2): 457-490. https://doi.org/10.1080/14786410903335174

[23] Castelli MV, López SN. Homoisoflavonoids: Occurrence, Biosynthesis, and Biological Activity. In: Rahman A, eds. Studies in Natural Products Chemistry. Vol. 54. Elsevier; 2017: 315-354. https://doi.org/10.1016/B978-0-444-63929-5.00009-7

[24] Devi M, Saini RK, Shrivastava S. Photovoltaic analysis of fabricated dsscs based on natural colorants. *Rasayan J Chem.* 2021; 14(2): 1175-1182. http://dx.doi.org/10.31788/RJC.2021.1426149

[25] Surana K, Bhattacharya B, Majumder S. Extraction of yellow fluorescent Caesalpinia sappan L. dye for photovoltaic application. *Opt Mater (Amst)*. 2021; 119: 111347. https://doi.org/10.1016/j.optmat.2021.111347

[26] Błaszczyk A, Joachimiak-Lechman K, Sady S, Tański T, Szindler M, Drygała A. Environmental performance of dye-sensitized solar cells based on natural dyes. *Sol Energy.*2021; 215: 346-355. https://doi.org/10.1016/j.solener.2020.12.040

[27] John Peter I, Vijaya S, Anandan S, Ramachandran K, Nithiananthi P. Alternative low-cost photon sensitizer for dye-sensitized solar cells using less explored natural fabric dyes. *Int J Energy Res.* 2021; 45: 7764-7782. https://doi.org/10.1002/er.6360

[28] Djibrilla M, Sanda A, Badu M, Awudza JAM, Boadi N. Development of $TiO_2$-based dye-sensitized solar cells using natural dyes extracted from some plant-based materials nanocrystal synthesis view project dye-sensitized solar cells.*Chem Int*.2021; 7(1): 9-20. https://doi.org/10.5281/zenodo.4018012

[29] Ayaz M, Kasi JK, Kasi AK, Bokhari M, Sohail M, Ullah S. Natural plant *trifolium pratense*, *mirabilis jalapa* and *bassia scoparia* extract used as photosensitizer in dye-sensitized solar cell. *Iran J Chem Chem Eng.* 2021; 40(3): 872-880. https://doi.org/10.30492/ijcce.2020.38359

[30] Nasyori A, Noor FA. The Effects of the Concentration of Red and Yellow Gambier Fruit Dyes on the Short-Circuit Photocurrent in Dye-Sensitised Solar Cells. *J Phys Conf Ser.* 2021; 1811: 012067. https://doi.org/10.1088/1742-6596/1811/1/012067

[31] Senthamarai R, Madurai Ramakrishnan V, Palanisamy B, Kulandhaivel S. Synthesis of $TiO_2$ nanostructures by green approach as photoanodes for dye-sensitized solar cells. *Int J Energy Res.* 2021; 45: 3089-3096. https://doi.org/10.1002/er.6002

[32] Bharathi Devi S, Prakash Babu D, Naresh Kumar S, Ponkumar S. Microwave radiation induced performance modifications of dye-sensitized solar cells. *Radiat Eff Defects Solids.* 2021; 176(8): 481-492. https://doi.org/10.1080/10420150.2021.1871734

[33] Ben Karoui M, Saadaoui S, Torchani A, Gharbi R. Effect of Natural Sensitizers Anchoring to Nanoporous $TiO_2$ on Performance of Dye-Sensitized Solar Cells. *J Electron Mater.* 2021; 50: 4797-4805. https://doi.org/10.1007/s11664-021-09010-7

[34] Peymannia M, Gharanjig K, Arabi AM. Effect of zinc oxide quantum dots on the photovoltaic properties of natural dye-sensitized solar cells. *Int J Energy Res.* 2021; 45: 4170-4183. https://doi.org/10.1002/er.6082

[35] Mattioli R, Francioso A, Mosca L, Silva P. Anthocyanins: A Comprehensive Review of Their Chemical Properties and Health Effects on Cardiovascular and Neurodegenerative Diseases. *Molecules.* 2020; 25(17): 3809. https://doi.org/10.3390/molecules25173809

[36] Castañeda-Ovando A, Pacheco-Hernández M de L, Páez-Hernández ME, Rodríguez JA, Galán-Vidal CA. Chemical studies of anthocyanins: A review. *Food Chem*. 2009; 113: 859-871. https://dx.doi.org/10.1016/j.foodchem.2008.09.001

[37] Enaru B, Dretcanu G, Pop TD, Stănilă A, Diaconeasa Z. Anthocyanins: Factors affecting their stability and degradation. *Antioxidants.* 2021; 10: 1967.https://doi.org/10.3390/antiox10121967

[38] Golshan M, Osfouri S, Azin R, Jalali T, Moheimani NR. Co-sensitization of natural and low-cost dyes for efficient panchromatic light-harvesting using dye-sensitized solar cells. *J Photochem Photobiol A.* 2021; 417: 113345. https://doi.org/10.1016/j.jphotochem.2021.113345

[39] Kamarulzaman NH, Salleh H, Dagang AN, Ghazali MSM, Ishak N, Abdullah M, Muda SM. Eco-Friendly Hybrid Solar Cells using *Eugenia Claviflora* as New Alternatives Sensitizer to $TiO_2$/PEDOT:PSS. *IOPConf Ser Mater Sci Eng*. 2021; 1176: 012047. https://doi.org/10.1088/1757-899X/1176/1/012047

[40] Erande KB, Hawaldar PY, Suryawanshi SR, Babar BM, Mohite AA, Shelke HD, Nipane SV, Pawa UT. Extraction of natural dye (specifically anthocyanin) from pomegranate fruit source and their subsequent use in DSSC. *Mater Today Proc.* 2021; 43(4): 2716-2720. https://doi.org/10.1016/j.matpr.2020.06.357

[41] PrabavathyN, Balasundaraprabhu R, Arne S, Kristoffersen G,BalajiS,PrasannaK, SivakumaranMD, KannanSvein R, Dhayalan Velauthapillai E. Enhanced photostability of anthocyanin dye for increased efficiency in natural dye sensitized solar cells. *Optik*. 2021; 227: 166053. https://doi.org/10.1016/j.ijleo.2020.166053

[42] Gasga K. Dye and activated carbon from *Canarium ovatumEngl*. as photosensitizer and counter electrode for Titania-based dye sensitized solar cell. *J Phys Conf Ser.* 2021; 1882: 012007. https://doi.org/10.1088/1742-6596/1882/1/012007

[43] Huamán AA, Celestino MR, Quintana ME. Theoretical and experimental study of solar cells based on nanostructured films of $TiO_2$ sensitized with natural dyes extracted from *Zea mays* and *Bixa orellana*. *RSC Adv.* 2021; 11: 9086-9097. https://doi.org/10.1039/d1ra01043c

[44] Faraz SM, Mazhar M, Shah W, Noor H, Awan ZH, Sayyad MH. Comparative study of impedance spectroscopy and photovoltaic properties of metallic and natural dye based dye sensitized solar cells. *Phys B.* 2021; 602: 412567. https://doi.org/10.1016/j.physb.2020.412567

[45] Joseph S, Paul Winston AJP, Muthupandi S, Shobha P, Margaret SM, Sagayaraj P. Performance of Natural Dye Extracted from Annatto, Black Plum, Turmeric, Red Spinach, and Cactus as Photosensitizers in $TiO_2$NP/TiNT Composites for Solar Cell Applications. *J Nanomater.* 2021; 2021: 5540219. https://doi.org/10.1155/2021/5540219

[46] Singh S, Maurya IC, Sharma S, Kushwaha SPS, Srivastava P, Bahadur L. Application of new natural dyes extracted from Nasturtium flowers (*Tropaeolum majus*) as photosensitizer in dye-sensitized solar cells. *Optik*. 2021; 243: 167331. https://doi.org/10.1016/j.ijleo.2021.167331

[47] Fernandes AS, Nascimento TCD, Jacob-Lopes E, Rosso VVD, Zepka LQ. A brief overview on its structure, biosynthesis, synthesis, and applications. In: Zepka LQ, E. Jacob-Lopes E, Rosso VVD, eds. *Progress in Carotenoid Research*. InTech; 2018: 1-16. https://doi.org/10.5772/intechopen.79542

[48] Mezzomo N, Ferreira SRS. Carotenoids functionality, sources, and processing by supercritical technology. *J Chem*. 2016; 2016: 3164312. http://dx.doi.org/10.1155/2016/3164312

[49] Maoka T. Carotenoids as natural functional pigments. *J Nat Med.* 2019; 74(1): 1-16. https://doi.org/10.1007/s11418-019-01364-x

[50] Ashenafi EL, Nyman MC, Jacob T. Shelley JT, Mattson NS. Spectral properties and stability of selected carotenoid and chlorophyll compounds in different solvent systems. *Food Chem Adv.* 2023; 2: 100178. https://doi.org/10.1016/j.focha.2022.100178

[51] Namitha KK, Negi PS. Chemistry and Biotechnology of Carotenoids. *Crit Rev Food Sci Nutr.* 2010; 50: 728-760. https://doi.org/10.1080/10408398.2010.499811

[52] Takaichi S. Carotenoids in Algae: Distributions, Biosyntheses and Functions. *Mar Drugs.* 2011; 9: 1101-1118. https://doi.org/10.3390/md9061101

[53] Varghese R, Buragohain T, Banerjee I, Mukherjee R, Penshanwar SN, Agasti S, Ramamoorthy S. The apocarotenoid production in microbial biofactories. *J Biotech.* 2023; 374: 5-16. https://doi.org/10.1016/j.jbiotec.2023.07.009

[54] Hou X, Rivers J, León P, McQuinn RP, Pogson BJ. Synthesis and Function of Apocarotenoid Signals in Plants. *Trends Plant Sci.* 2016; 21(9): 792-803. https://doi.org/10.1016/j.tplants.2016.06.001

[55] Carballo-Uicab VM, C´ardenas-Conejo Y, Vallejo-Cardona AA, Aguilar-Espinosa M, Rodríguez-Campos J, Serrano-Posada H, Narv´aez-Zapata JA, V´azquez-Flota F, Rivera-Madrid R. Isolation and functional characterization of two dioxygenases putatively involved in bixin biosynthesis in annatto (Bixa orellana L.). *PeerJ.* 2019; 7: e7064. https://doi.org/10.7717/peerj.7064

[56] Alwis DDDH, Chandrika UG, Jayaweera PM. Photostability of apocarotenoids on surface of $TiO_2$ semiconductor nanoparticles. *J Photochem Photobiol A Chem*. 2021; 407: 113061. https://doi.org/10.1016/j.jphotochem.2020.113061

[57] Shakunthala NM. Natural Dyes as a Photosensitizer in Dye Sensitized Solar Cells- Review. *J Sci Res.* 2021; 65(8): 59-63. https://doi.org/10.37398/JSR.2021.650813

[58] Datte JK, Yapi SA, Kouassi LK, Douhoré GYT. Effect of $TiO_2$ Photoanode Films on the Performance of Dye Sensitized Solar Cell with Rauvolfia Vomitoria Fruit Extract. *Am J Mater Sci Eng.* 2021; 9(1): 1-5. https://pubs.sciepub.com/ajmse/9/1/1/index.html

[59] Coy-Barrera, E. Analysis of betalains (betacyanins and betaxanthins). In: Sanches Silva A, Nabavi SF, Saeedi M, Nabavi SM, ed. *Recent Advances in Natural Products Analysis.*Elsevier; 2020: 593-619. https://doi.org/10.1016/B978-0-12-816455-6.00017-2

[60] Sadowska-Bartosz I, Bartosz G. Biological properties and applications of betalains. *Molecules*. 2021; 26: 2520. https://doi.org/10.3390/molecules26092520

[61] Slimen IB, Najar T, Abderrabba M. Chemical and antioxidant properties of betalains. *J Agric Food Chem.* 2017; 65: 675-689. https://doi.org/10.1021/acs.jafc.6b04208

[62] Azeredo HMC. Betalains: Properties, sources, applications, and stability. *Int J Food Sci Technol.* 2009;44:2365-2376. https://doi.org/10.1111/j.1365-2621.2007.01668.x

[63] Lopera A, V´elez E, Restrepo J, Polo V. A DFT study on natural sensitizers with donor-π-acceptor architecture based on 1,7-diazaheptametine for applications in Dye-Sensitized Solar Cells (DSSC). *Comput Theor Chem.* 2024; 1232: 114450. https://doi.org/10.1016/j.comptc.2023.114450

[64] Bharathi Devi S, Prakash Babu D, Naresh Kumar S. Effect of microwave annealing on the performance of dye sensitized solar cell with Beta vulgaris as natural dye. *Spectrosc Lett*. 2021; 54(5): 352-359. https://doi.org/10.1080/00387010.2021.1931793

[65] Soni K, Sheikh A, Jain V, Lakshmi N. Application of Natural Betalain Dye from Beetroot for Improved Efficiency in Dye Sensitized Solar Cell. *IOP Conf Ser Mater Sci Eng*. 2021; 1187: 012005. https://doi.org/10.1088/1757-899X/1187/1/012005

[66] Li Y, He N, Hou J, Xu L, Liu C, Zhang J, Wang Q, Zhang X, Wu X. Factors influencing leaf chlorophyll content in natural forests at the biome scale. *Front Ecol Evol.* 2018; 6: 64. https://doi.org/10.3389/fevo.2018.00064

[67] Solymosi K, Mysliwa-Kurdziel B. Chlorophylls and their Derivatives Used in Food Industry and Medicine. *Mini Rev Med Chem.* 2017; 17(13): 1194-1222. https://doi.org/10.2174/1389557516666161004161411

[68] Martins T, Novo Barros A, Rosa E, Antunes L. Enhancing Health Benefits through Chlorophylls and Chlorophyll-Rich Agro-Food: A Comprehensive Review. *Molecules.*2023; 28(14): 5344. https://doi.org/10.3390/molecules28145344

[69] Pelletier PJ, Caventou JB, Sur la matière verte des feuilles. *Ann Chim Phys.* 1818; 9: 194-196.

[70] Richard Willstätter - Facts. NobelPrize.org. Nobel Prize Outreach 2025. https://www.nobelprize.org/prizes/chemistry/1915/willstatter/facts/. Accessed February 22, 2025.

[71] Hans Fischer - Facts. NobelPrize.org. Nobel Prize Outreach 2025. https://www.nobelprize.org/prizes/chemistry/1930/fischer/facts/. Accessed February 22, 2025.

[72] Robert B. Woodward - Biographical. NobelPrize.org. Nobel Prize Outreach 2025. https://www.nobelprize.org/prizes/chemistry/1965/woodward/biographical/. Accessed February 22, 2025.

[73] Tanaka R, Tanaka A. Chlorophyll cycle regulates the construction and destruction of thelight-harvesting complexes. *Biochim Biophys Acta.* 2011; 1807: 968-976. https://doi.org/10.1016/j.bbabio.2011.01.002

[74] Herrera M, Viera I, Roca M. Study of the authentic composition of the novel green foods: Food colorants and coloring foods. *Food Res Int.* 2023; 170: 112974. https://doi.org/10.1016/j.foodres.2023.112974

[75] Mejica GFCM, Ramaraj R , Unpaprom Y. Natural dye (chlorophyll, anthocyanin, carotenoid, flavonoid) photosensitizer for dye-sensitized solar cell: A review. *Maejo Int J Energ Environ Comm.* 2022; 4-1: 12-22. https://doi.org/10.54279/mijeec.v4i1.247970

[76] Cari C, Kurniawan D, Supriyanto A. The Effect of ZnO and $TiO_2$with Natural Dye of Broccoli (*Brassia oleracea var. italica*) on Dye-Sensitized Solar Cell (DSSC). *J Phys Conf Ser.* 2021;1842: 012055. https://doi.org/10.1088/1742-6596/1842/1/012055

[77] Kurniawan D, Cari C, Supriyanto A. Comparison of Nanocomposite ZnO/$TiO_2$ Composition Dye-Sensitized Solar Cell (DSSC) with Natural Dye Leaves of Green Mustard (*Brassica rapa*). *J Phys Conf Ser.* 2021;1842: 012056. https://doi.org/10.1088/1742-6596/1842/1/012056

[78] Arjun Kumar B, Ramalingam G, Karthigaimuthu D, Elangovan T, Vetrivelan V. Fabrication of natural dye sensitized solar cell using tridax procumbens leaf and beetroot extract mixer as a sensitizer. *Mater Today Proc.* 2021;49(7):2541-2545. https://doi.org/10.1016/j.matpr.2021.04.221

[79] Mensah-Darkwa K, Agyemang FO, Yeboah D, Akromah S. Dye-sensitized solar cells based on graphene oxide and natural plant dye extract. *Mater Today Proc.* 2021;38(2):514-521. https://doi.org/10.1016/j.matpr.2020.02.391

[80] Siregar N , Motlan, Panggabean JH, Sirait M, Rajagukguk J , Gultom NS , Kedir Sabir FK. Fabrication of Dye-Sensitized Solar Cells (DSSC) Using Mg-Doped ZnO as Photoanode and Extract of Rose Myrtle (Rhodomyrtus tomentosa) as Natural Dye.*Int J Photoenergy*. 2021; 2021. https://doi.org/10.1155/2021/4033692

[81] Anoua R, Lifi H, Touhtouh S, El Jouad M, Hajjaji A, Bakasse M, Plociennik P, Zawadzka A.Optical and morphological properties of *Curcuma longa* dye for dye-sensitized solar cells. *Environ Sci Pollut Res.* 2021;28:57860-57871. https://doi.org/10.1007/s11356-021-14551-9

# Potencijal odabranih biljnih pigmenata za korišćenje u solarnim ćelijama aktiviranim bojom: trenutni status

**Anita M. Lazić[1], Luka R. Matović[1], Nemanja P. Trišović[2] i Nataša V. Valentić[2]**

[1]*Inovacioni centar Tehnološko-metalurškog fakulteta, Beograd, Srbija*
[2]*Univerzitet u Beogradu, Tehnološko-metalurški fakultet, Beograd, Srbija*

(Osvežimo naše znanje)

*Izvod*

Treća generacija solarnih ćelija, u koje spadaju i solarne ćelije aktivirane bojom, privukla je veliku pažnju istraživača tokom poslednjih decenija, prevashodno zbog svoje netoksičnosti i ekonomičnosti. U ovom radu sumirano je dosadašnje istraživanje biljnih pigmenata sa mogućnošću primene kao fotosenzitizatora u solarnim ćelijama, pri čemu je fokus stavljen na njihovo izolovanje, prečišćavanje i faktore koji utiču na njihova fizičko-hemijska svojstva. Istraživanja o solarnim ćelijama uglavnom su usmerena ka flavonoidima, antocijaninima, karotenoidima, betalanima i hlorofilu, kao ekološki najprihvatljivijim prirodnim fotosenzitivnim jedinjenjima. Pored toga, podaci o solarnoj efikasnosti, do kojih se došlo primenom različitih tipova poluprovodnika i elektrolita, takođe su prikazani u ovom radu. Osnovni cilj ovog rada je da se istaknu mogućnosti upotrebe prirodnih fotosenzitivnih pigmenata u izradi solarnih ćelija i da se stavi akcenat na one kandidate čijom će se primenom u solarnim ćelijama postići najbolje performanse.

*Ključne reči:* Fotonaponske ćelije; flavonoidi; antocijanini; karotenoidi; betalaini; hlorofil

# Erratum

## Printed version only / Samo u štampanoj verziji

*Hem. Ind.* **79(1)** 67 (2025)

In the article
**Modelling of sanitary wastewater composition and operation of a small membrane bioreactor wastewater treatment plant with denitrification and nitrification**, by *David S. Mitrinović, Marija S. Perović, Srđan R. Kovačević, Miodrag R. Popović and Zorana Z. Radibratović*, published in Hem. Ind. **78(4)** 337-349 (2024), in the footnote on page 337 instead of
Paper received: 25 April 2024; Paper accepted: 17 December 2024; Paper published: 15 January 2024,
it should read:
Paper received: 25 April 2024; Paper accepted: 17 December 2024; Paper published: 15 January 2025

U radu
**Modelling of sanitary wastewater composition and operation of a small membrane bioreactor wastewater treatment plant with denitrification and nitrification**, autora *David S. Mitrinović, Marija S. Perović, Srđan R. Kovačević, Miodrag R. Popović and Zorana Z. Radibratović*, objavljenom u broju Hem. Ind. **78(4)** 337-349 (2024), u fusnoti na stranici 337 umesto
Paper received: 25 April 2024; Paper accepted: 17 December 2024; Paper published: 15 January 2024,
treba da piše:
Paper received: 25 April 2024; Paper accepted: 17 December 2024; Paper published: 15 January 2025
.